DEVELOPMENT AND APPLICATION OF FAST SIMULATION BASED ON THE PSS PRESSURE AS A SPATIAL COORDINATE

A Dissertation

by

KENTA NAKAJIMA

Submitted to the Office of Graduate and Professional Studies of
Texas A&M University
in partial fulfillment of the requirements for the degree of

DOCTOR OF PHILOSOPHY

Chair of Committee,	Michael J. King
Committee Members,	Eduardo Gildin
	Siddharth Misra
	Debjyoti Banerjee
Head of Department,	Jeff Spath

May 2021

Major Subject: Petroleum Engineering

ABSTRACT

Rapid modeling of multi-well interactions is extremely useful for infill drilling optimization and in the determination of optimal well spacing in reservoir development. In the case of unconventional reservoirs, especially, the requirement is especially acute for the low permeabilities, since the period of transient flow is large and the amount of historical data showing well interactions is limited.

This research starts by examining and extending previous applications of the Fast Marching Method (FMM) and the diffusive time of flight (DTOF). The previous study applied the 1D DTOF coordinate to numerical simulation (FMM-SIM), but the current approach enables pressure approximation without the need to solve numerical finite difference matrix system (FMM-DTOF), and this can be extendable to multi-well interaction through superposition. Although FMM has the strength in its fast computational time due to the dimensional reduction, it is based on the underlying assumption that the pressure drop should be well-aligned with the DTOF coordinate. As an alternative 1D coordinate, we propose the fast simulation based on the PSS as a spatial coordinate, which can overcome the limitations which FMM has and still hold the same benefit. First, we derive the 1D coordinate based on the PSS pressure under a 3D reservoir model and construct its discrete form. Next, we develop both a numerical system (PSS-SIM) and semi-analytic pressure solution (PSS-DTOF) under the PSS coordinate to analyse benefits of each approach. While a numerical simulation has its

own strength in its accuracy, semi-analytic approximation has its benefit in that it does not require solving computationally heavy non-linear matrix problems.

We validate the approaches against both an analytical solution and a commercial reservoir simulator. First, PSS-SIM provides excellent approximations to the flow simulation results under both early-mid and late time transient, which is an indicator of a well-aligned 1D coordinate along actual pressure drop of the entire reservoir. Secondly, PSS-DTOF also shows accurate performance in forecasting early-mid time transient of reservoirs, although it has a little mismatch in late time solution due to its pressure/flux approximation. Based on their strength and shortcoming, we concluded that PSS-DTOF is more suitable for early-mid time reservoir development, such as well spacing optimization problems, while PSS-SIM is a useful tool for late time transient analysis.

DEDICATION

To my families

ACKNOWLEDGEMENTS

I would like to thank my advisor, Dr. Michael J. King for his guidance and support throughout the course of this research. Data analytics approach against new technical problems, learned from him through day-by-day communication, is a treasure for my R&D life.

I would like to appreciate my friends and colleagues in my classes, my research group and Student Chapter of Society of Petroleum Engineers at Texas A&M University. All of them made my school life at Texas A&M University a great experience. Thanks also go to Phaedra L. Hopcus for her support in setting up opportunities for us to present our research and development to industry.

Besides, I am grateful for Schlumberger and Sciencesoft to provide data analytics software to Texas A&M University, which helped my research study.

Finally, thanks to my mother, father and sister for their encouragement.

CONTRIBUTORS AND FUNDING SOURCES

Contributors

This work was supervised by a dissertation committee consisting of Professor Michael J. King, Eduardo Gildin and Siddharth Misra in the Department of Petroleum Engineering, and Professor Debjyoti Banerjee in the Department of Mechanical Engineering. All work conducted for the dissertation was helped by Professor Michael J King through continuous discussions and completed by the student independently.

Funding Sources

Graduate study was supported by Model Calibration and Efficient Reservoir Imaging (MCERI), Texas A&M University. Besides, this research project is completed thanks to the financial support by Dr. Datta-Gupta through a joint research project with Saudi Aramco. Finally, this work was also made possible in part by Dr. Morita.

NOMENCLATURE

B_o	Oil formation volume factor, RB/STB
B_w	Water formation volume factor, RB/STB
c_t	Total compressibility, psi^{-1}
c_o	Oil compressibility, psi^{-1}
c_f	Rock compressibility, psi^{-1}
ΔX	Cell length in the X direction, ft
ΔY	Cell length in the Y direction, ft
ΔZ	Cell length in the Z direction, ft
F_i	Flag function for well control state "*i*"
k	Permeability, mD
ORAT	Oil production rate, STB/D
p	Pressure, psia
p_{init}	Initial reservoir pressure, psia
q	Total flux, RB/D
q_D	Dimensionless total flux at reservoir conditions
q_o	Oil production rate, STB/D
q_t	Total well flow rate, RB/D
q_w	Water production rate, STB/D

r_0 Peaceman radius, ft

r_w Wellbore radius, ft

$S_{w,init}$ Initial water saturation, dimensionless

t Time, day

$w_r(\tau)$ Derivative of cumulative reservoir resistivity with respect to τ, (cp*ft^3)/(psi*hr$^{0.5}$)

J Productivity index, RB/D/psi

V_p Pore volume at reservoir conditions, ft^3

Q Cumulative total fluid production, RB

$V_d(t)$ Drainage volume at reservoir conditions, ft^3

$V_p(\tau)$ Cumulative pore volume at reservoir conditions, ft^3

V_{DP} Dykstra-Parsons coefficient, dimensionless

α Diffusivity, ft^2/day

δp Pressure drop from initial pressure, psi

Δp Pressure difference from bottomhole pressure, psi

$\bar{p}$ Average reservoir pressure, psia

ϕ Porosity, dimensionless

μ Viscosity, cp

τ Diffusive time of flight, hour$^{0.5}$

θ Normalized PSS pressure drop, psi/cp/RB

λ_{rt} Total mobility, cp^{-1}

$\overline{\sigma^2}$ Mean variance, dimensionless

TABLE OF CONTENTS

Page

LIST OF FIGURES

Page

LIST OF TABLES

Page

1. INTRODUCTION AND LITERATURE REVIEW

1.1. Introduction

For optimization of well performance to obtain maximum oil production, it is essential to have a good understanding of pressure propagation in a reservoir. Although all reservoir engineering measures are rooted in the same diffusivity equation, there are two common tools to help engineers to better characterize reservoir properties: analytical solutions and numerical solutions. While the use of analytical solutions, such as pressure transient analysis (PTA) and rate transient analysis (RTA), are limited to simple and homogeneous reservoirs with a single well, they can provide quick insight about pressure propagation around wells (Horne, 1995; Lee, 1982; Lee, Rollins, & Spivey, 2003; Thambynayagam, 2011). Meanwhile, numerical simulation is useful in reservoir characterization by integrating detailed 3D geologic models with flow simulation, but is not always suitable for giving a simple insight to grasp reservoir performance near wells. In most unconventional reservoirs, reservoir engineers are often required to make quick decisions over their development plans with limited subsurface data availability, so they cannot rely on the computationally heavy numerical simulation for each decision. Thus, developing a rapid semi-analytic approach, which treats a reservoir as a simplified 1-D representation based on DTOF, but can still consider its heterogeneity, is helpful when making decisions in reservoir development.

The fundamental concept of the semi-analytic approach is originated from the diffusivity equation. Transforming the analytic solution of the diffusivity equation, Lee first defined a ‘radius of investigation’ from a speed of propagation of a peak pressure disturbance from an impulse sink/source (Lee, 1982). This radius is related to the physical distance where the

maximum of impulse response arrive from the sink/source. This concept has been generalized by introducing a Diffusive Time of Flight (DTOF), which represents a travel time of the pressure disturbance from a sink/source (Datta-Gupta, Xie, Gupta, King, & Lee, 2011). Utilizing the DTOF of each cell from a well, we can perform a coordinate transformation from a 3-D spatial grid to a 1-D DTOF grid, which integrates the effects of reservoir heterogeneity on well performance (Fujita, Datta-Gupta, & King, 2015, 2016; Zhang et al., 2014, 2016; Zhang, Yang, King, & Datta-Gupta, 2013). This asymptotic approximation provides us with an underlying drainage pore volume geometry of a well and an important interpretation of the well test derivative in terms of the inferred transient drainage volume (King, Wang, & Datta-Gupta, 2016; Wang, Li, & King, 2017).

In the case of unconventional reservoirs, multiple transverse fracture wells (MTFW's) have been widely employed to access the stimulated reservoir volume (SRV). The asymptotic approach has been further developed to construct novel analytic solutions for infinite reservoirs with MTFW's by means of superposition (Malone, King, & Wang, 2019). The solutions developed have shown that they can consider fracture-to-fracture interference effects and forecast individual fracture behavior accurately under fixed rate, fixed bottomhole flowing pressure (BHP) and variable rate boundary conditions. Besides, it is noteworthy that drainage volume progression of a well can be calculated as a collective behavior of multiple single fracture drainage volumes.

The 1D pressure solution based on the coordinate transformation can be categorized into four methods: FMM-SIM, FMM-DTOF, PSS-SIM and PSS-DTOF. Table 1 summarizes the main concepts of these four approaches. With respect to the coordinate, while both FMM-SIM and FMM-DTOF are based on the same DTOF coordinate, PSS-SIM and PSS-DTOF are

constructed based on the normalized PSS pressure drop at the late time. In terms of the discretization, FMM-SIM/DTOF is based on cumulative pore volume, while PSS-SIM/DTOF performs 3D grid coarsening. Regarding the 1D transmissibility, FMM-SIM/DTOF calculates it using piecewise linear interpolation, although PSS-SIM/DTOF obtains its value by PSS upscaling. Lastly, as for the pressure solution, FMM-SIM and PSS-SIM solve the numerical finite difference system by numerical simulation, while FMM-DTOF and PSS-DTOF calculate the pressure solution using asymptotic approximation.

Table 1 Four Different 1D Pressure Solutions

Method	FMM-SIM	FMM-DTOF	PSS-SIM	PSS-DTOF
Coordinate	DTOF	DTOF	PSS Pressure Drop	PSS Pressure Drop
1D Discretization	Cumulative Pore Volume	Cumulative Pore Volume	Coarsened 3D Grid	Coarsened 3D Grid
1D Transmissibility	Piecewise Linear Interpolation	Piecewise Linear Interpolation	PSS Upscaling	PSS Upscaling
Pressure Solution	Numerical Simulation	Asymptotic Pressure Approximation	Numerical Simulation	Asymptotic Pressure Approximation

In this research study, we first start with a literature review of the previous work on FMM-SIM/DTOF for its single well reservoir applications. In this study, the concept of FMM-DTOF is extended to multiple well reservoir developments by means of superposition. Other studies have appliedFMM-SIM to multiple well reservoir development by partitioning the reservoir into each region based on the DTOF (Iino & Datta-Gupta, 2018; Iino, Jung, Onishi, & Datta-Gupta, 2020; Iino, Onishi, & Datta-Gupta, 2020). However, we will explore an alternative approach based upon superposition. Next, we develop PSS-SIM in Chapter 3 in comparison with FMM-SIM/DTOF. Based on the 1D PSS coordinate, we develop a one dimensional Eikonal equation with an asymptotic pressure solution in order to apply the approach to multiple well

models. Finally, all four of these approaches are compared with one another to see what impact the newly developed coordinate provides.

1.2. Diffusivity Equation, Asymptotic Approximation and Eikonal Equation

The derivation of the asymptotic pressure solution is obtained from the well-known diffusivity equation (Dake, 1983; Lee, 1982; Lee et al., 2003) as shown in Eq. (1.1).

$$\phi(\vec{x})c_t(\vec{x},t)\frac{\partial p(\vec{x},t)}{\partial t}+\nabla\bullet\vec{u}(\vec{x},t)=0 \tag{1.1}$$

$$\vec{u}(\vec{x},t)=-\frac{\vec{\vec{k}}(\vec{x})}{\mu}\bullet\nabla p(\vec{x},t) \tag{1.2}$$

This is the form of Darcy's equation for single phase flow, and will be generalized later. By applying Fourier transformation shown as Eq. (1.3) to Eq. (1.1), we can derive the diffusivity equation in the frequency domain shown as Eq. (1.4).

$$\tilde{p}(\vec{x},\omega)=\int_{-\infty}^{\infty}p(\vec{x},t)e^{-i\omega t}dt=e^{-\sqrt{-i\omega}\tau(\vec{x})}\sum_{j=0}^{\infty}\frac{A_j(\vec{x})}{\left(\sqrt{-i\omega}\right)^j} \tag{1.3}$$

$$\phi(\vec{x})\mu c_t(-i\omega)\tilde{p}(\vec{x},\omega)-\nabla\bullet\left(\vec{\vec{k}}(\vec{x})\bullet\nabla\tilde{p}(\vec{x},\omega)\right)=0 \tag{1.4}$$

The parameter τ shown in Eq. (1.3) is called the diffusive time of flight (DTOF), which corresponds to the physical distance in terms of the pressure disturbance propagation from a sink/source. (Datta-Gupta et al., 2011) showed that there is a correlation between pressure drop and DTOF $\left(p(\vec{x},t)\approx p\left(\tau(\vec{x}),t\right)\right)$ for smoothly varying heterogeneous media. The high frequency limit of Eq. (1.4) leads to Eq. (1.5).

$$\nabla\tau(\vec{x})\bullet\vec{\vec{\alpha}}(\vec{x})\bullet\nabla\tau(\vec{x})=1 \tag{1.5}$$

$$\vec{\vec{\alpha}}(\vec{x})=\frac{\vec{\vec{k}}(\vec{x})}{\phi(\vec{x})\mu c_t} \tag{1.6}$$

Eq. (1.5) is called Eikonal equation and Eq. (1.6) is called diffusivity, $\alpha(\vec{x})$, the square root of which can be regarded as the propagation speed of pressure disturbance. Here, as a boundary condition, we assign $\tau = 0$ to all perforations, which corresponds to $r = 0$. This system then can be solved by the use of the Fast Marching Method (Sethian, 1999; Zhang et al., 2014, 2016; Zhang et al., 2013).

1.3. Fast Marching Calculation of the Diffusive Time of Flight

Eq. (1.5) indicates that the local travel time of a pressure front is inversely proportional to the square root of diffusivity $\alpha(\vec{x})$. This equation has a form of the Eikonal equation, and can be efficiently solved by the use of Fast Marching Method (FMM). This algorithm is a class of front tracking methods proposed by Sethian (1996). The principal algorithm is summarized below.

(1) Label all node points as '*unknown'*
(2) Initialize the Diffusive Time of Flight (DTOF) at the starting points to zero and label those nodes as '*considered'*
(3) Select the node which has the minimum DTOF among the '*considered'* nodes and update its label to be '*accepted'*
    a. Update the labels of any adjacent '*unknown'* nodes to '*considered'*
    b. Update the values in any adjacent nodes that are labeled '*considered'*
(4) Go to step (3) until all nodes become '*accepted'*

As a simple exampleconsider the 2D 5-point stencil Cartesian grid model. In this case, the process explained above is illustrated below (Datta-Gupta et al., 2011). First, the starting point of the pressure propagation is labeled as 'accepted' and its DTOF is initialized to zero as described in (a). Next, its neighbors A, B, C, and D are labeled as 'considered', and their DTOF's are updated from their neighboring 'accepted' point based on the solution of Eikonal equation, which is described in (b). After all the DTOF's at A, B, C and D have been updated, the smallest DTOF among them, which is supposed to be A in the figure below, is selected. Its label is

changed into ‘accepted’ as described in (c). In step (d), its neighbors, E, F and G are newly added to ‘considered’ lists. The series of the updating process ((b) and (c)) is to be continued until the next ‘accepted’ point, which is supposed to be D in the figure (e) and (f), is obtained. Finally, the overall flow described here is to be repeated until all the nodes are labeled as ‘accepted’.

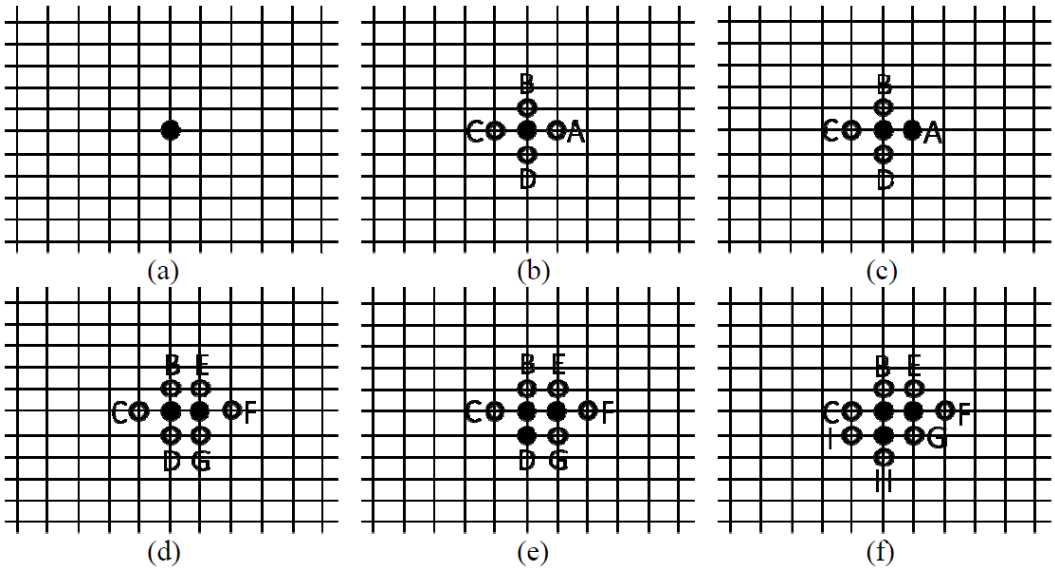

Figure 1 Fast Marching Method, Reprinted from (Datta-Gupta et al., 2011)

The local solution of the Eikonal equation can be calculated from the standard finite difference equation shown below (Sethian 1996).

$$\max\left(D_{ij}^{-x}\tau, D_{ij}^{+x}\tau, 0\right)^2 + \max\left(D_{ij}^{-y}\tau, D_{ij}^{+y}\tau, 0\right)^2 = \frac{1}{\alpha} \tag{1.7}$$

Here, D represents a gradient of finite difference scheme approximated with first order truncation error. For simplicity, we assume the 5-point stencil FMM for 2D Cartesian grid model. In this case, $D_{ij}^{-x}\tau = \left(\tau_{i,j} - \tau_{i-1,j}\right)/\Delta x$ and $D_{ij}^{+x}\tau = \left(\tau_{i+1,j} - \tau_{i,j}\right)/\Delta x$. Similar equations hold in the y-direction. Solving Eq (1.7) gives us DTOF at all nodes, which can be used as a new coordinate for the following pressure solutions.

In the process of solving the Eikonal equation, it is necessary to consider which discretization scheme to use. For simplicity, we describe 2D examples in this section as shown in Figure 2.

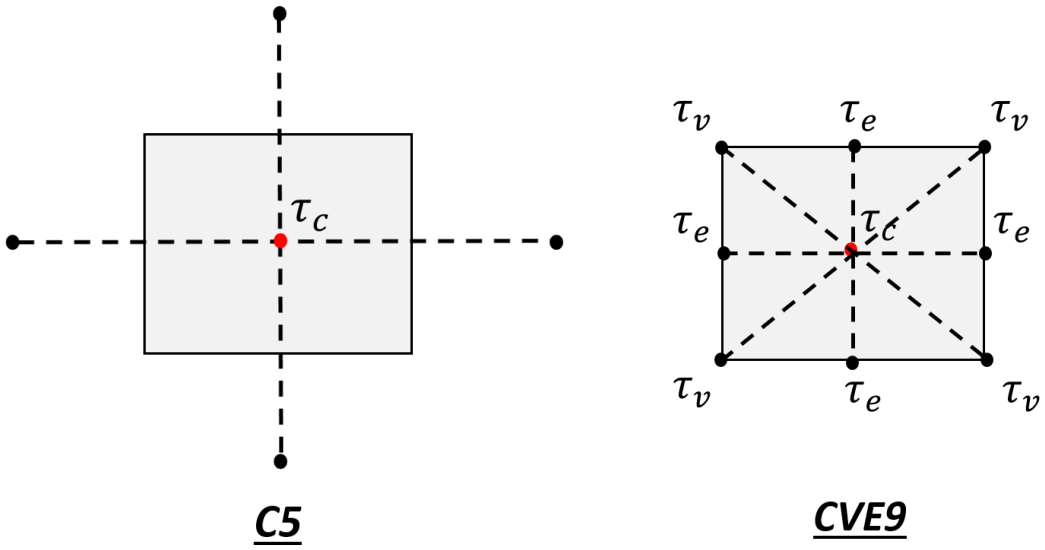

Figure 2 DTOF Calculation Schemes

The simplest way to calculate the DTOF is C5. In this case, we set the node points at the center of each cell, and calculate the DTOF based on the four adjacent nodes (up, down, right and left). For increased accuracy, we can utilize nodes at the vertices and edges of each cell in addition to the center (Li & King, 2020). This also will enhance the accuracy of the discrete volumetric calculations, as there will now be 8 octant elements per cell. Since CVE9 has been proven to be more accurate than C5, the DTOF coordinate is calculated based on this scheme in this research study. In the case of 3D models, there are 1 center node, 8 vertices shared with 8 cells, 12 edges shared with 4 cells and 6 faces shared with 2 cells (CVFE27 stencil). This concept can be extended for an unstructured grid under a complex fracture system, which

provides better characterization of transient drainage volume for complex fracture systems without losing the ability for rapid simulation of the reservoir performance (Yang, Xue, King, & Datta-Gupta, 2017). In a recent study, the solution is further generalized using a control volume finite difference discretization so that it is free of grid geometries and simply depends on cell volumes and intercell transmissibilities (Chen, Onishi, Park, & Datta-Gupta, 2020).

1.4. 1D DTOF-Based Flow Equations

First, a 1D form of the diffusivity equation can be obtained in the DTOF coordinate, where the diffusivity equation expressed as Eq. (1.1) can be written as Eq. (1.8). Here, the pressure derivative of time in the 1D DTOF coordinate is defined as the pore volume weighted average of the pressure derivative based on the original 3D coordinate.

$$0=\lim_{\Delta\tau\to 0}\int_{\Delta\tau}\left\{\phi\left(\vec{x}\right)c_t\left(\vec{x},t\right)\frac{\partial p\left(\vec{x},t\right)}{\partial t}+\nabla\bullet\vec{u}\right\}d^3x \tag{1.8}$$

By integrating Eq. (1.8), we can obtain Eq. (1.9), which is the diffusivity equation under the 1D coordinate.

$$c_t\left(\tau,t\right)\frac{dV_p}{d\tau}\frac{\partial p\left(\tau,t\right)}{\partial t}-\frac{\partial q\left(\tau,t\right)}{\partial\tau}=0 \tag{1.9}$$

This equation provides the foundation for single phase FMM-SIM and FMM-DTOF. It can be extended to multiple phases for FMM-SIM (Iino & Datta-Gupta, 2018; Iino, Jung, et al., 2020; Iino, Onishi, et al., 2020; Iino et al., 2017; Park, Iino, Datta-Gupta, Bi, & Sankaran, 2019).

Following the treatment in these references for multiphase flow, the diffusivity, Eq. (1.6), is generalized to include fluid properties, providing an additional source of heterogeneity. The inverse of the single phase viscosity is replaced by the relative total mobility, $\lambda_{rt}\left(S\right)$, Eq. (1.10),

where $S=(S_w,S_o)$ for a water-oil system. The total compressibility also depends upon the saturation, Eq. (1.11)

$$\lambda_{rt}(S)=\frac{k_{rw}(S)}{\mu_w}+\frac{k_{ro}(S)}{\mu_o} \tag{1.10}$$

$$c_t=c_f+c_wS_w+c_oS_o \tag{1.11}$$

The phase viscosity, phase compressibility, and rock compressibility may also depend upon the pressure. When solving the Eikonal equation, the initial values of saturation and pressure are utilized.

The flow equations have been generalized from this earlier work to include the fluid heterogeneity. The spatial heterogeneity is taken into account in the form of the reservoir resistivity $R(\tau)$ (Li, Wang, & King, 2021).

$$q(\tau,t)=\lambda_{rt}(S)\vec{n}(\vec{x})\bullet\vec{\vec{k}}(\vec{x})\bullet\nabla p\approx\lambda_{rt}(S)\frac{dR(\tau)}{d\tau}\frac{\partial p}{\partial\tau}(\tau,t) \tag{1.12}$$

$$V_p(\tau)=\int_0^{\tau}\phi(\vec{x})d^3x,\quad w(\tau)=\frac{dV_p}{d\tau} \tag{1.13}$$

$$R(\tau)=\int_0^{\tau}\lambda_{rt}^{-1}(\vec{x},0)c_t(\vec{x},0)\phi(\vec{x})d^3x,\quad w_r(\tau)=\frac{dR}{d\tau} \tag{1.14}$$

The use of the reservoir resistivity to define the cross-sectional area for fluid flow, $\vec{n}(\vec{x})$, ensures that $q(\tau,t)$ has no terms depending upon 3D location $\vec{x}$, but only τ. The flux term $q(\tau,t)$ denotes total flux that crosses a given τ contour as shown in Figure 3. The flux may be determined by a finite difference calculation or can be derived using asymptotic approximation based on the upstream reservoir volume (refer to Section 1.5).

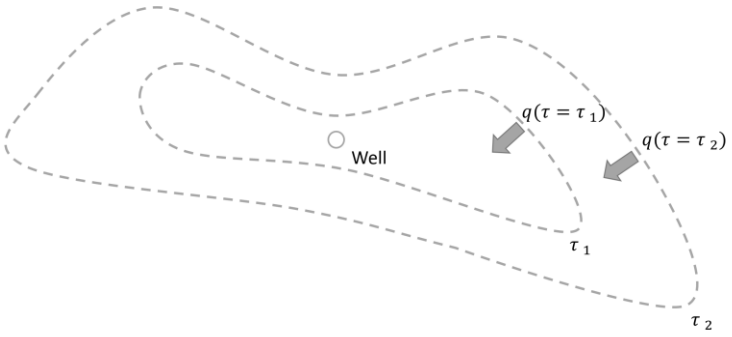

Figure 3. Concept of total flux along τ

At the wellbore surface $r = r_w$, we define τ_w for a single perforation of a vertical well.

$$\tau_w = \frac{1}{2} r_w \left(\frac{1}{\sqrt{\alpha_x}} + \frac{1}{\sqrt{\alpha_y}} \right) \tag{1.15}$$

This is consistent with the analysis of anisotropy in Peaceman's derivation of the Well Index (Donald W. Peaceman, 1983). In the case of multiple perforations, the requirement that $w_r(\tau_w)$ be equal to the sum over all perforations can be expressed as Eq. (1.16),.

$$\tau_w = \sum_{ijk}^{Radial} \left\{ (kh) \left(\frac{1}{2} r_w \right) \left(\frac{1}{\sqrt{\alpha_x}} + \frac{1}{\sqrt{\alpha_y}} \right) \right\}_{ijk} \Bigg/ \sum_{ijk}^{Radial} (kh)_{ijk} \tag{1.16}$$

The expression $R(\tau) = \pi \sqrt{k_x k_y} h \tau^2$ for radial flow in a perforated cell has been utilized.

Integrating Eq. (1.12) with respect to τ, we can get Eq. (1.17).

$$p(\tau, t) = p_{wf}(t) + \int_{\tau' = \tau_w}^{\tau} \frac{q(\tau', t)}{\lambda_{rt}\left(S(\tau', 0)\right) w_r(\tau')} d\tau' \tag{1.17}$$

In the FMM-DTOF calculations, we treat the saturation and viscosity as constants over time, fixed by the initial values of saturation and pressure. Saturations and pressures are each a function of location τ obtained by the pore volume weighted average in $\vec{x}$ over a τ interval. and viscosity is measured based on the initial pressure.

By taking the pore volume weighted average of the pressure profile, we can calculate average pressure within the range from τ_w up to τ.

$$\bar{p}(\tau,t) = p_{wf}(t) + \frac{q_t(t)}{\Delta V_p(\tau)} \int_{\tau'=\tau_w}^{\tau} \int_{\tau''=\tau_w}^{\tau'} \frac{q_D(\tau'',t)}{\lambda_{rt}\left(S(\tau'',0)\right) w_r(\tau'')} d\tau'' dV_p(\tau') \tag{1.18}$$

Here, $\Delta V_p(\tau) = V_p(\tau) - V_p(\tau_w)$ is the reservoir storage from τ_w. Evaluating Eq. (1.18) from a well (τ_w) up to a reservoir boundary $(\tau_{\max})$, we can get the average pressure over the entire reservoir, $\bar{p}(t)$. This average may be used to calculate the Productivity Index $J(t)$, as Eq. (1.19) (Wang, Malone, & King, 2019).

$$\bar{p}(t) = p_{wf}(t) + q_t(t) \cdot J^{-1}(t) \tag{1.19}$$

$$J^{-1}(t) = \frac{\bar{p}(t) - p_{wf}(t)}{q_t(t)} = \frac{1}{\Delta V_{p,\max}} \int_{\tau'=\tau_w}^{\tau_{\max}} \int_{\tau''=\tau_w}^{\tau'} \frac{q_D(\tau'',t)}{\lambda_{rt}\left(S(\tau'',0)\right) w_r(\tau'')} d\tau'' dV_p(\tau') \tag{1.20}$$

This expression for the productivity index is time dependent as it generalizes the usual definition of the productivity index to transient flow. Here, for convenience, since we may deal with multiphase flow, we have defined the productivity index with respect to total reservoir flux. The average reservoir pressure can also be obtained by integrating the diffusivity equation (Eq. (1.1)) with respect to τ and time to obtain the pore volume weighted average pressure.

$$\bar{p}(t) = p_{init} - \frac{Q(t)}{c_t \Delta V_{p,\max}} \tag{1.21}$$

Here, $Q(t)$ is the total produced fluid volume at reservoir conditions, which is obtained from the time integral of Eq. (1.1). Combining Eq. (1.19) and Eq. (1.21) gives us the equation for $p_{wf}(t)$.

$$p_{wf}(t) = p_{init} - \frac{Q(t)}{c_t \Delta V_{p,\max}} - q_t(t) \cdot J^{-1}(t) \tag{1.22}$$

To solve the system, we need a boundary condition. Under rate control, $q_t(t)$ is specified as a known target rate, allowing us to solve for $p_{wf}(t)$. If $p_{wf}(t)$ is given, for instance as a pressure constraint, then the solution of the equation gives us $q_t(t)$. In the following chapters, we solve the system using asymptotic pressure approximation (FMM-DTOF). FMM-DTOF can be differentiated from numerical FMM simulation (FMM-SIM) in that FMM-DTOF does not solve the finite difference fluid flow equations, but its governing equation is given by mass balance and the asymptotic pressure approximation (Zhang et al., 2014, 2016; Zhang et al., 2013).

1.5. Asymptotic Pressure Approximation

For the Infinite Acting Transient Flow (IATF) asymptotic pressure solution (King et al., 2016; Wang et al., 2017), we have an expression for $\frac{\partial p}{\partial t}$, as shown in Eq. (1.23).

$$c_t(\tau,t)\frac{\partial p}{\partial t} = \frac{\partial q}{\partial V_p(\tau)} \approx -\frac{q_t}{V_d(t)} e^{-\tau^2/4t}, \quad q = \lambda_{rt}(S)\frac{dR}{d\tau}\frac{\partial p}{\partial \tau} \tag{1.23}$$

$$q = q_t \quad at \quad \tau = \tau_w \tag{1.24}$$

$$V_d(t) = \int_{\tau=\tau_w}^{\infty} e^{-\tau^2/4t} dV_p(\tau) = \int_{\tau(\vec{x})\geq\tau_w}^{\infty} \phi(\vec{x}) e^{-\tau^2/4t} d^3x \tag{1.25}$$

The pressure drawdown in Eq. (1.23), can be expressed as a summation of terms, each with its own function of time (King et al., 2016; Wang et al., 2017). Winestock and Colpitts showed that this expression can be approximated using only the first term in the case of smooth rate variations (Winestock & Colpitts, 1965). Integration of Eq. (1.23) from a τ contour to the outer boundary of the reservoir gives the flux at a specific location and time $q(\tau,t)$. For a water-oil system, we can express the flux in terms of the total flux at reservoir conditions,

$$q_t = q_o B_o + q_w B_w \tag{1.26}$$

$$q(\tau,t)=q_t(t)\cdot q_D(\tau,t),\quad q_D(\tau,t)=\left(\frac{\int_{\tau(\vec{x})\geq\tau}^{\infty}\phi(\vec{x})e^{-\tau^2/4t}d^3x}{\int_{\tau(\vec{x})\geq\tau_w}^{\infty}\phi(\vec{x})e^{-\tau^2/4t}d^3x}\right) \tag{1.27}$$

$q_D(\tau,t)$ represents the dimensionless flux at the location of τ. In the PSS limit, the exponential term becomes one, so the reservoir storage term reduces to the upstream pore volume.

1.6. Discretization

1.6.1. 1D DTOF Discretization

In this section, we examine the discretization of Eq. (1.22) into $N+1$ intervals. The first interval $(i=0)$ ranges from τ_w to τ_0, and τ which is bigger than τ_0 is discretized into N intervals.

First, we start 1D DTOF discretization from a well cell. Figure 4 describes the discretization of a well block in the case of a single perforation well.

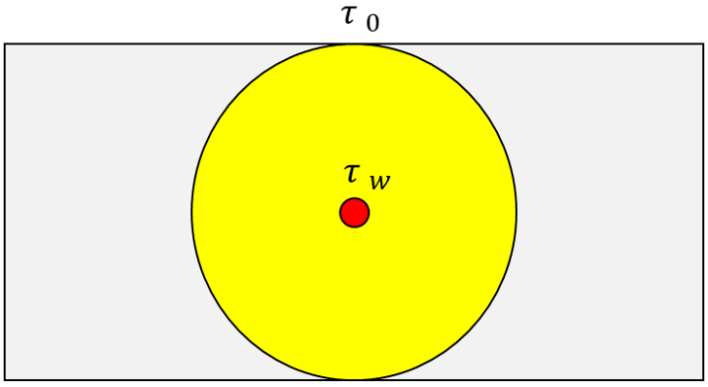

Figure 4 Definition of τ_w and τ_0 in Single Perforation

$$\tau_0=\min\left(\frac{\Delta X}{2\sqrt{\alpha_x}},\frac{\Delta Y}{2\sqrt{\alpha_y}}\right)\quad @VerticalWell \tag{1.28}$$

In the case of a multiple perforation well, we take the positive smallest value among all perforations. Next, we consider discretization of the 3D reservoir grid into 1D DTOF coordinate as shown in Figure 5.

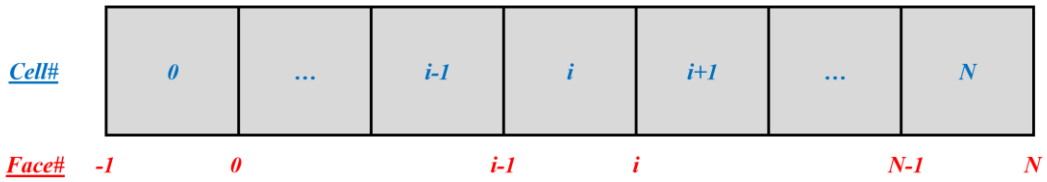

Figure 5 Cell and Face Indices, $\tau_{-1} = \tau_w$

In this figure, $\tau_{-1} = \tau_w$. In the case of a 3D CVFE27 FMM solution, there are $(2NX+1)\cdot(2NY+1)\cdot(2NZ+1)$ nodes in a model. Following (Li et al., 2021), we develop the 1D discretization beyond the well blocks based on these nodes and on the constraint of Eq. (1.29).

$$\tau_i = \min\left(\tau \geq \tau_{i-1} + \Delta\tau\right), \quad i = 1,\ldots,N \tag{1.29}$$

The purpose of this filtering is to obtain a sufficiently smooth $w_r(\tau)$, and corresponding calculation for the transmissibility. The interval size $\Delta\tau$ is usually selected as the first interval of the DTOF coordinate. The selected τ through the process is defined as reference τ. In the following sections, we utilize the reference τ for discretization of the drainage volume and the discrete flux calculation.

1.6.2. Drainage Volume and Reservoir Resistivity

In this section, we consider the discretization of $V_p(\tau)$ and $R(\tau)$, defined in Section 1.4. Since the calculations are sensitive to the flow geometry near the well, we use an analytical solution for radial flow inside each well block up to τ_0. Beyond that, and for the non-well cells,

linear interpolation is used to determine the portion of the volume of each cell up to τ, as shown in Figure 6. Combining the radial and the piecewise linear sections, $V_p(\tau)$ and $R(\tau)$ can be expressed as Eq. (1.30)-(1.31) in a discretized form.

$$V_p(\tau) = \pi \cdot \sum_{ijk}^{Radial} \left(\sqrt{\alpha_x \alpha_y} h\phi\right)_{ijk} \cdot Min\left(\tau^2, \tau_{0,ijk}^2\right) + \sum_{\ell}^{Linear} PV_\ell \cdot Min\left(1, Max\left(0, \frac{\tau - \tau_\ell^{\min}}{\tau_\ell^{\max} - \tau_\ell^{\min}}\right)\right) \tag{1.30}$$

$$\begin{aligned} R(\tau) = \pi \cdot & \sum_{ijk}^{Radial} \left(\sqrt{k_x k_y} h\right)_{ijk} \cdot Min\left(\tau^2, \tau_{0,ijk}^2\right) \\ & + \sum_{\ell}^{Linear} \lambda_{rt0}^{-1} c_{t0} \cdot PV_\ell \cdot Min\left(1, Max\left(0, \frac{\tau - \tau_\ell^{\min}}{\tau_\ell^{\max} - \tau_\ell^{\min}}\right)\right) \end{aligned} \tag{1.31}$$

In the above equation, mobility and total compressibility are evaluated at the initial condition. α and h are diffusivity and length of a well in each cell, respectively. The combination $\lambda_{rt0}^{-1} c_{t0} \sqrt{\alpha_x \alpha_y} h\phi$ in the expression for the resistivity in the well cells evaluates to the familiar form $\sqrt{k_x k_y} h$, as shown. $\tau_\ell^{\max}$ and $\tau_\ell^{\min}$ are maximum and minimum τ in each linear element or cell l. PV_ℓ denotes the pore volume of a linear element l, defined by each of the sub-volumes in the CVFE27 FMM solution, or for each cell l.

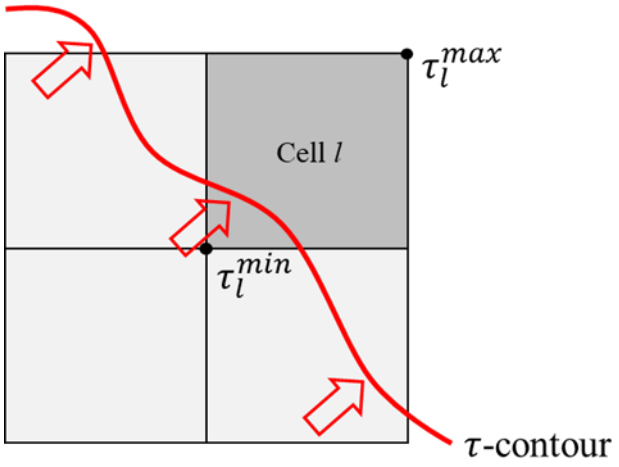

Figure 6. Description of $\tau_\ell^{\max}$ and $\tau_\ell^{\min}$ for a Cell Volume

Next, consider the discretization of $w_r(\tau)$. As for the near well region where $\tau \le \tau_0$, the flow geometry is radial, so $w_r(\tau)$ can be expressed as Eq. (1.32), which is obtained from the summation of the derivative of $R(\tau)$ with respect to τ for each perforation.

$$w_r(\tau) = \frac{dR}{d\tau} = \tau \cdot \sum_{ijk}^{Perforations} \left(2\pi\sqrt{k_x k_y}h\right)_{ijk}, \quad \tau \le \tau_0 \tag{1.32}$$

It is also possible to implement an LGR between τ_w and τ_0 for increased accuracy in the 1D finite difference calculation. Next, for $\tau > \tau_0$, $w_r(\tau)$ takes the form of a piecewise linear function of τ using a weighted central difference to obtain the nodal values $w_r(\tau_i)$, as shown in Eq. (1.33).

$$w_r(\tau) = \left(\frac{\tau_{i+1}-\tau}{\tau_{i+1}-\tau_{i-1}}\right)\cdot\left(\frac{R(\tau_i)-R(\tau_{i-1})}{\tau_i-\tau_{i-1}}\right)+\left(\frac{\tau-\tau_{i-1}}{\tau_{i+1}-\tau_{i-1}}\right)\cdot\left(\frac{R(\tau_{i+1})-R(\tau_i)}{\tau_{i+1}-\tau_i}\right), \quad \tau_{i-1} \le \tau \le \tau_i \tag{1.33}$$

For the first node, $w_r(\tau_1)$, the reference value of $(0,0)$ is used for τ and $R(\tau)$. For the last interval, we use a backwards difference to calculate $w_r(\tau_N)$. In the following section, we consider discretization of flux and the definition of transmissibility based on the 1D grid and the piecewise linear $w_r(\tau)$ specified here.

1.6.3. Transmissibility

By taking the volume integral of Eq. (1.9), the 1D diffusivity equation can be written as Eq. (1.34).

$$\begin{aligned} c_{t,i}\Delta V_{p,i}\frac{dp_i(t)}{dt} - q(\tau,t)\Big|_{\tau_{i-1}}^{\tau_i} &= 0, \qquad i = 0,\ldots,N \\ q(\tau_i,t) &= \lambda_{rt}(S_{i+1})\cdot T_i \cdot (p_{i+1}-p_i), \quad i = 0,\ldots,N-1 \end{aligned} \tag{1.34}$$

The indexing follows Figure 5. Here, the outer boundary flux vanishes, $q(\tau_N, t) = 0$, and the inner boundary flux is given by the Well Index, $q(\tau_w, t) = \lambda_{rt}(S_0) \cdot WI \cdot (p_0 - p_{wf})$ FMM-SIM solves this system numerically, while FMM-DTOF solves the diffusivity equation by means of the asymptotic pressure approximation. Saturation is evaluated in the upstream cell, $i+1$. Here, T_i represents the intercell transmissibility, which can be obtained using adjacent half cell transmissibilities.

$$\frac{1}{T_i} = \frac{1}{T_i^{Plus}} + \frac{1}{T_{i+1}^{Minus}}, \quad i = 0, \ldots, N-1 \tag{1.35}$$

Here, T_i^{Minus} and T_i^{Plus} denote the half cell transmissibility for cell (or interval) "*i*" in the minus and plus direction, as shown in Figure 7.

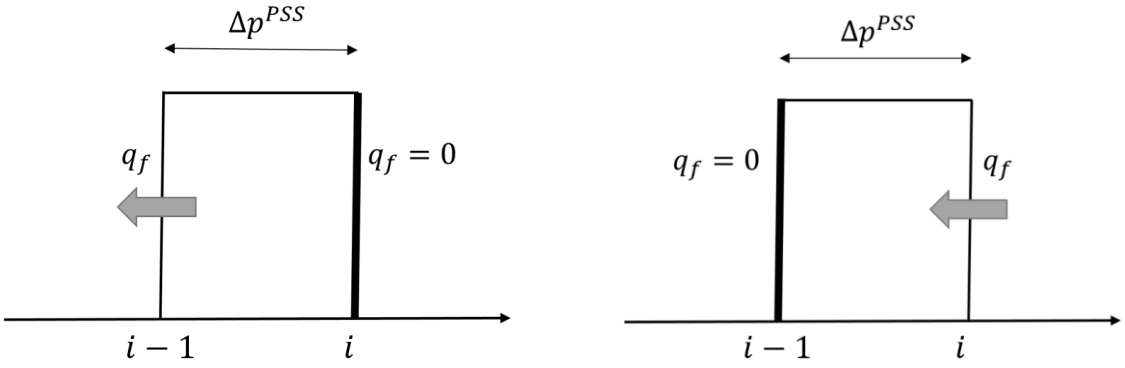

Figure 7 Boundary Conditions for Half Cell Transmissibility

In this section, we derive the half cell transmissibility based on the discretized representations of $V_p(\tau)$ and $w_r(\tau)$. In the flow equation, transmissibility is an intrinsic property, so we consider a single phase and PSS flow to derive the half cell transmissibility. From previous studies (Nunna & King, 2020; Nunna, Liu, & King, 2018), the half cell transmissibility can be obtained by

setting up a no flow boundary on the other face of the half cell transmissibility we want to calculate. By its definition, the transmissibility can be expressed in terms of the PSS pressure drop for uniform relative mobility and compressibility.

$$\lambda_{rt} \to 1/\mu \quad p(\tau,t) \to p^{PSS}(\tau,t) \tag{1.36}$$

Under this condition, the discrete form of 1D Darcy flux in a local interval at PSS can be written as Eq. (1.37) by integrating Darcy's equation, Eq. (1.12), for Δp^{PSS}, once we know the PSS flux, $q^{PSS}(\tau)$.

$$q_f = \frac{1}{\mu} T_f \cdot \Delta p^{PSS} \tag{1.37}$$

Here, we first consider the half cell transmissibility of cell *i* at $\tau = \tau_{i-1}$ (T_i^{Minus}). The boundary conditions, pressure difference and face flux are described in the left hand side of Figure 7.

The pressure at a location of τ with the no flow boundary on the other face can be expressed as Eq. (1.38).

$$p^{PSS}(\tau) = p(\tau_{i-1}) + \mu \int_{\tau'=\tau_{i-1}}^{\tau} \frac{q^{PSS}(\tau')}{w_r(\tau')} d\tau' \tag{1.38}$$

Here, $q^{PSS}(\tau)$ denotes the PSS flux within the interval $\tau_{i-1} \le \tau \le \tau_i$, which can be obtained from Eq. (1.23) in the long time limit. For the minus direction flux, $q = q_f$ on the flowing face, τ_{i-1}, and vanishes on the other cell face.

$$q^{PSS}(\tau) = q_f \cdot \left(\frac{V_p(\tau_i) - V_p(\tau)}{V_p(\tau_i) - V_p(\tau_{i-1})} \right) \tag{1.39}$$

Substituting Eq. (1.39) into Eq. (1.38), the minus direction half cell transmissibility at $\tau = \tau_{i-1}$ can be written as Eq. (1.40).

$$\frac{1}{T_i^{Minus}} \equiv \frac{\Delta p^{PSS}}{\mu q_f} = \int_{\tau=\tau_{i-1}}^{\tau_i} \frac{1}{w_r(\tau)} \frac{V_p(\tau_i) - V_p(\tau)}{V_p(\tau_i) - V_p(\tau_{i-1})} d\tau \tag{1.40}$$

In the same manner, we can derive the plus direction half cell transmissibility for the $\tau = \tau_i$ face.

The boundary conditions, pressure difference and face flux are described in the right hand side of Figure 7. In this boundary condition, q_f means the face flux at $\tau = \tau_i$.

$$q(\tau) = q_f \cdot \left(\frac{V_p(\tau) - V_p(\tau_{i-1})}{V_p(\tau_i) - V_p(\tau_{i-1})} \right) \tag{1.41}$$

$$\frac{1}{T_i^{Plus}} \equiv \frac{\Delta p^{PSS}}{\mu q_f} = \int_{\tau=\tau_{i-1}}^{\tau_i} \frac{1}{w_r(\tau)} \frac{V_p(\tau) - V_p(\tau_{i-1})}{V_p(\tau_i) - V_p(\tau_{i-1})} d\tau \tag{1.42}$$

For the first interval, we use quadratic $V_p(\tau)$ and linear $w_r(\tau)$ to obtain the known solution for a radial flow geometry (Schlumberger, 2019a). Expressed in terms of τ:

$$\frac{1}{WI} = \frac{1}{T_0^{Minus}} = \frac{\frac{\tau_0^2}{\tau_0^2 - \tau_w^2} \ln\left(\frac{\tau_0}{\tau_w}\right) - 0.5}{2\pi \sum_{ijk}^{Perforation} [kh]_{ijk}} \tag{1.43}$$

$$\frac{1}{T_0^{Plus}} = \frac{0.5 - \frac{\tau_w^2}{\tau_0^2 - \tau_w^2} \ln\left(\frac{\tau_0}{\tau_w}\right)}{2\pi \sum_{ijk}^{Perforation} [kh]_{ijk}} \tag{1.44}$$

Next, we consider deriving the transmissibility for the remaining intervals. For piecewise linear representations of $V_p(\tau)$ and $w_r(\tau)$, we obtain:

$$\frac{1}{T_i^{Minus}} = \frac{\tau_i - \tau_{i-1}}{w_r(\tau_i) - w_r(\tau_{i-1})} \left\{ \frac{w_r(\tau_i)}{w_r(\tau_i) - w_r(\tau_{i-1})} \ln\left(\frac{w_r(\tau_i)}{w_r(\tau_{i-1})} \right) - 1 \right\} \tag{1.45}$$

$$\frac{1}{T_i^{Plus}} = \frac{\tau_i - \tau_{i-1}}{w_r(\tau_i) - w_r(\tau_{i-1})} \left\{ 1 - \frac{w_r(\tau_{i-1})}{w_r(\tau_i) - w_r(\tau_{i-1})} \ln\left(\frac{w_r(\tau_i)}{w_r(\tau_{i-1})} \right) \right\} \tag{1.46}$$

If the change in $w_r(\tau)$ is sufficiently small, $\left|\frac{w_r(\tau_i)-w_r(\tau_{i-1})}{w_r(\tau_i)+w_r(\tau_{i-1})}\right| < TOL = 10^{-6}$, then we replace these equations with their value in this limit.

$$\frac{1}{T_i^{Minus}} = \frac{1}{T_i^{Plus}} \approx \frac{\Delta\tau_i}{w_r(\tau_i)+w_r(\tau_{i-1})} \tag{1.47}$$

This transmissibility is used for the finite difference simulation (FMM-SIM), and also used to calculate the pressure profile with the asymptotic approach (FMM-DTOF).

Using the half cell transmissibilities derived, the pressure equation is shown as Eq. (1.48) in the discrete form.

$$\begin{aligned} p(\tau_i,t) &= p_{wf}(t) + \int_{\tau'=\tau_w}^{\tau_i} \frac{q(\tau',t)}{\lambda_{rt}(S_j)w_r(\tau')}d\tau' \\ &= p_{wf}(t) + \sum_{j=0}^{i}\left\{\frac{q(\tau_{j-1},t)}{\lambda_{rt,j}(S_j)T_j^{Minus}} + \frac{q(\tau_j,t)}{\lambda_{rt,j}(S_j)T_j^{Plus}}\right\} \end{aligned} \tag{1.48}$$

Here, $\lambda_{rt,j}$ is a function of the initial saturation and pressure in the cell interval "*j*" in the FMM-DTOF calculation. In FMM-SIM, it is a function of saturation and pressure. The face flux q is obtained by Eq. (1.27). Here, the calculation process of the second term in Eq. (1.27) requires the evaluation of the following integral as part of the calculation of the analytic flux.

$$\int_{\tau_a}^{\tau_b} e^{-\tau^2/4t}\frac{dV_p}{d\tau}d\tau \tag{1.49}$$

For the radial portion of the grid:

$$\int_{\tau_a}^{\tau_b} e^{-\tau^2/4t}\frac{dV_p}{d\tau}d\tau = \frac{2\pi kh}{\mu c_t}\int_{\tau_a}^{\tau_b} e^{-\tau^2/4t}\tau d\tau = \frac{4\pi kh}{\mu c_t}t\left(e^{-\tau^2/4t}\Big|_{\tau_b}^{\tau_a}\right) \tag{1.50}$$

For the piecewise linear portion of the grid:

$$\int_{\tau_a}^{\tau_b} e^{-\tau^2/4t}\frac{dV_p}{d\tau}d\tau = \frac{\Delta V_p}{\Delta\tau}\int_{\tau_a}^{\tau_b} e^{-\tau^2/4t}d\tau = \sqrt{\pi t}\left(\frac{\Delta V_p}{\Delta\tau}\right)\left(erfc\left(\frac{\tau}{2\sqrt{t}}\right)\Big|_{\tau_b}^{\tau_a}\right) \tag{1.51}$$

In the case of FMM-DTOF, Eq. (1.50) is applied for $\tau \le \tau_0$ and Eq. (1.51) is used for $\tau > \tau_0$.

Equally, the average pressure where $\tau \le \tau_i$ can expressed in the discrete form as Eq. (1.52).

$$\bar{p}(\tau_i, t) = p_{wf}(t) + \frac{1}{V_p(\tau_i) - V_p(\tau_w)} \sum_{j=0}^{i} \Delta V_{p,j} \cdot \left\{ \frac{q(\tau_{j-1}, t)}{\lambda_{rt}(S_j) T_j^{Minus}} + \frac{q(\tau_j, t)}{\lambda_{rt}(S_j) T_j^{Plus}} \right\} \tag{1.52}$$

The average pressure of the entire reservoir can be derived by taking $\tau_i = \tau_{\max}$ in this equation.

1.7. Case Studies

1.7.1. Single Well Synthetic Case: Homogeneous

- Input

A 2D homogeneous reservoir model is examined as the first case study. The fluid type used in the model is single phase dead oil.

Table 2 Reservoir Properties (2D Homogeneous)

Grid	[300, 300, 1]	[-]
ΔX	600	[ft]
ΔY	600	[ft]
ΔZ	300	[ft]
ϕ	0.01	[-]
k	1	[mD]
c_f	1.0e-6	[1/psi]
p_{init}	5200	[psia]
$S_{w,init}$	0	[-]

Table 3 Fluid Properties 1

Fluid Type	Dead Oil	[-]
B_o	1.14	[bbl/STB]
μ	1.185	[cp]
c_o	1.07e-5	[1/psi]

Table 4 Well Properties (2D Homogeneous)

Well Type	Vertical	[-]
Location	[121, 150, 1]	[-]
Target Rate	300	[STB/D]
BHP Constraint	14.7	[psia]

- Result

The $w_r(\tau)$ profile along τ is shown in Figure 8. $w_r(\tau)$ represents the derivative of $R(\tau)$. As we can see in Eq. (1.32), $w_r(\tau)$ has a linear relationship with τ in the near well region. Even beyond τ_0, it increases proportionally to τ in the 2D homogeneous model. This is because the coefficient of τ is uniform under the homogeneous distribution for infinite acting radial flow. Once the pressure front hits the reservoir boundary, the increment of $w_r(\tau)$ decreases due to the finite reservoir volume (≈ 1600 hr$^{0.5}$). Once the boundary effect starts to appear, $w_r(\tau)$ is no longer linear with τ, and it drops gradually close to zero.

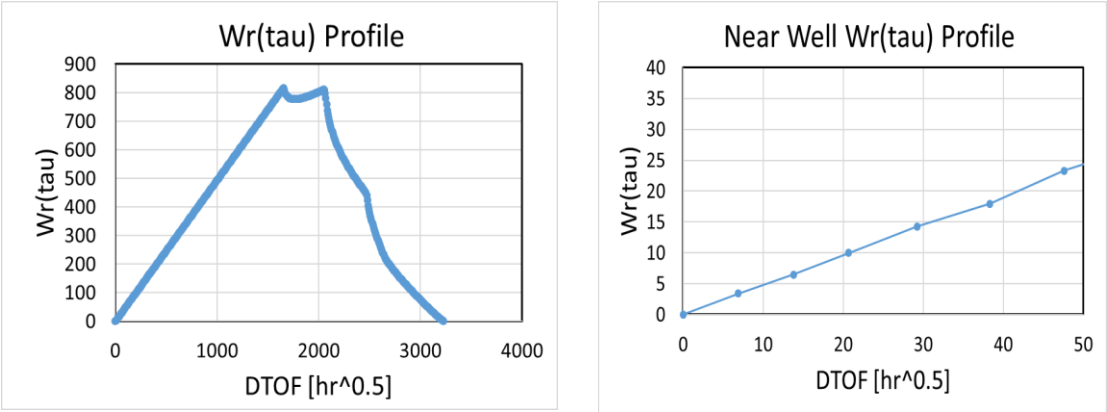

Figure 8 $w_r(\tau)$ Profile of a 2D Homogeneous Model

Next, we make a comparison of the pressure transient profiles. Here, we have two reference calculations in the figure: ECL and E1. Eclipse (ECL) is a numerical reservoir

simulator (Schlumberger, 2019b) and E1 is the analytical solution for infinite acting radial flow (Lee, 1982; Lee et al., 2003). In Figure 9, the black line and blue circles represent the E1 analytical solution and the numerical solution based on ECL, respectively. The green dash vertical line denotes the beginning of PSS at the Peaceman radius, r_0 (Gunasekera, Cox, & Lindsey, 1997; D. W. Peaceman, 1978; Donald W. Peaceman, 1983). This is the time when the transients within the finite volume of the Peaceman radius can be ignored and ECL becomes accurate against the analytical solution. Peaceman's analysis for the effective wellbore radius assumes that PSS is reached in the well cells, so it cannot accurately represent the pressure decline trend at times earlier than t_{PSS}. This time can be obtained from the following analysis. First, we calculate τ at the Peaceman radius for each perforation.

$$\tau_{p,i} = \frac{1}{4} e^{-\gamma} \sqrt{\frac{\Delta x_i^2}{\alpha_{x,i}} + \frac{\Delta y_i^2}{\alpha_{y,i}}}, \quad \textit{Vertical Well} \tag{1.53}$$

Here, γ is the Euler-Mascheroni constant (Donald W. Peaceman, 1983). The derivation for the average τ_p for the 1D τ discretization requires that the Well Index be the same as the sum over multiple perforations.

$$WI = \sum_{ijk} WI_{ijk} \quad \Rightarrow \quad \frac{\sum_{ijk} (kh)_{ijk}}{\ln\left(\tau_p / \tau_w\right)} = \sum_{ijk} \frac{(kh)_{ijk}}{\ln\left(\tau_{p,ijk} / \tau_{w,ijk}\right)} \tag{1.54}$$

Lastly, the corresponding time when the transient near well pressure drop becomes equivalent to the steady state Peaceman WI, can be obtained from his paper (D. W. Peaceman, 1978). Peaceman defined the dimensionless time in terms of the cell dimension on an isotropic grid as Eq. (1.55).

$$t_D = \frac{kt}{\phi \mu c_t \Delta x^2} \tag{1.55}$$

He demonstrated the accuracy of the Peaceman WI once $t_D \approx 1$, in other words, once the radius of investigation reaches the center of the adjacent cell. This time is also equal to the time at which PSS flow is achieved at the Peaceman radius, τ_p, Eq. (1.56).

$$t_{PSS} = 25\tau_p^2 \tag{1.56}$$

This is consistent with Peaceman's steady state WI construction which ignores transient pressure effects within the radius r_0. A finite difference simulator using Peaceman's WI is expected to have reduced accuracy earlier than this time.

From the figure, it can be observed that the E1 analytical solution is more accurate than ECL at the very early time when the well block of the numerical simulation has not reached PSS, but the E1 analytical solution does not follow the pressure drop once the reservoir boundary effect starts to appear.

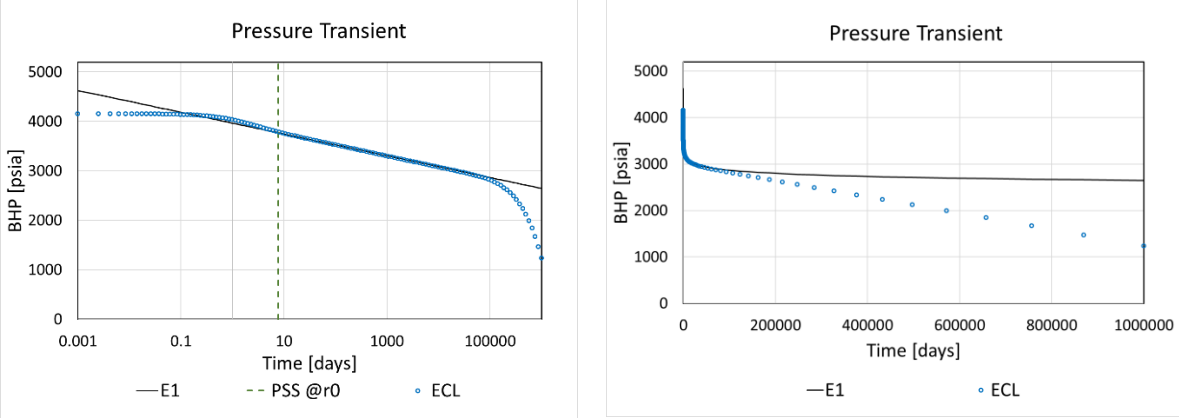

Figure 9 Pressure Transient Profiles based on Commercial Software and E1 Analytical Solution

In comparison with these two references, the BHP comparison between FMM-DTOF and ECL is shown in Figure 10. The red line correspond to FMM-DTOF result. The left figure shows the pressure transient profile along with log scale of production time, and the right along with linear scale, respectively.

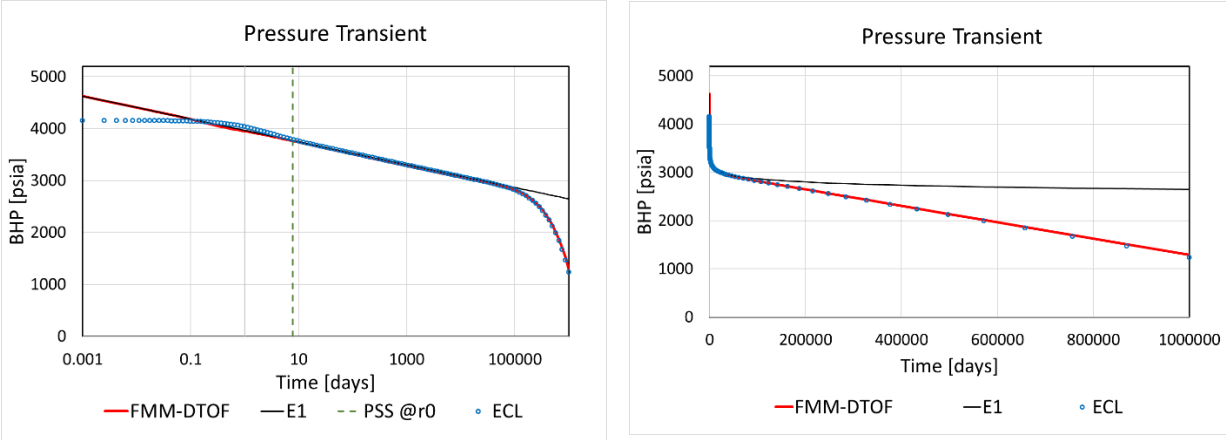

Figure 10 Pressure Transient for Fixed Rate Drawdown of a Homogeneous Single Well Reservoir: Logarithmic Scale (left) & Linear Scale (right)

In the above figure, we can see that FMM-DTOF matches perfectly the E1 solution at the very early time. Once the boundary effect starts appearing, FMM-DTOF begins to follow ECL accurately. This can be a validation that FMM-DTOF model is implemented correctly in the simulation study.

1.7.2. Single Well Synthetic Case: Heterogeneous

- Input

In this case study, the spatial heterogeneity is introduced to the reservoir model used in the previous study. The same fluid type as the previous case study is used. The permeability field and the DTOF are described as described in Figure 11. Here, as an indicator of the level of heterogeneity, we use Dykstra Parsons coefficient V_{DP} (Dykstra & Parsons, 1950). According to the definition, the reservoir with $V_{DP} = 0.64$ is categorized into a "very heterogeneous" reservoir.

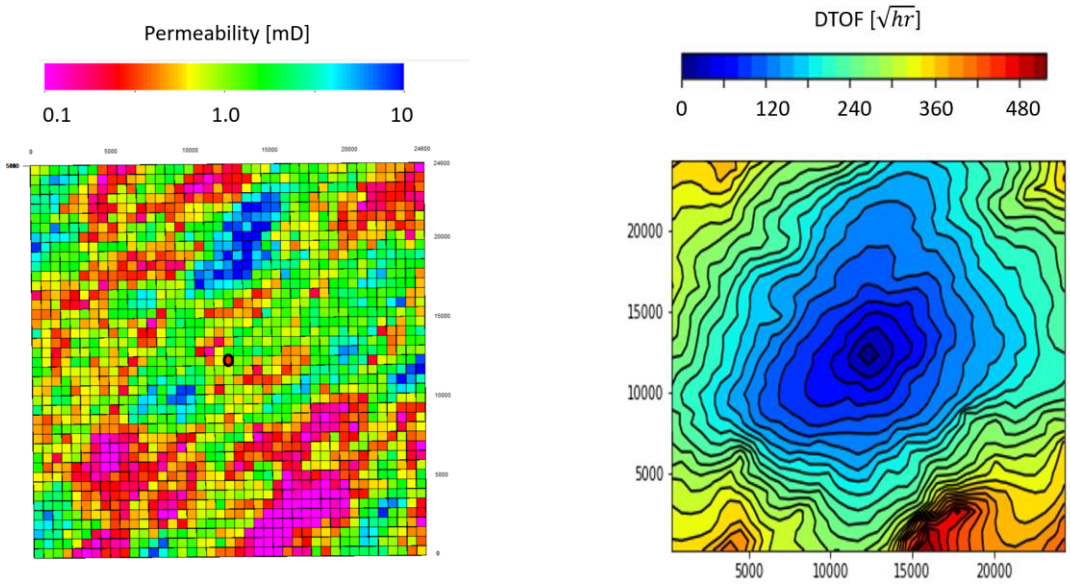

Figure 11 Heterogeneous Model, Table 5

Table 5 Reservoir Properties (2D Heterogeneous)

Grid	[41, 41, 1]	[-]
ΔX	600	[ft]
ΔY	600	[ft]
ΔZ	150	[ft]
ϕ	0.01	[-]
V_{DP}	0.64	[-]
c_f	1.0e-6	[1/psi]
p_{init}	5200	[psia]
$S_{w,init}$	0	[-]

Table 6 Well Properties (2D Heterogeneous)

Well Type	Vertical	[-]
Location	[21, 21, 1]	[-]
Target Rate	50	[STB/D]
BHP Constraint	14.7	[psia]

- Result

$w_r(\tau)$ profile along τ is shown in Figure 12. Since the reservoir model is heterogeneous, $w_r(\tau)$ is not a strictly linearly function near the well, and shows a more complex structure due to the heterogeneity and the reservoir boundary effect. Next, the pressure transient comparison between FMM-DTOF and ECL is shown in Figure 13. The blue dots and the red line correspond to ECL and FMM-DTOF results, respectively. In this figure, the green vertical dash line denotes the beginning of PSS at the well block, since ECL is only expected to be accurate after this time, while the FMM-DTOF is accurate at early time.

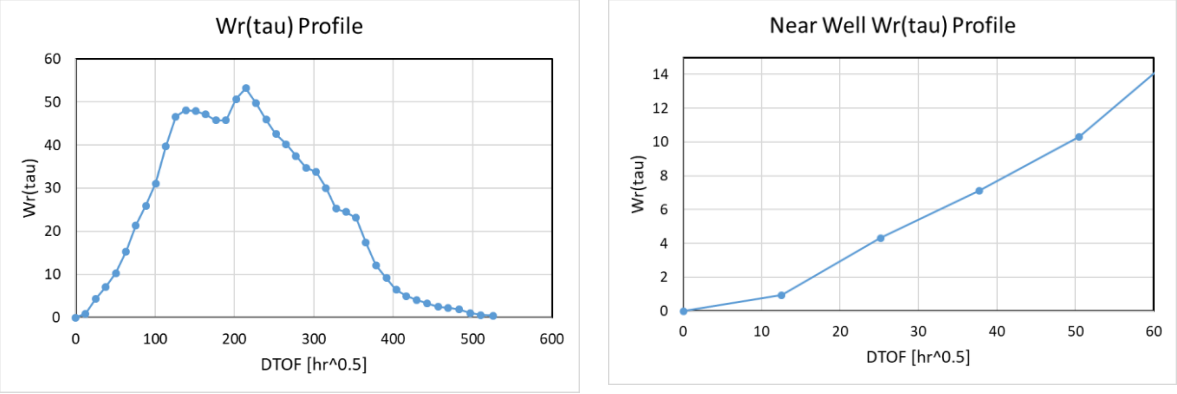

Figure 12 $w_r(\tau)$ Profile of a 2D Heterogeneous Model

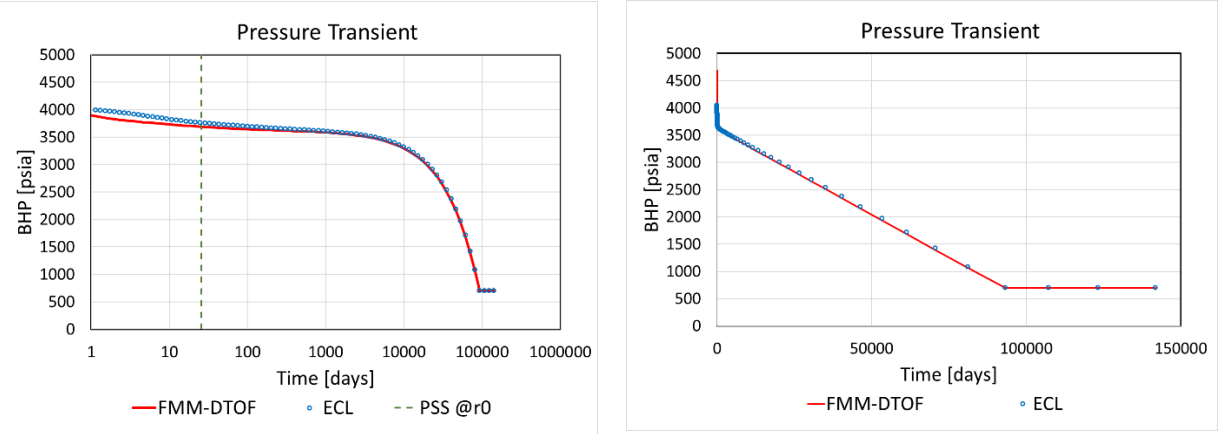

Figure 13 Pressure Transient for Fixed Rate Drawdown of a Heterogeneous Single Well Reservoir: Logarithmic Scale (left) & Linear Scale (right)

From the above figure, we can see that although there is a small mismatch at the very early time from ECL, FMM-DTOF is matching ECL well after the beginning of PSS at the well block (25 days), and up to an including the boundary effects. The reason of the mismatch at the very early time is because Peaceman's analysis for the effective wellbore radius assumes that PSS is reached in the well cell.

1.7.3. Single Well Sector Model

- Input

In this case study, the methodology developed in Section 1.4 is applied to a sector model. This sector model is provided by one of our industrial partners as part of a joint research project with the MCERI JIP. Table 7 and Table 8 summarize the reservoir and well properties, respectively. Unlike Section 1.7.2, the production well is perforated in multiple layers: Layer 1 to Layer 27. The reservoir fluid has the same properties as the previous case study shown in Table 3. The permeability field is described in Figure 14. The histograms of permeability and porosity are described in Figure 15 and Figure 16. As shown in Figure 15, there are two groups of

permeability/porosity distributions: high and low. The group with high permeability/porosity ranges between layer 1 and layer 27, where the production well is completed. The other group with low permeability/porosity is below layer 27, where the production well is not completed. In this model, the top zone group makes a major contribution to the well performance compared to the bottom zone group. Since V_{DP} is a measurement for a degree of heterogeneity for a unimodal permeability distribution, since the model has a bimodal distribution, we calculated V_{DP} for the highly productive zone (cut-off value is 1 mD). The value of $V_{DP} = 0.86$ indicates strong heterogeneity in the productive zones.

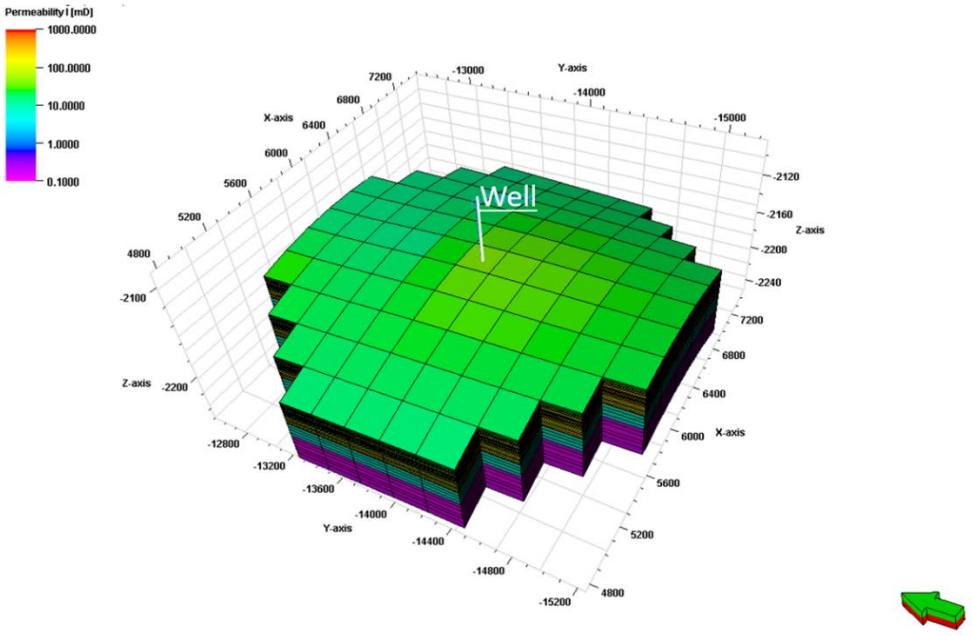

Figure 14 Single Well Field Model, Table 7

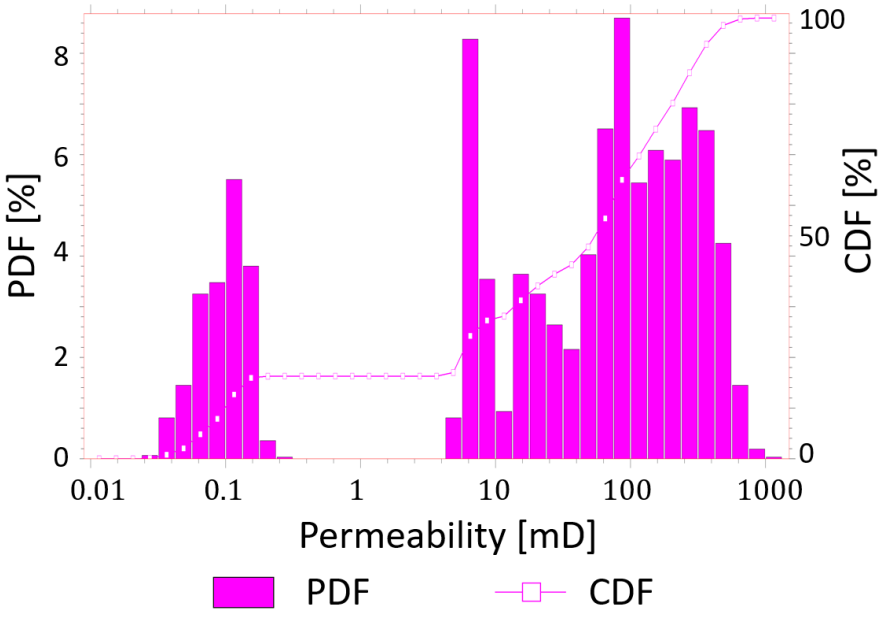

Figure 15 Permeability Histogram, Table 7

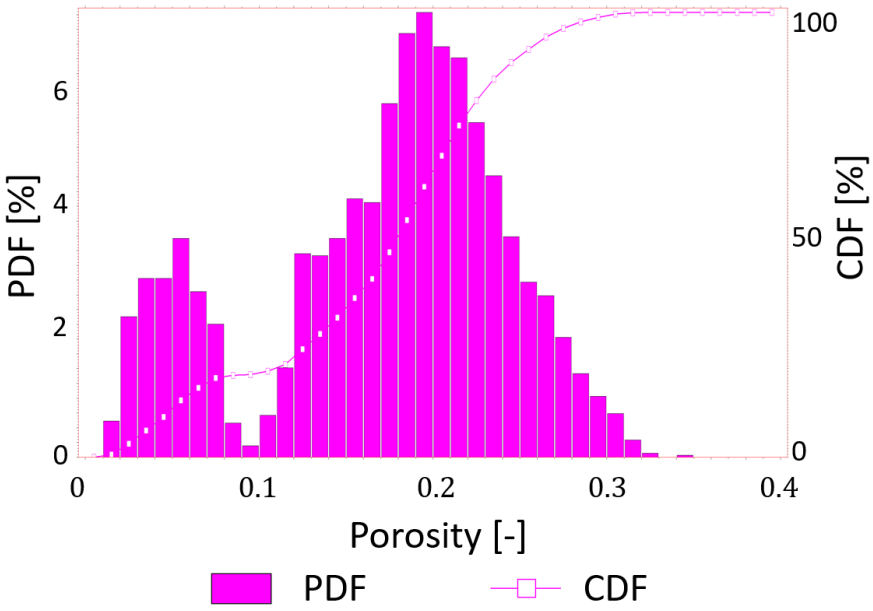

Figure 16 Porosity Histogram, Table 7

Table 7 Reservoir Properties (3D Sector Model)

Grid	[11, 11, 32]	[-]
ΔX	250	[ft]
ΔY	250	[ft]
ΔZ	0.5 - 10	[ft]
$\bar{\phi}$	0.18	[-]
V_{DP}	0.86	[-]
c_f	1.0e-6	[1/psi]
p_{init}	5200	[psia]
$S_{w,init}$	0	[-]

Table 8 Well Properties (3D Sector Model)

Well Type	Vertical	[-]
Location	[6, 6, 1-27]	[-]
Target Rate	100	[STB/D]
BHP Constraint	2000	[psia]

- Result

$w_r(\tau)$ profile along τ is shown in Figure 17. Since the reservoir model is heterogeneous, $w_r(\tau)$ is not a strictly linear function, even for small τ in the near well region, and starts to go down once the reservoir boundary effect appears. Next, the pressure transient comparison between FMM-DTOF and ECL is shown in Figure 18. The blue dots and the red line correspond to ECL and FMM-DTOF results, respectively. The time for Peaceman radius to reach PSS is 0.09 day, so the ECL based well performance is supposed to be accurate from the very early time.

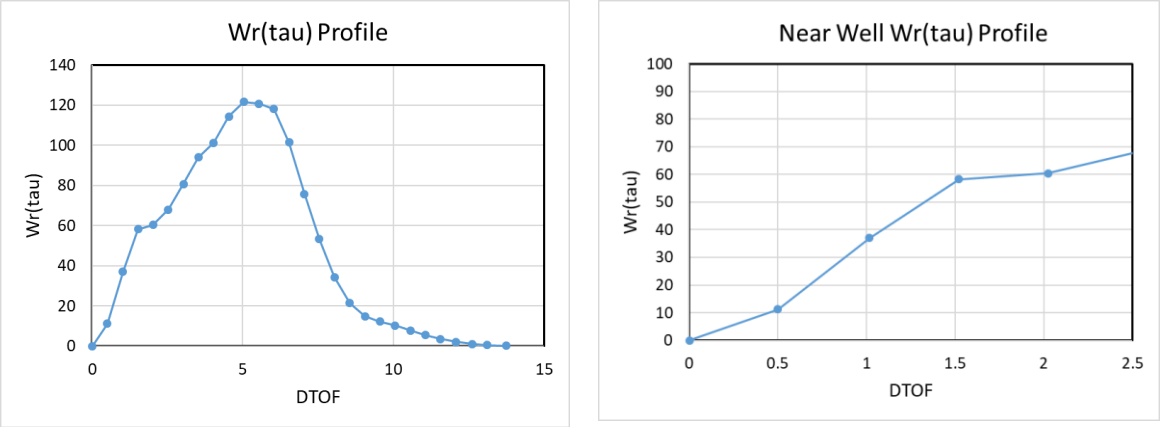

Figure 17 $w_r(\tau)$ Profile of a Single Well Sector Model

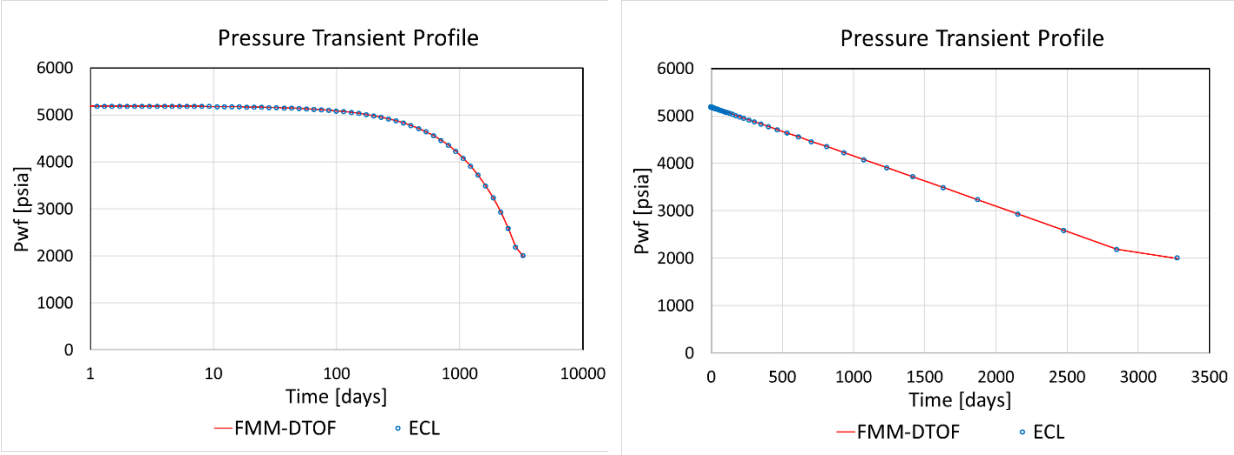

Figure 18 Pressure Transient for Fixed Rate Drawdown of a Single Well Sector Model: Logarithmic Scale (left) & Linear Scale (right)

From the above figure, we can see that FMM-DTOF is working extremely well even in the case of a multi-completion well with strong heterogeneity. This case study result demonstrates that the methodology developed in Section 1.4 is applicable for a 3D reservoir model with a multiple perforation well under very heterogeneous permeability field.

2. FMM MULTIPLE WELLS DEVELOPMENT

2.1. Asymptotic Equation Systems: Superposition Approach

In this section, first we express the pressure at a location τ from the initial reservoir pressure in the case of a single well.

$$p(\tau,t) = \left(p(\tau,t) - p_{wf}(t)\right) - \left(\bar{p}(t) - p_{wf}(t)\right) - \left(p_{init} - \bar{p}(t)\right) + p_{init} \tag{2.1}$$

Here, the first, second and third term can be obtained from Eq. (1.17), Eq. (1.19), Eq. (1.21), respectively. The flux term $q(\tau,t)$ can be expressed as a product of total flux and the dimensionless reservoir flux, Eq. (1.27). $\Delta V_{p,\max}$ is the total connected reservoir pore volume. $Q(t)$ is the cumulative total fluid production. λ_{rt} is a function of the initial saturation averaged to the resolution of τ.

In the case of multiple well reservoir models, we need to consider pressure drops from the initial reservoir pressure attributed to every well. For instance, let us consider a reservoir model which has two production wells: A and B. We would like to calculate the total pressure drop at a location marked with a star in Figure 19. The total pressure drop from the initial reservoir pressure in this case is obtained by summing both pressure drops from Well A and from Well B.

$$\delta p_{total} = \delta p_A + \delta p_B \tag{2.2}$$

Here, δp_A and δp_B are pressure drops from the initial reservoir pressure p_{init} due to each well (A or B). δp_{total} is the total pressure drop from p_{init}. In order to calculate each pressure drop, we consider two different τ coordinates: Coordinate A (shown as gray contours) and Coordinate B (shown as blue contours).

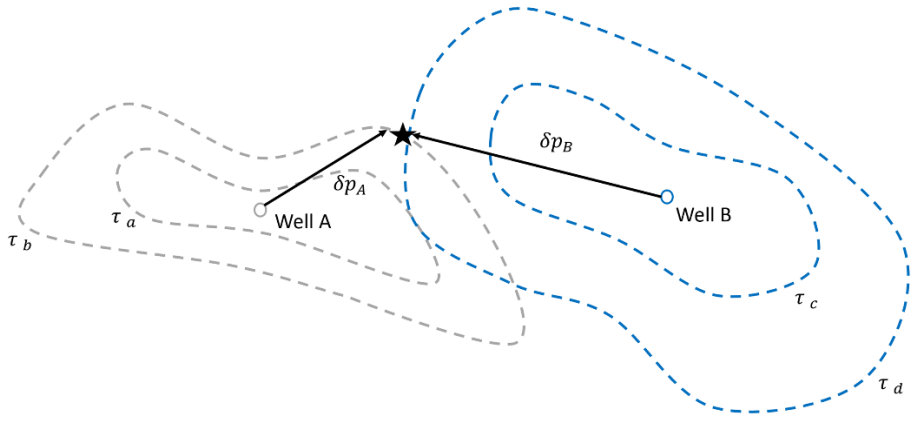

Figure 19 Superposition Method

In Coordinate A, we ignore Well B and all DTOF's are obtained from Well A. The pressure drop, we call δp_A, can be calculated in the same manner as the single well case shown as Eq. (1.22). Equally, we can calculate the pressure drop, δp_B, which is due to Well B, ignoring Well A. In Coordinate B, the target location marked with a star has a different DTOF from the one in Coordinate A. δp_B is expressed using Eq. (2.1). Lastly, the summation of all pressure drops (δp_A and δp_B) provides the total pressure drop at any location.

$$\begin{aligned} p(\vec{x},t) &= p_{init} - \sum_{j=1}^{Wells} \delta p_j \\ &= p_{init} + \sum_{j=1}^{Wells} q_{t,j}(t) \left\{ \int_{\tau'=\tau_{w,j}}^{\tau_j(\vec{x})} \frac{q_{D,j}(\tau',t)}{\lambda_{rt}(S) w_{r,j}(\tau')} d\tau' - J_j^{-1}(t) \right\} - \frac{Q(t)}{c_t \Delta V_{p,\max}} \end{aligned} \tag{2.3}$$

$\Delta V_{p,\max}, q_{D,j}$ are the total drainage pore volume and dimensionless total flux of well *j* at reservoir condition, respectively. $\tau_{w,j}, \tau_j(\vec{x})$ denote the DTOF at the wellbore surface and at the location $\vec{x}$ in the "*j*" coordinate. Likewise to the single well case, λ_{rt} is a function of the initial saturation.

These equations are solved subject to the boundary conditions of the wells, which can be expressed as a target rate subject to a pressure constraint, as in Eq. (2.4).

$$\begin{aligned} &F_i(t)\cdot p_{wf,i}(t)+\left(1-F_i(t)\right)\cdot q_{t,i}(t)=F_i(t)\cdot p_{wf,i}^{\text{constraint}}+\left(1-F_i(t)\right)\cdot q_{t,i}^{\text{target}} \\ &F_i(0)=0 \end{aligned} \tag{2.4}$$

Here, $i=1,...,N$ and N is the total number of wells. In the system, F_i is a flag which takes on the value 0 if a well "i" is controlled by rate and 1 if controlled by BHP. All wells are initialized with values of 0, and switch to 1 when the transient BHP based on rate control reaches lower limit of BHP. In a block matrix form, it is written as Eq. (2.5).

$$\left[\begin{array}{c|ccc|ccc} c_tV_{p,res} & 0 & \cdots & 0 & \Delta t^n & \cdots & \Delta t^n \\ \hline 1 & -1 & & 0 & M_{1,1}^{n+1} & \cdots & M_{1,N}^{n+1} \\ \vdots & & \ddots & & \vdots & & \vdots \\ 1 & 0 & & -1 & M_{N,1}^{n+1} & \cdots & M_{N,N}^{n+1} \\ \hline 0 & F_1^{n+1} & & 0 & 1-F_1^{n+1} & & 0 \\ \vdots & & \ddots & & & \ddots & \\ 0 & 0 & & F_N^{n+1} & 0 & & 1-F_N^{n+1} \end{array}\right]\left[\begin{array}{c} \bar{p}^{n+1} \\ \hline p_{wf,1}^{n+1} \\ \vdots \\ p_{wf,N}^{n+1} \\ \hline q_{t,1}^{n+1} \\ \vdots \\ q_{t,N}^{n+1} \end{array}\right]=\left[\begin{array}{c} c_tV_{p,res}\bar{p}^n \\ \hline 0 \\ \vdots \\ 0 \\ \hline F_1^{n+1}p_{wf,1}^{\text{const}}+\left(1-F_1^{n+1}\right)q_{t,1}^{\text{target}} \\ \vdots \\ F_N^{n+1}p_{wf,N}^{\text{const}}+\left(1-F_N^{n+1}\right)q_{t,N}^{\text{target}} \end{array}\right] \tag{2.5}$$

Here, $M_{i,j}^{n+1}$ is expressed as Eq. (2.6).

$$M_{i,j}^{n+1}=\int_{\tau'=\tau_{w,j}}^{\tau_j(\vec{x}_i)}\frac{q_{D,j}\left(\tau',t^{n+1}\right)}{\lambda_{rt}\left(S\left(\tau',0\right)\right)w_{r,j}\left(\tau'\right)}d\tau'-J_j^{-1}\left(t^{n+1}\right) \tag{2.6}$$

Here, $\tau_j\left(\vec{x}_i\right)$ represents the DTOF of well "i" location under "j" coordinate. The superscript "n" denotes the time level. This matrix problem can be solved based on the average reservoir pressure using the mass balance equation at the previous time step. The flag function is initialized to zero at the $n=0$ time step, and then switches to one once the well control changes to the BHP constraint. In each time steps we use the flags at the previous time step as initial

values, and re-calculate the matrix system, if a well constraint is hit. It is noteworthy that the asymptotic approach does not require to solve any explicit reservoir flow equation, since they are taken care of by the analytic pressure approximation, which leaves only well rate and pressure as unknowns to be solved. In the case of a reservoir model used in Section 2.4, for instance, we have 30,400 cell pressure to solve with a finite difference numerical simulator, correspondingly for each cell, but we only have to solve the matrix system for 11 unknowns (1 for average pressure, 5 for production rate and 5 for BHP of each well)

2.2. Multiple Well Synthetic Case Study: Homogeneous

- Input Data

As the first step for the validation of the model, the asymptotic pressure system is tested against a 2D homogeneous reservoir model. The grid, reservoir and fluid properties are the same as the single well case study (Table 5 with homogeneous permeability and Table 3). The reservoir model has two production wells at the locations shown in the tables below (Table 9). The second production well has double the production rate compared to the first production well and both wells have the same BHP constraint of 700 psia. They are put symmetrically in the 2D homogeneous reservoir as described in Figure 20.

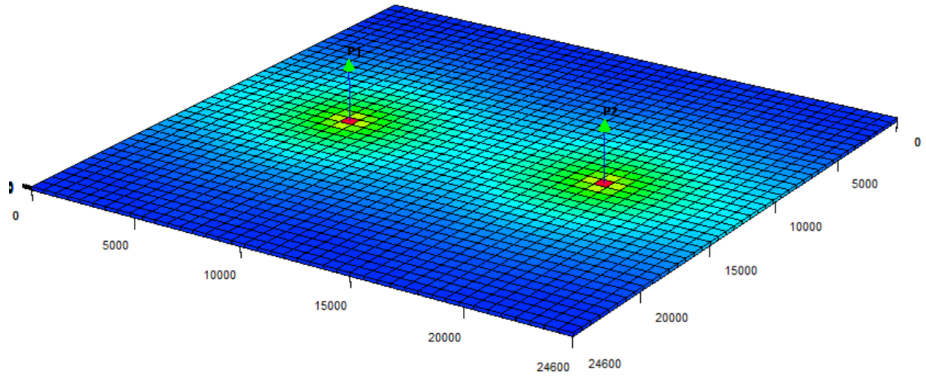

Figure 20 Multiple Well Homogeneous Case

Table 9 Multiple Well Production Well Descriptions

P1		
Well Type	Vertical	[-]
Location	[11, 21, 1]	[-]
Target Rate	30	[STB/D]
BHP Constraint	700	[psia]
P2		
Well Type	Vertical	[-]
Location	[31, 21, 1]	[-]
Target Rate	60	[STB/D]
BHP Constraint	700	[psia]

- Results

$w_r(\tau)$ profile along τ is shown in Figure 21. Since the reservoir model is homogeneous and two production wells are put symmetrically, the $w_r(\tau)$ profiles are the same for both of the production wells. The $w_r(\tau)$ profile looks similar to the single well homogeneous case shown in the previous section. Next, the pressure and rate comparison between FMM-DTOF and ECL is

shown in Figure 22. The blue plots and red lines correspond to ECL and FMM-DTOF simulation results, respectively.

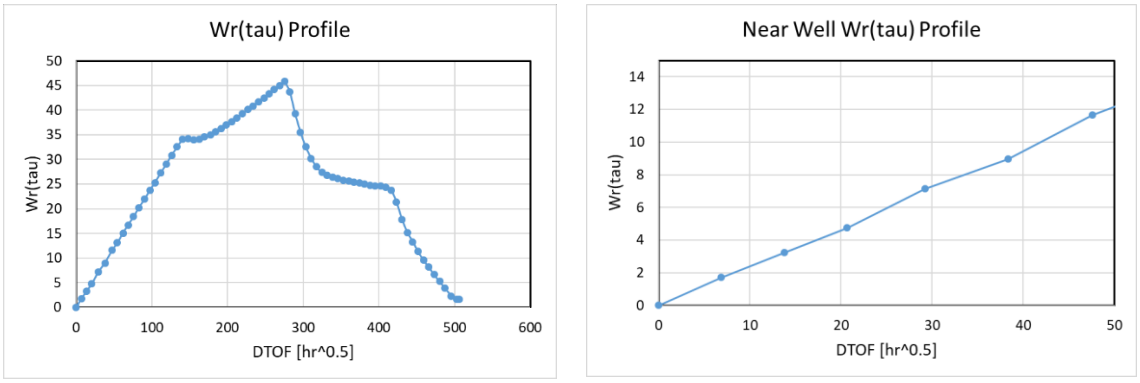

Figure 21 $w_r(\tau)$ Profiles of a Multiple Well 2D Homogeneous Model

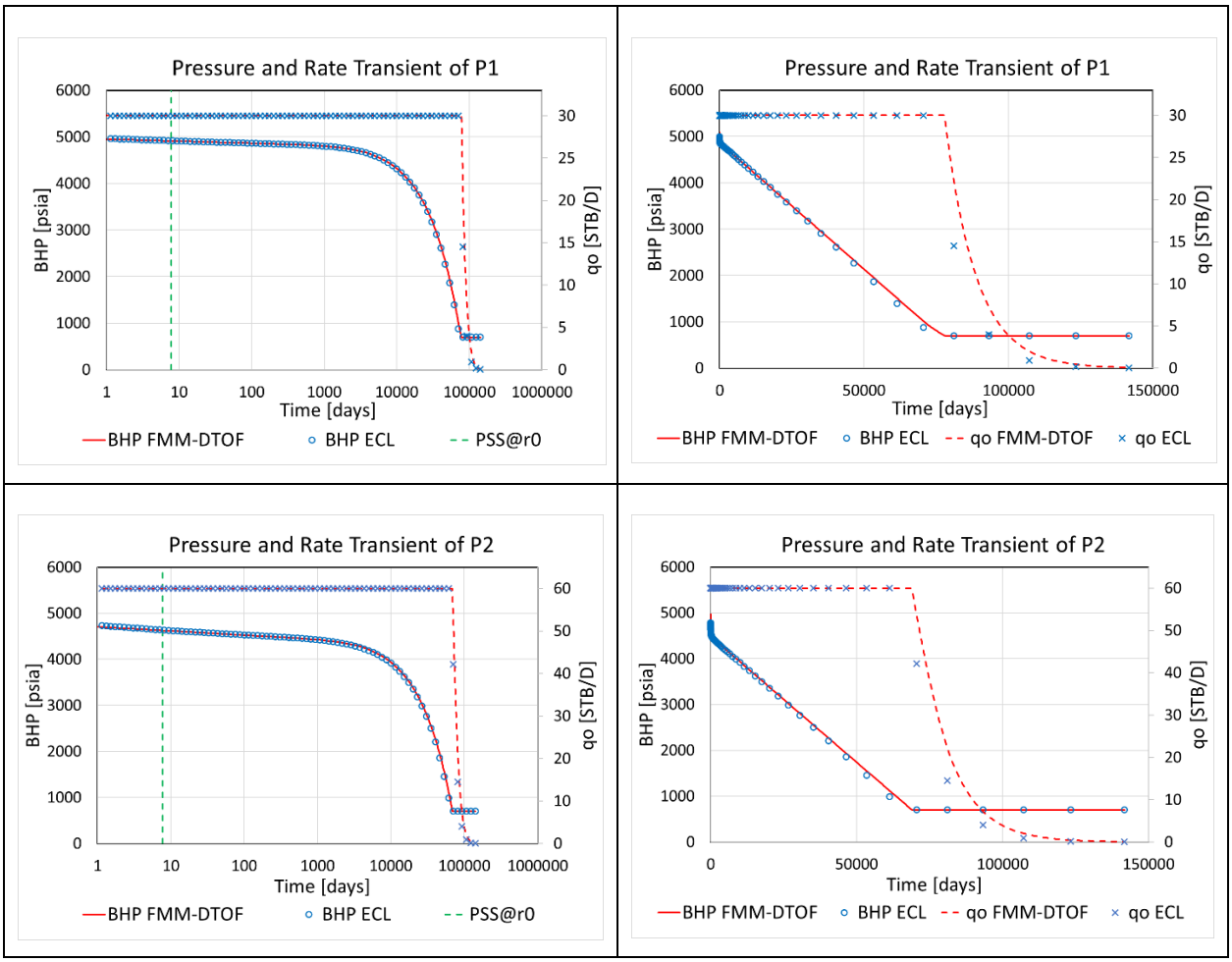

Figure 22 Pressure and Rate Transient for a 2D Homogeneous Multiple Well Reservoir

In this case study, we took the time step logarithmically up to a certain point, and then fixed the step size as a constant after that. This is because FMM-DTOF calculates the average reservoir pressure explicitly, so we can make sure the solutions of the system are converged in this way. Both wells start producing oil with target rate at first, and they switch to BHP constraint (700 psia) at late time. Both wells have good matches in BHP against ECL. Compared to the BHP, the rate has small mismatch against ECL in both cases, but this is because the rate drop is sharp, so it is sensitive to the exact time when the well switches from the BHP control to rate control. However, by and large, we can see that FMM-DTOF follows the trend of ECL for both of the production wells. This is the starting point for application of asymptotic solution for multi-well models with heterogeneity studied in the next section.

2.3. Multiple Well Synthetic Case Study: Heterogeneous

- Input Data

As a next step for the validation of the multi-well model, the spatial heterogeneity is introduced to the reservoir model used in the previous section. The grid, fluid, well location and production control are the same as the previous case study used for the homogeneous multi-well case study (Table 5, Table 3 and Table 9 for reservoir, fluid properties and well properties).

- Results

$w_r(\tau)$ profile along τ is shown in Figure 23 and Figure 24 for P1 and P2, respectively. The $w_r(\tau)$ profile for P2 around the wellbore has a steeper gradient compared to P1. Next, the well behavior comparison between FMM-DTOF and ECL is shown in Figure 25, left for P1 and right P2, respectively. The blue plots and red lines correspond to ECL and FMM-DTOF results

in each figure. As in the previous sections, the green vertical dash line denotes the beginning of PSS at the well block.

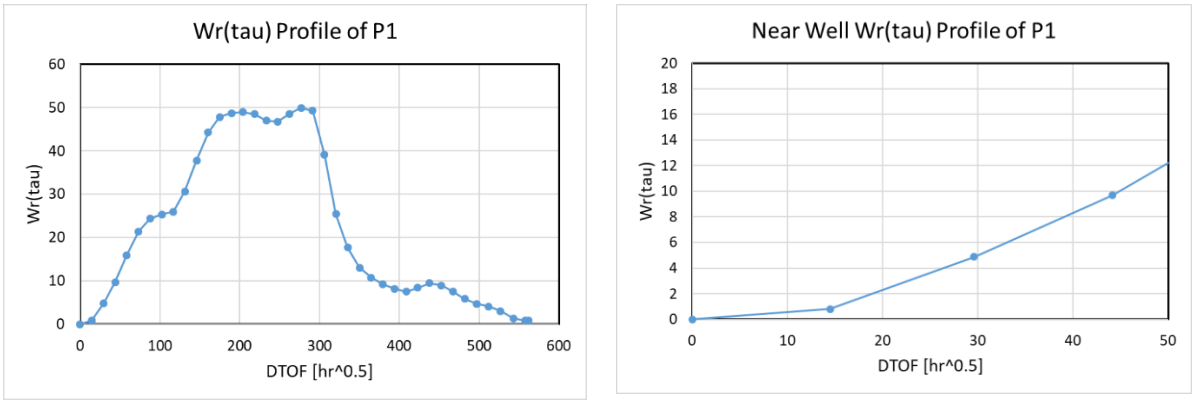

Figure 23 $w_r(\tau)$ Profiles of a Multiple Well 2D Heterogeneous Model (P1)

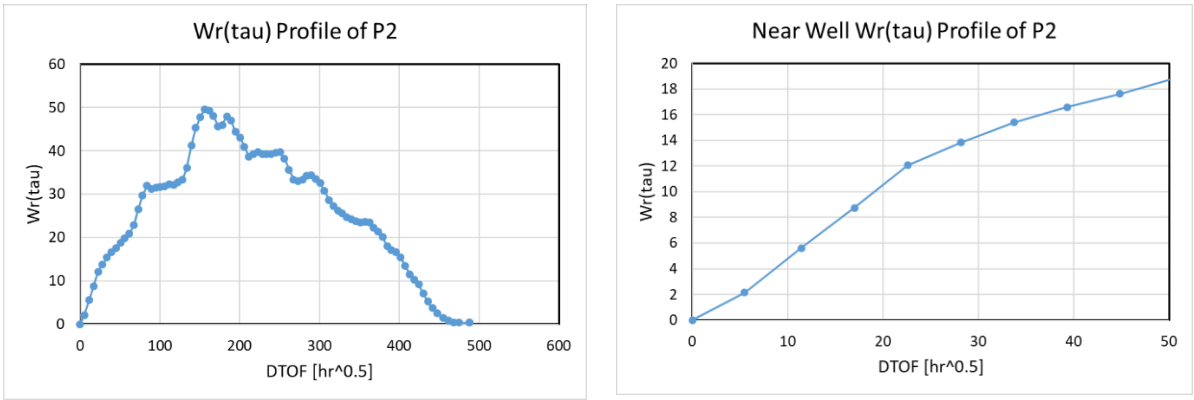

Figure 24 $w_r(\tau)$ Profiles of a Multiple Well 2D Heterogeneous Model (P2)

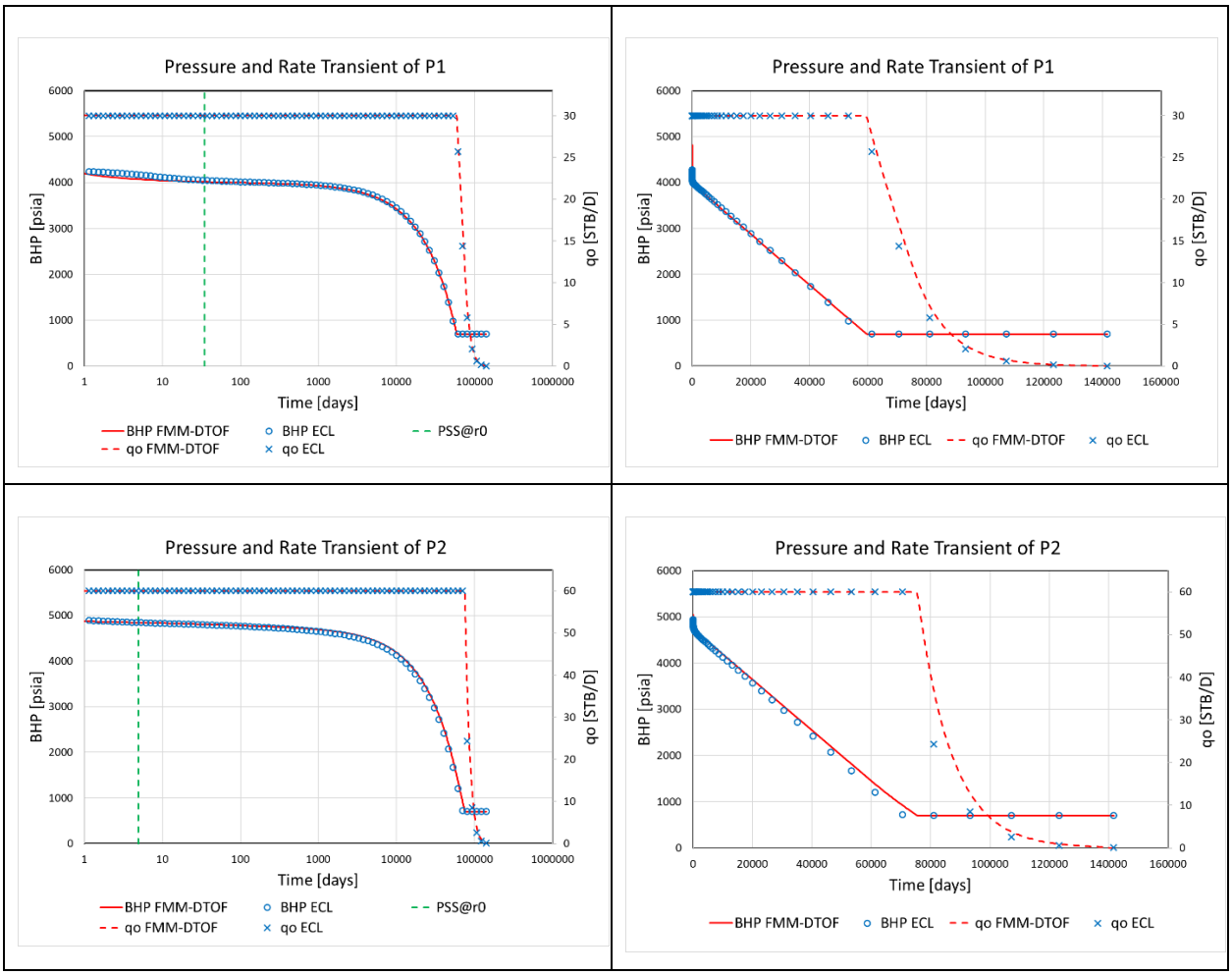

Figure 25 Pressure and Rate Transient for a 2D Heterogeneous Multiple Well Reservoir

Likewise to the case study in Section 2.2, we took the time step logarithmically up to a certain point, and then fixed the step size as a constant after that so that we can make sure the solutions of the system are converged. For both production wells, we can see that FMM-DTOF follows the trend of ECL simulation results even under heterogeneity.

2.4. Multiple Well Field Application 1

- Input Data

As a process of field application study, FMM-DTOF is tested against a 3D reservoir field model described in Figure 26. This field model is provided by one of our industrial partners as a part of a joint research project with the MCERI JIP. This field model is provided from Saudi Aramco as a part of joint research project with MCERI in 2018. The permeability and porosity distribution are described in Figure 27 and Figure 28. Similarly to the sector model used in Section 1.7.3, the permeability distribution can be categorized into two groups. Since V_{DP} is usually applied to a single type permeability distribution, we use 1 [mD] as a cutoff value to calculate V_{DP}. The corresponding value in the model is 0.65, so the level of heterogeneity is "very heterogeneous" according to its definition (Dykstra & Parsons, 1950). The reservoir has five vertical production wells: one at the middle of the reservoir and four around it. The well produces oil at target rate at first, and shift to BHP constraint later. The reservoir and well properties are shown in the tables below (Table 10 and Table 11, respectively). The fluid properties are the same as Table 3.

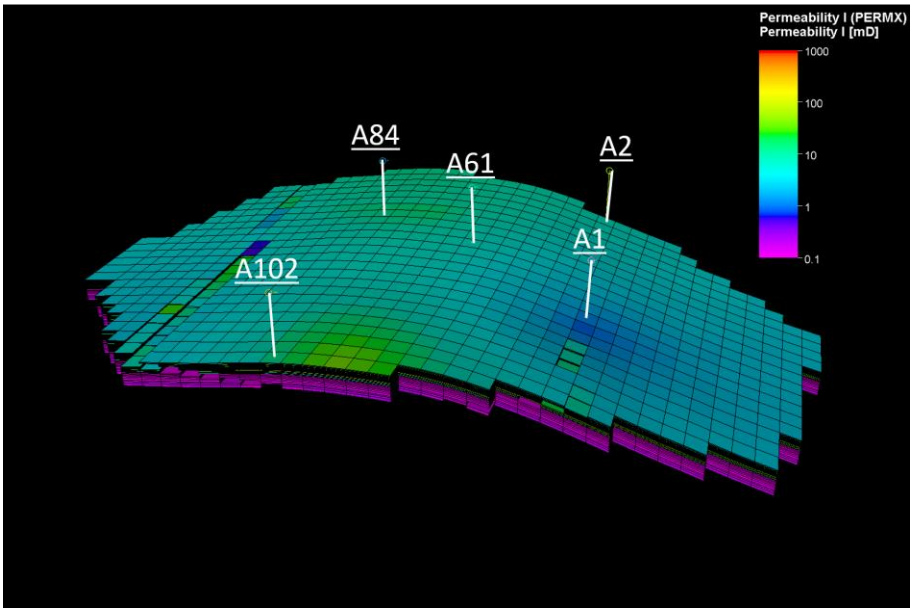

Figure 26 Multiple Well Field Model, Table 10

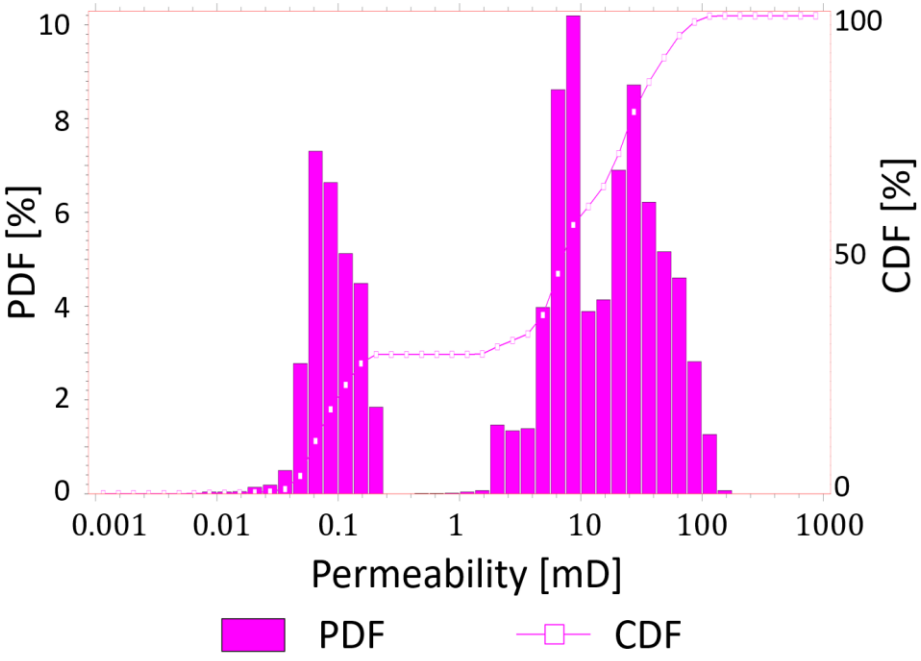

Figure 27 Permeability Histogram, Table 10

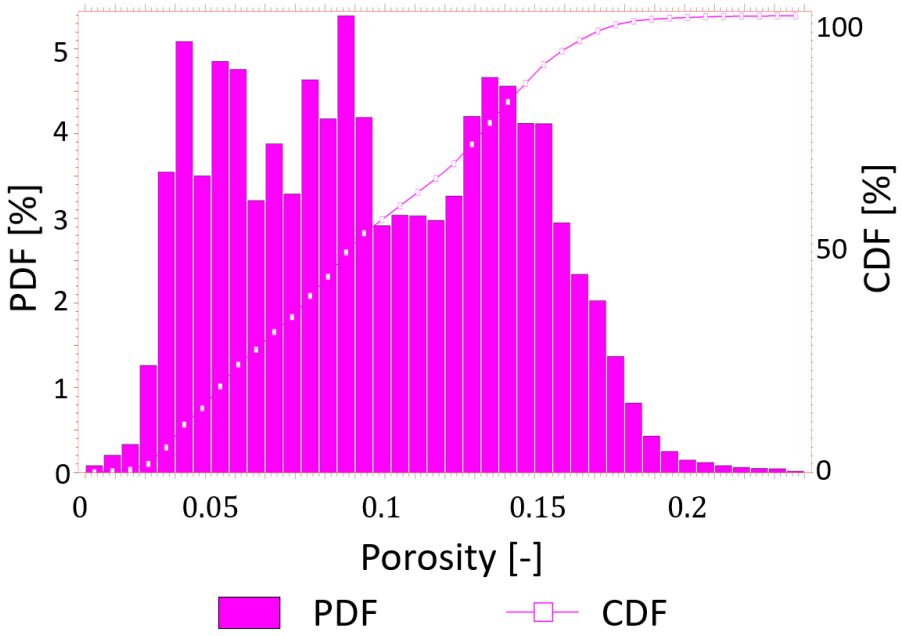

Figure 28 Porosity Histogram, Table 10

Table 10 Reservoir Properties (Field Model 1)

Grid	[38, 25, 32]	[-]
ΔX	250	[ft]
ΔY	250	[ft]
ΔZ	0.5 – 7.0	[ft]
$\bar{\phi}$	0.10	[-]
V_{DP}	0.65	[-]
c_f	1.e-06	[1/psi]
p_{init}	5200	[psia]
$S_{w,init}$	0	[-]

Table 11 Well Properties (Field Model 1)

Well Type	5 Vertical Wells	[-]
Target Rate	500	[STB/D]
BHP Constraint	2000	[psia]

- Results

Figure 29 shows the $w_r(\tau)$ profile along τ for each well (up for overall and down for near well, respectively). Especially in the near well region, A2 and A102 have more moderate gradient compared to A1, A61 and A84, since they are located right next to the reservoir boundary. Next, Figure 30 shows the production forecast based on FMM-DTOF and ECL for each well. The red and blue dots represent FMM-DTOF and ECL, respectively. Throughout the case study, we took the time step size logarithmically up to a certain point, and a constant time step size after that. We made sure that both pressure and rate solutions are converged with respect to time step size for each well.

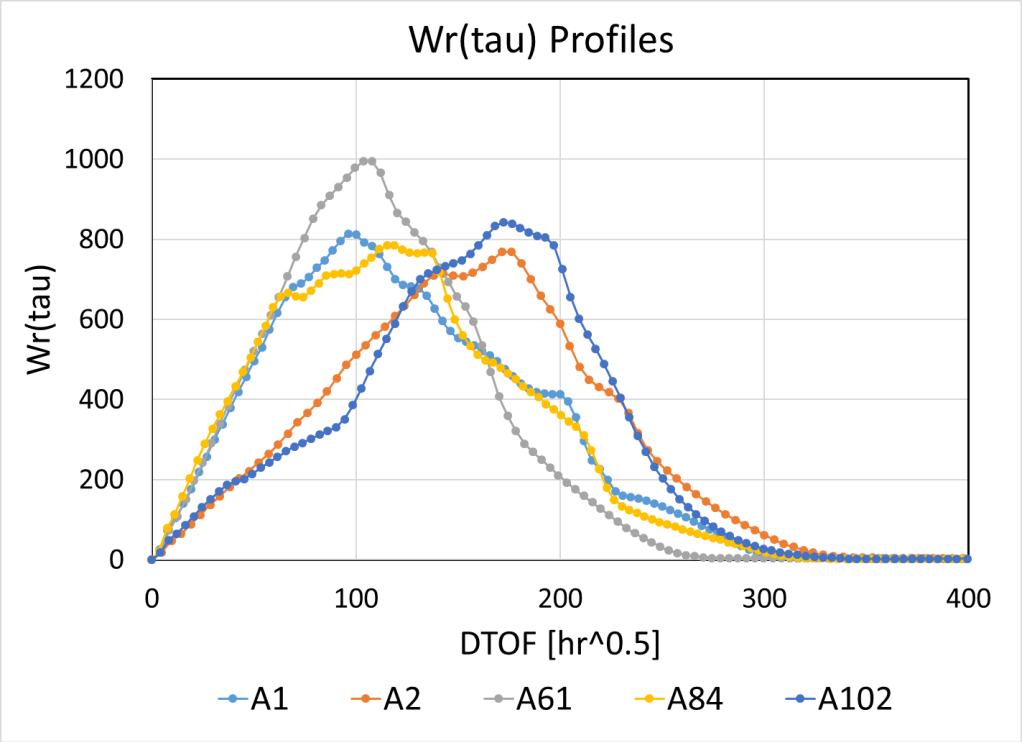

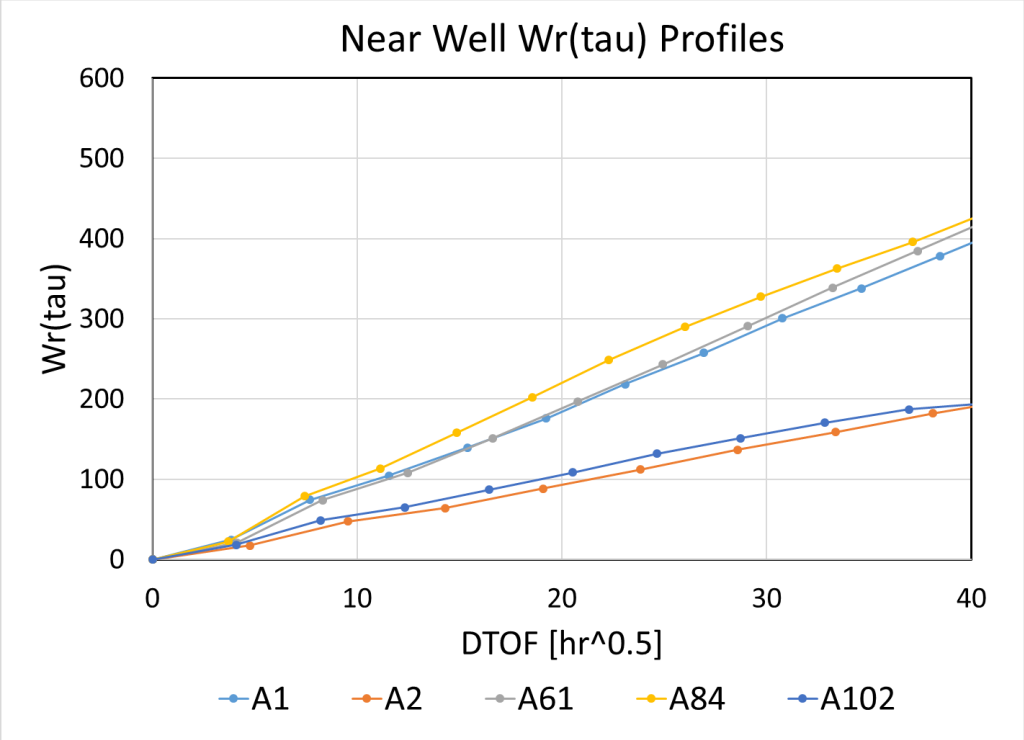

Figure 29 $w_r(\tau)$ Profiles of a Multiple Well Field Model 1

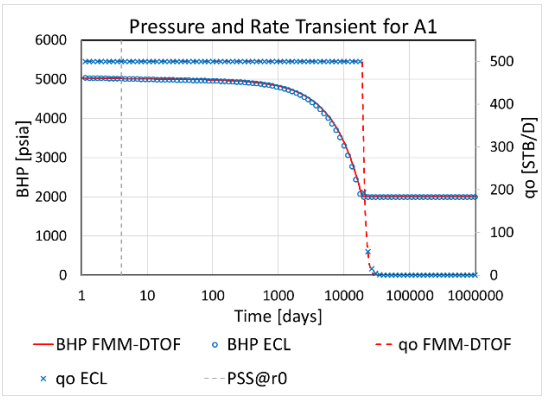
Pressure and Rate Transient for A1
BHP [psia]
qo [STB/D]
Time [days]
BHP FMM-DTOF
BHP ECL
qo FMM-DTOF
qo ECL
PSS@r0

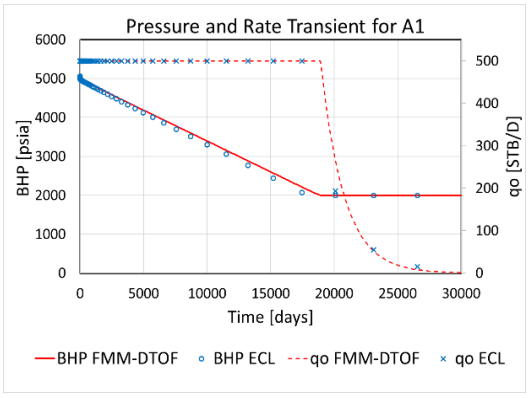
Pressure and Rate Transient for A1
BHP [psia]
qo [STB/D]
Time [days]
BHP FMM-DTOF
BHP ECL
qo FMM-DTOF
qo ECL

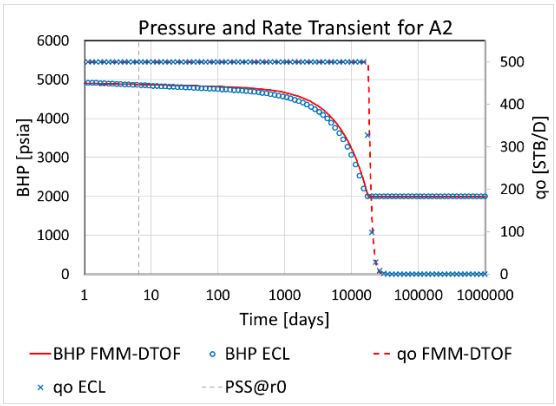
Pressure and Rate Transient for A2
BHP [psia]
qo [STB/D]
Time [days]
BHP FMM-DTOF
BHP ECL
qo FMM-DTOF
qo ECL
PSS@r0

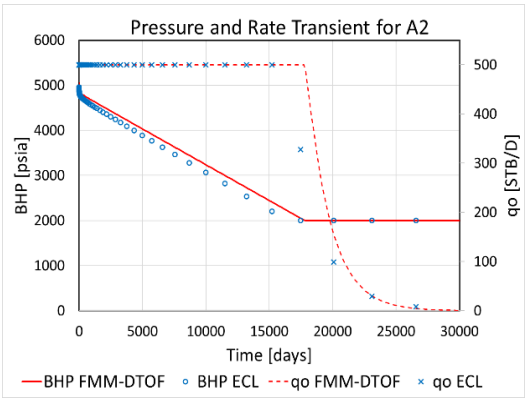
Pressure and Rate Transient for A2
BHP [psia]
qo [STB/D]
Time [days]
BHP FMM-DTOF
BHP ECL
qo FMM-DTOF
qo ECL

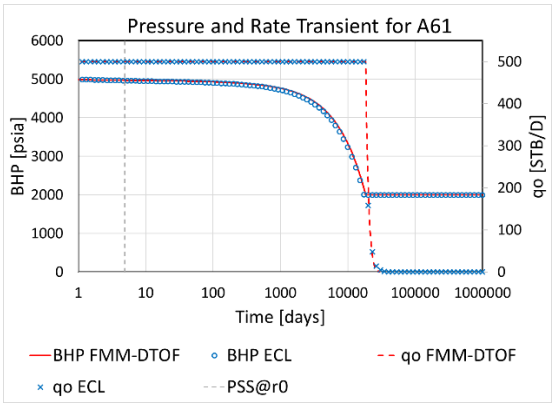
Pressure and Rate Transient for A61
BHP [psia]
qo [STB/D]
Time [days]
BHP FMM-DTOF
BHP ECL
qo FMM-DTOF
qo ECL
PSS@r0

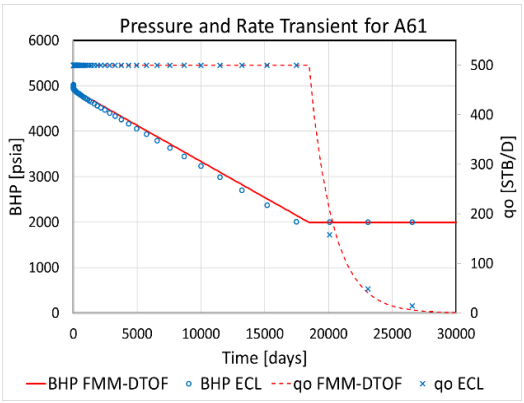
Pressure and Rate Transient for A61
BHP [psia]
qo [STB/D]
Time [days]
BHP FMM-DTOF
BHP ECL
qo FMM-DTOF
qo ECL

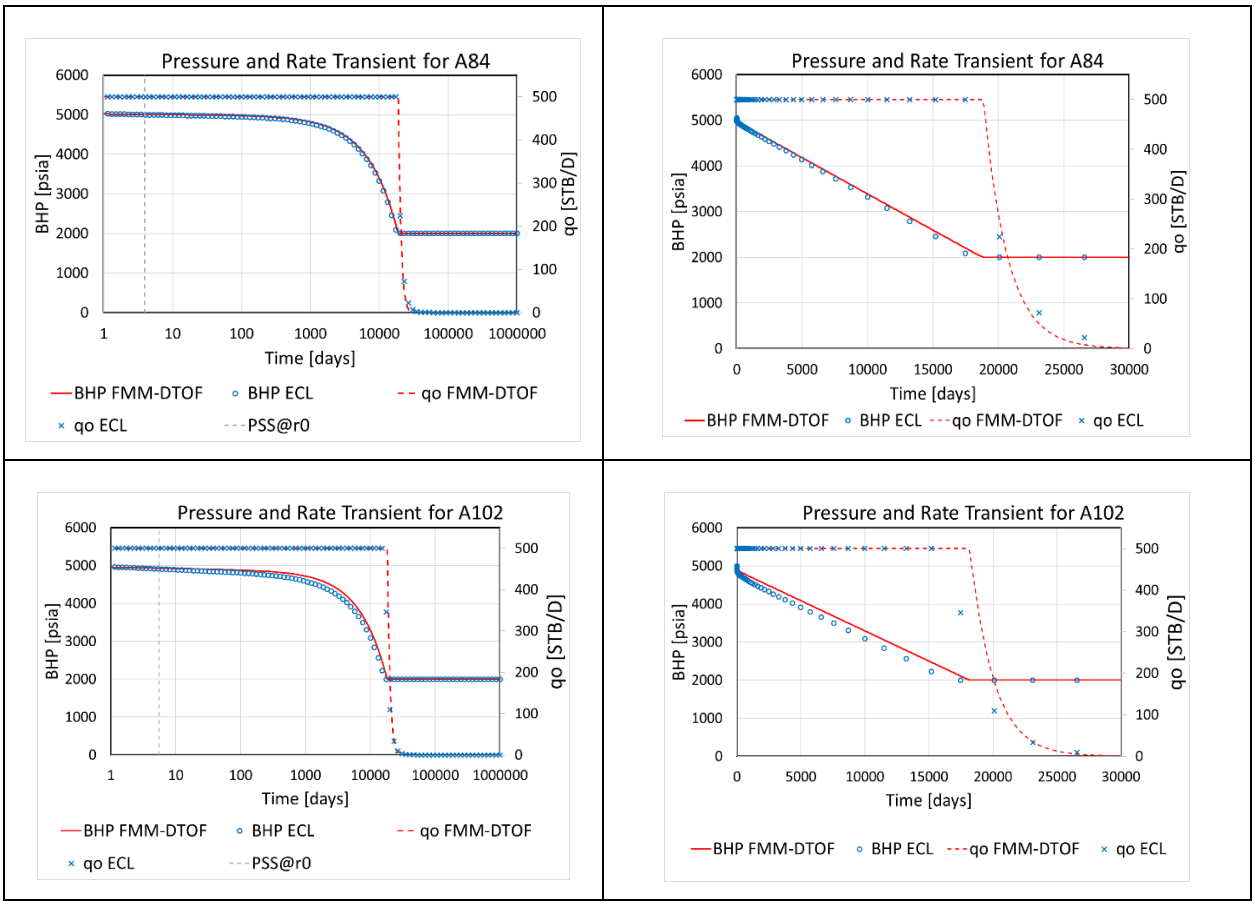

Figure 30 Pressure and Rate Transient for a Multiple Well Field Model 1

By and large, FMM-DTOF based simulation results are following ECL simulation results. However, more careful observation lets you notice that A2 and A102 have bigger mismatch in BHP than A1, A61 and A84. This implies that FMM-DTOF has some error as it goes close to the reservoir boundary. The further analysis is made in the following sections to analyze and identify the causes of the mismatch.

2.5. Multiple Well Field Application 2

- Input Data

As a process of field application study, FMM-DTOF is tested against a 3D reservoir field model described in Figure 31. This field model is provided by one of our industrial partners as a

part of a joint research project with the MCERI JIP. This field model is provided from Saudi Aramco as a part of joint research project with MCERI in 2018. Figure 32 and Figure 33 describe the permeability and porosity distribution, respectively. Since the permeability follows the single model distribution, we can apply V_{DP} as a measurement of heterogeneity. The calculated V_{DP} in the model is 0.765, so it is more heterogeneous than the previous case used in Section 2.4. The model has three vertical production wells and one production well drilled horizontally. The well produces oil at target rate at first, and shift to BHP constraint later. The reservoir, fluid type and well properties are shown in the tables below (Table 12, Table 13 and Table 14 for reservoir, fluid and well properties, respectively).

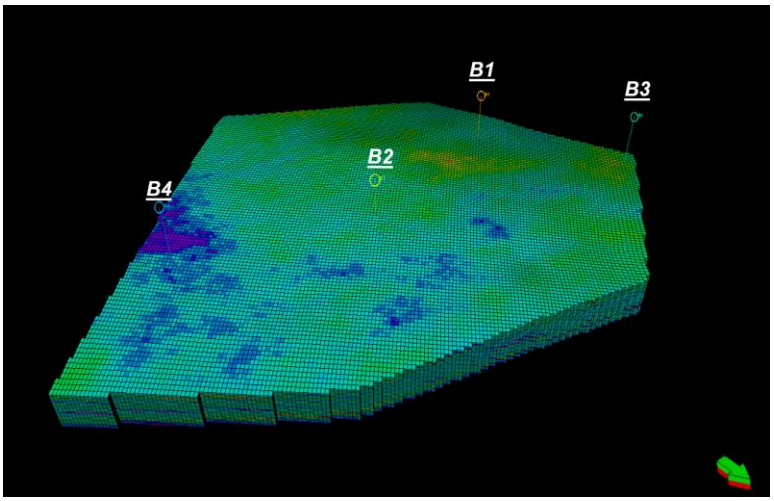

Figure 31 Multiple Well Field Model, Table 12

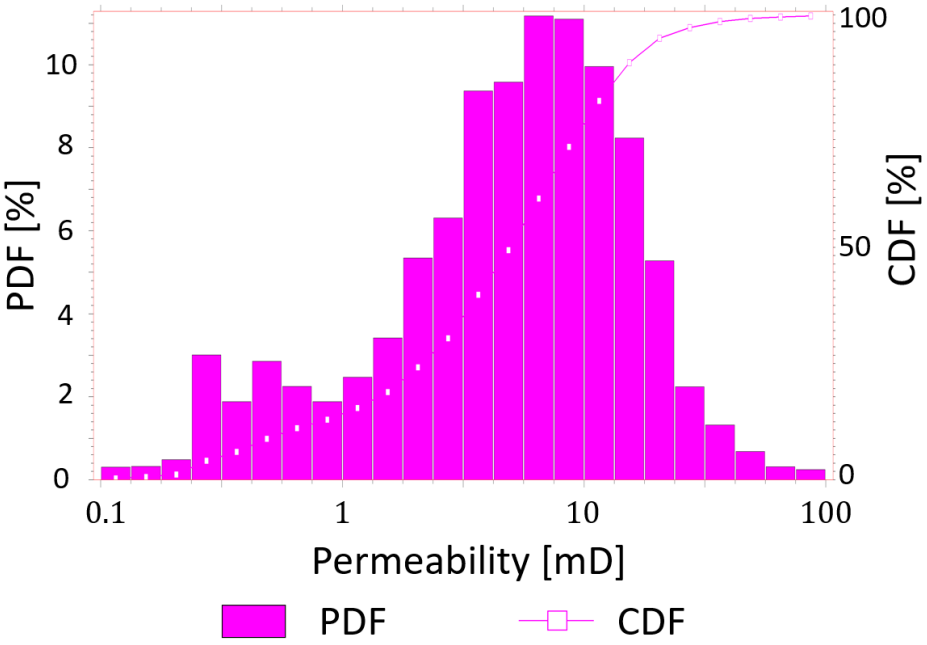

Figure 32 Permeability Histogram, Table 12

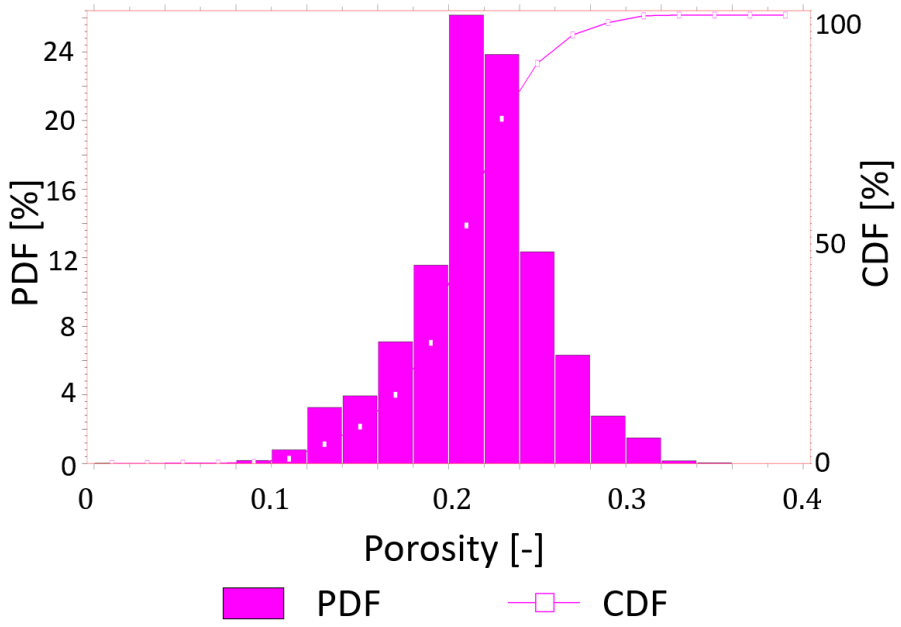

Figure 33 Porosity Histogram, Table 12

Table 12 Reservoir Properties (Field Model 2)

Grid	[122, 155, 26]	[-]
ΔX	58	[m]
ΔY	58	[m]
ΔZ	4.7	[m]
ϕ	0.22	[-]
V_{DP}	0.765	[-]
c_f	5.79e-05	[1/bar]
p_{init}	135	[bars]
$S_{w,init}$	0	[-]

Table 13 Fluid Properties 2

Fluid Type	Dead Oil	[-]
B_o	0.99	[rm3/sm3]
μ	5	[cp]
c_o	1.25e-6	[1/bar]

Table 14 Well Properties (Field Model 2)

B1		
Well Type	Vertical	[-]
Position	Edge	[-]
Target Rate	100	[sm3/day]
BHP Constraint	48	[barsa]
B2		
Well Type	Vertical	[-]
Position	Center	[-]
Target Rate	100	[sm3/day]
BHP Constraint	48	[barsa]
B3		
Well Type	Vertical	[-]
Position	Edge	[-]
Target Rate	100	[sm3/day]
BHP Constraint	48	[barsa]
B4		
Well Type	Horizontal	[-]
Position	Edge	[-]
Target Rate	100	[sm3/day]
BHP Constraint	48	[barsa]

- Results

Figure 34 shows the $w_r(\tau)$ profile along τ for each. Figure 35 shows the production forecast based on FMM-DTOF and ECL. The red and blue dots represent FMM-DTOF and ECL, respectively.

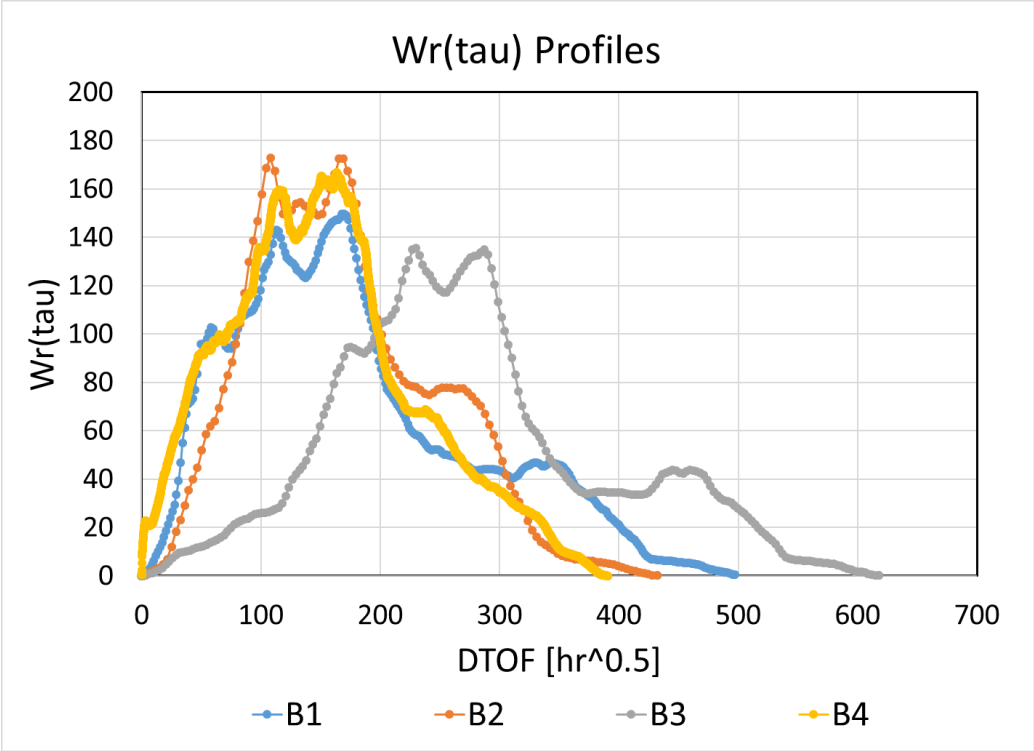

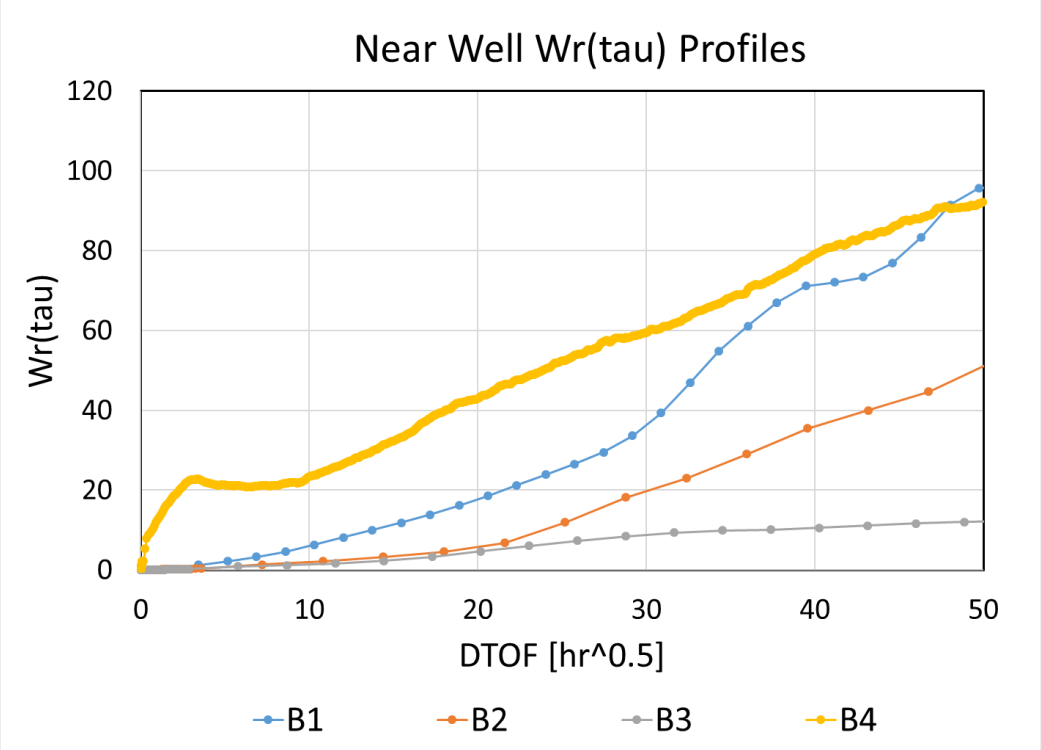

Figure 34 $w_r(\tau)$ Profiles of a Multiple Well Field Model 2

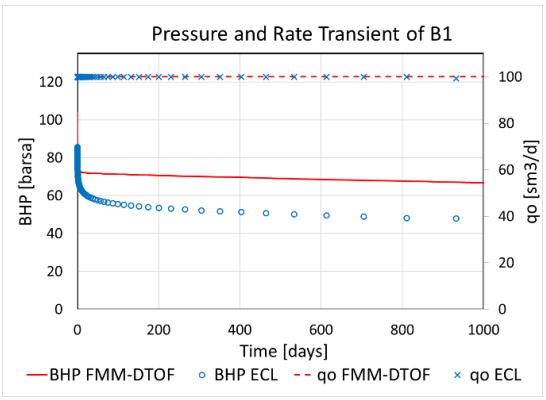

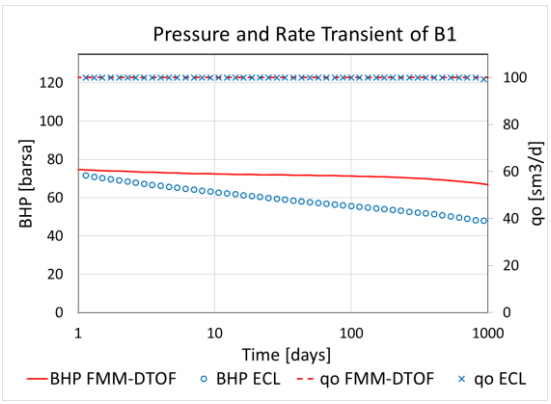

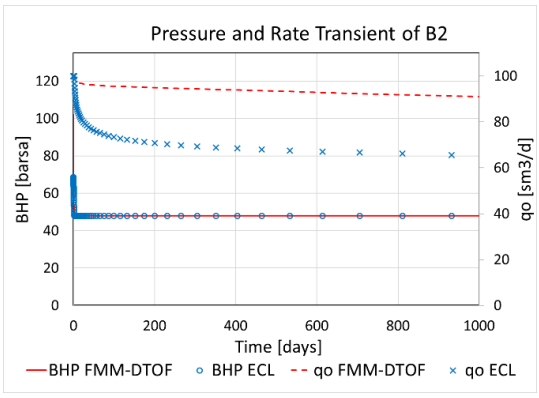

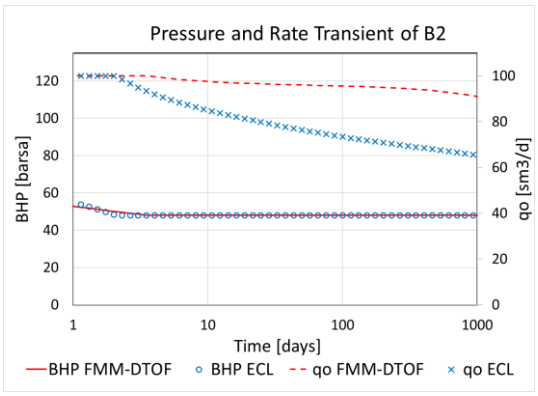

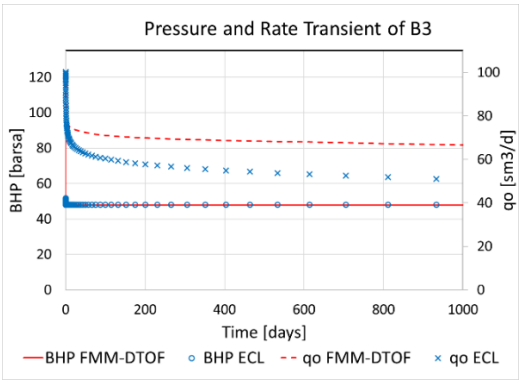

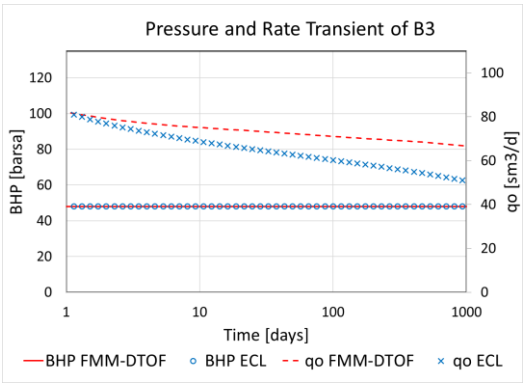

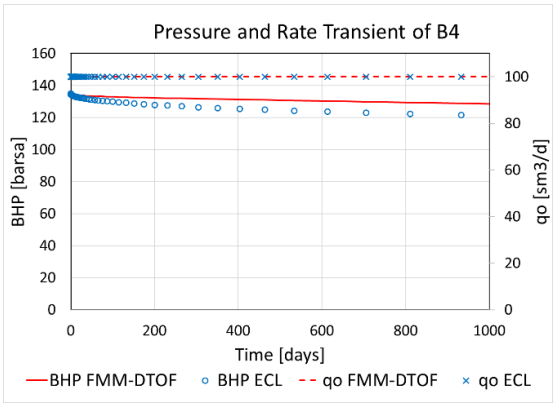

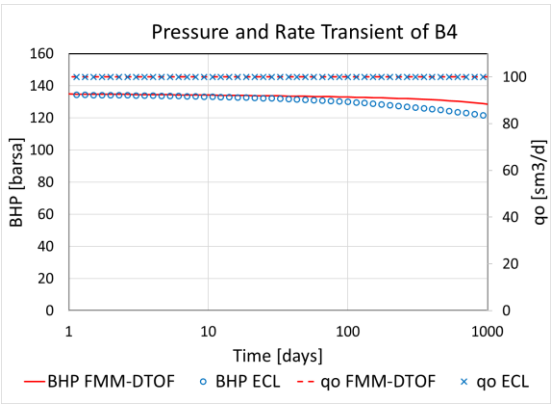

Figure 35 Pressure and Rate Transient for a Multiple Well Field Model 2

From Figure 34, it can be observed that B4 has a sharp jump at near well region. This is due to the wider surface area of pressure front because it is horizontally drilled. Next, B2 has the second smallest τ when the pressure front reaches the last edge of the reservoir boundary, since it is placed at the middle of the reservoir. Lastly, both B1 and B3 are located at near the reservoir boundary, but $w_r(\tau)$ profile of B3 is flatter compared to B1. This indicates that it takes more time for the pressure front to propagate through the reservoir from B3.

As for the pressure and rate transient, FMM-DTOF based simulation results do not match ECL simulation results well. In more detail, the pressure and rate profiles at 1 day are still close to those of ECL, but major discrepancy starts to appear in the mid-late time of the production time. This trend is true for all the four wells. These results imply that the constructed 1D DTOF coordinate may not be a good representation of the actual pressure drop for the mid-late time. The further analysis is made in the following sections to investigate the causes of the mismatch.

2.6. Discussion

In this second chapter, we developed the asymptotic pressure approximation method for multiple well reservoir development using superposition based on FMM-DTOF. At the end of the chapter, we summarize the observations obtained from the study. The major analysis is listed as follows:

- The asymptotic approach takes into consideration the reservoir characteristics into *J* function, and this *J* function is a transient *J* function extended from PSS to transient domain. The concept of the transient *J* function can be easily extended for a multiple well reservoir development by means of superposition
- The use of superposition and the asymptotic approach does not require to solve any explicit reservoir flow equation, since they are taken care of by the analytic pressure approximation,

which leaves only well rate and pressure as unknowns to be solved (30,400 unknows reduced to 11 unknows in Section 2.4)

- Predicted BHP profile has gap if the well is near the reservoir boundary
- In a highly heterogeneous field model, the discrepancy of pressure/rate starts to appear in the mid-late time, which implies the 1D DTOF coordinate may not be a good representation of the reservoir pressure drop even before boundary effects are significant

Throughout the study, we understand that FMM-DTOF works for some models with moderate heterogeneity, based on the assumption that the reservoir pressure drop should be well-aligned with the DTOF. The discrepancy in Section 2.4 and 2.5 implies this correlation may start to break down depending upon degree of heterogeneity or well locations. In the next chapter, we start the research by clarifying the cause of the mismatch we have seen and suggest a new approach which overcomes these problems.

3. FAST SIMULATION BASED ON THE PSS PRESSURE AS A SPATIAL COORDINATE

3.1. Objective of Chapter

For the further investigation of the mismatch in the field application, we pick one production well (B2), which is fully completed and located at the center of the reservoir. Besides, for the purpose of comparison, here we show a numerical simulation result based on FMM (FMM-SIM) against ECL finite difference simulation to remove the impact of the asymptotic pressure approximation. $w_r(\tau)$ profile for B2 is the same as the second row in Figure 34. The figure below shows the production forecast based on FMM-SIM/DTOF and ECL in absence of other production wells except for B2.

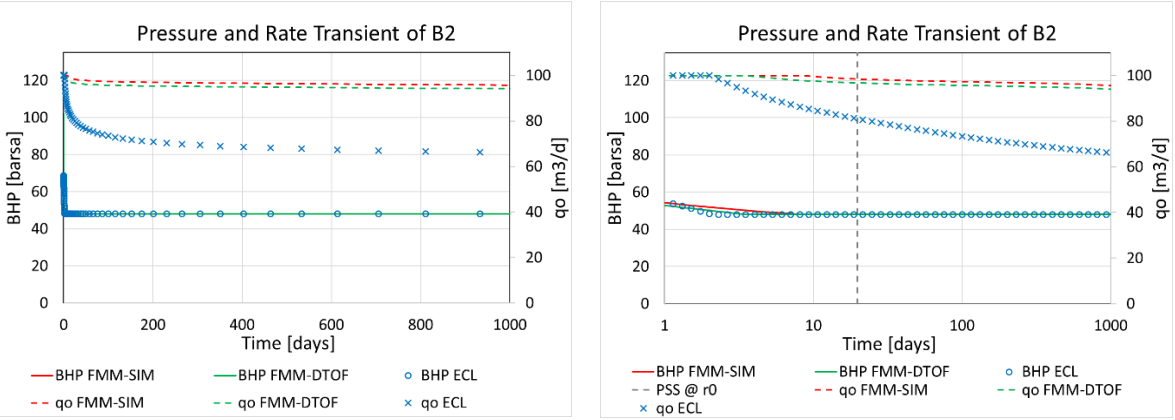

Figure 36 Pressure and Rate Transient for B2

Since the FMM-SIM is still in disagreement with ECL, we can confirm that the cause of the mismatch is not due to the superposition or asymptotic effect. We will show in an additional example below (Section 3.7.3) that the strong deviation of FMM-SIM from ECL is not due to the

onset of the pressure constraint. In this chapter, we introduce the goal of the current study to analyze the cause of the mismatch and to suggest a possible solution.

3.2. Diffusivity Equation

As shown in the previous sections, the strength of the current approach is in its coordinate transformation from 3D to 1D based on the DTOF. This approach is based on the assumption that pressure drop at each cell in the 3D coordinate has a strong correlation with the DTOF obtained from the same well. However, this assumption may or may not hold depending upon the flow regime: early time, mid time or late time, and the degree of reservoir heterogeneity. Hence, it is of importance to test whether a model is appropriately described by the DTOF. As an alternative for the DTOF-based coordinate, we propose a new 1D coordinate θ, which is the normalized PSS pressure difference from the wellbore. The coordinate θ can be derived by solving Eq. (1.1) and Eq. (1.2) for pressure with a uniform value for $\left(\frac{\partial p}{\partial t}\right)$.

$$\theta(\vec{x}) \equiv \left\{ p(\vec{x},t) - p_{wf}(t) \right\}^{PSS} \Big/ q_t \tag{3.1}$$

$$q_t = \int_{\text{Res}} \phi(\vec{x}) c_t(\vec{x},0) d^3x \tag{3.2}$$

The integral showing up in q_t is over the volume of the reservoir connected to the well. In the same manner as FMM-SIM, the fluid properties are evaluated at the initial condition.

$$c_t(\vec{x},t) \to c_t(\vec{x},0), \quad \lambda_{rt}(\vec{x},t) \to \lambda_{rt}(\vec{x},0) \tag{3.3}$$

$$p(\vec{x},t) \to p^{PSS}(\vec{x},t) = p_{wf}(t) + q_t \cdot \theta(\vec{x}) \tag{3.4}$$

Taking into consideration these assumptions in addition to the uniform $\left(\frac{\partial p}{\partial t}\right)$, the diffusivity equation Eq. (1.1) can be transformed to Eq. (3.5) .

$$\nabla \bullet \left(-\lambda_{rt}\left(\vec{x},0\right)\vec{\vec{k}}\left(\vec{x}\right)\bullet \nabla p\left(\vec{x}\right)\right) = \phi\left(\vec{x}\right)c_t\left(\vec{x},0\right) \tag{3.5}$$

Here, the coordinate is proportional to the pressure difference and the normalization of the pressure is arbitrary, since it is needed only for the PSS coordinate. Since Eq. (3.5) is a second order ordinary differential equation, we need two BC's shown as Eq. (3.6) and Eq. (3.7) to solve the system. Solving the system defined here gives us the new coordinate θ.

$$p = 0 \quad @\, r = r_w \tag{3.6}$$

$$\vec{n} \bullet \vec{\vec{k}} \bullet \nabla p = 0 \quad @\, boundary \tag{3.7}$$

Under the PSS coordinate θ, the diffusivity equation can be expressed as Eq. (3.8).

$$c_t\left(\theta,t\right)\frac{\partial p\left(\theta,t\right)}{\partial t} - \frac{\partial q\left(\theta,t\right)}{\partial V_p\left(\theta\right)} = 0 \tag{3.8}$$

It is important that this is the simplest pressure transient equation and also the direct analog of the diffusivity equation in DTOF coordinate. Thus, this can be easily generalized to multiple phase and multiple component flow as previously done using FMM-SIM (Iino & Datta-Gupta, 2018; Iino et al., 2017). In the next section, we derive a discrete form of the coordinate θ.

3.3. Derivation of PSS Coordinate

In this section, we start from Eq. (3.5). Taking the volume integral of Eq. (3.5) gives Eq. (3.9) for a cell volume Ω_n, which is the sum of the outwardly directed normalized fluxes.

$$\iiint_{Volume,\Omega_n} d^3x \nabla \bullet \left(-\lambda_{rt}\left(\vec{x},0\right)\vec{\vec{k}}\left(\vec{x},0\right)\bullet \nabla p\left(\vec{x}\right)\right) = \sum_{m=w,\, faces} q_{nm} \tag{3.9}$$

The RHS of Eq. (3.9) can be expressed separately for each boundary condition.

$$\sum_{m=w,\, faces} q_{nm} = \sum_{m=w,\, faces}^{q:Known} q_{nm} + \sum_{m=w,\, faces}^{p:Known} q_{nm} + \sum_{m=w,\, faces}^{q,p:Unknown} q_{nm} \tag{3.10}$$

The first term in the RHS corresponds to the no flow boundary condition on the outer boundary. The second term corresponds to the boundary condition of wellbore. The last term represents the

flux between adjacent cells. In order to expand Eq. (3.10), we introduce the half cell transmissibility and intercell transmissibility. The half cell transmissibility and intercell transmissibility between corner point cells "*n*" and "*m*" are defined as Eq. (3.11) and Eq. (3.12) (Ponting, 1989).

$$T_f^{Half} = k_f \cdot \left(\frac{\vec{n}_f \bullet \vec{t}_f}{t_f^2} \right) \tag{3.11}$$

$$\frac{1}{T_{nm}} = \frac{1}{T_{n,f+}^{Half}} + \frac{1}{T_{m,f-}^{Half}} \tag{3.12}$$

Here, $\vec{n}$ and $\vec{t}$ are the normal and tangent vectors of a cell. Using these definitions, Eq. (3.10) can be written as Eq. (3.13).

$$\sum_{m=w,\,faces} q_{nm} = \lambda_{rt,n} WI_n \cdot p_n + \sum_{m(n)}^{q,p:Unknown} \lambda_{rt,nm} \cdot T_{nm} \cdot \left(p_n - p_m \right) \tag{3.13}$$

Here, *WI* represent the Well Index. λ_{rt} is evaluated based on the initial saturation of the upstream cell. The first term is non-zero only for well cells. Substituting this back to Eq. (3.5) gives Eq. (3.14).

$$\begin{gathered} \left\{ \lambda_{rt,n} \cdot WI_n + \sum_{m(n)}^{\text{internal}} \lambda_{rt,nm} \cdot T_{nm} \right\} \cdot p_n - \sum_{m(n)}^{\text{internal}} \lambda_{rt,nm} \cdot T_{nm} \cdot p_m = c_{t,n} \cdot V_{p,n} \\ q_t = \sum_n \lambda_{rt,n} \cdot WI_n \cdot p_n = \sum_n c_{t,n} \cdot V_{p,n} \end{gathered} \tag{3.14}$$

This system is solved using Python library (Virtanen et al., 2020).

Here, we have calculated the PSS coordinate θ numerically, so we would like to test it against the geometry of the radial solution. We have θ at the center of each fine cell and the corresponding cumulative V_p for the finite difference calculation. On the other hand, we know the distance to the cell center, which gives the analytic radial pore volume, expressed as $\pi r^2 h\phi$ for the analytical plot, where h denotes the thickness of the reservoir. These two plots are

similar in that both are solving for the same pressure difference using the same 2D homogeneous model, but different in their way of calculation. Although the radial solution is a continuous function of r (correspondingly θ), the cumulative V_p based on the numerical solution takes a form of a step function. This effect is especially significant near the well.

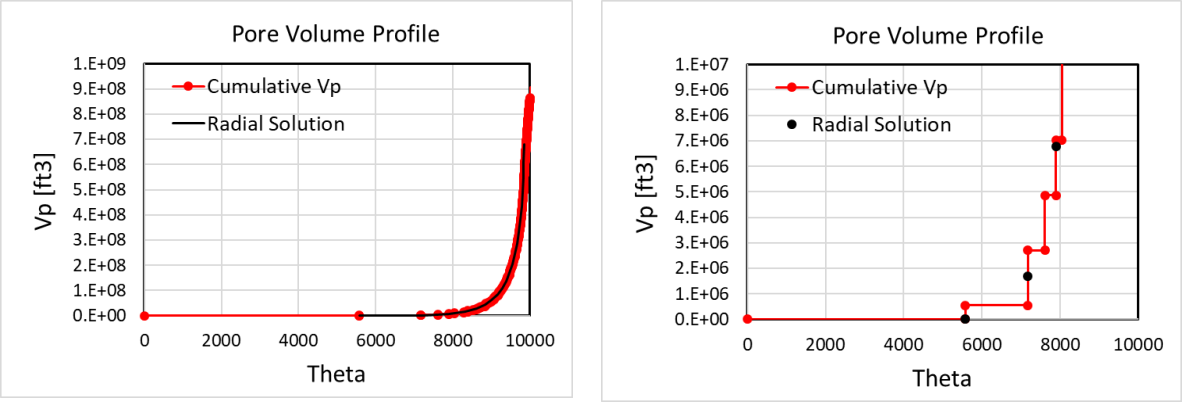

Figure 37 Drainage Pore Volume Profile

The red points denote the 1D cumulative V_p, and it is compared against the radial solution in a homogeneous model (shown as black plots) up to the end of radial flow. Among these red points, the smallest positive V_p corresponds to the pore volume of the well block. The next point corresponds to the cumulative V_p up to the neighboring cells of the well block. From the figure, it can be confirmed that the cumulative V_p matches the radial solution in a homogeneous model up until the boundary effect appears.

3.4. PSS Coordinate vs DTOF Coordinate

For fixed rate drawdown, the late time solution will reach PSS, and the pressure drop in a reservoir model will always be correlated with θ, with no scatter. For fixed BHP production,

$\left(\frac{\partial p}{\partial t}\right)$ is not uniform in the reservoir and PSS is never reached, but the solution will reach boundary dominated flow (BDF) at late time. In this section, we compare the two different coordinates (τ and θ) and see their similarities and differences. The following figures show the coordinate contour maps with different heterogeneity: Figure 38 for a homogeneous case and Figure 40 for $V_{DP} = 0.6$. The permeability map for the $V_{DP} = 0.6$ model is shown as Figure 39.

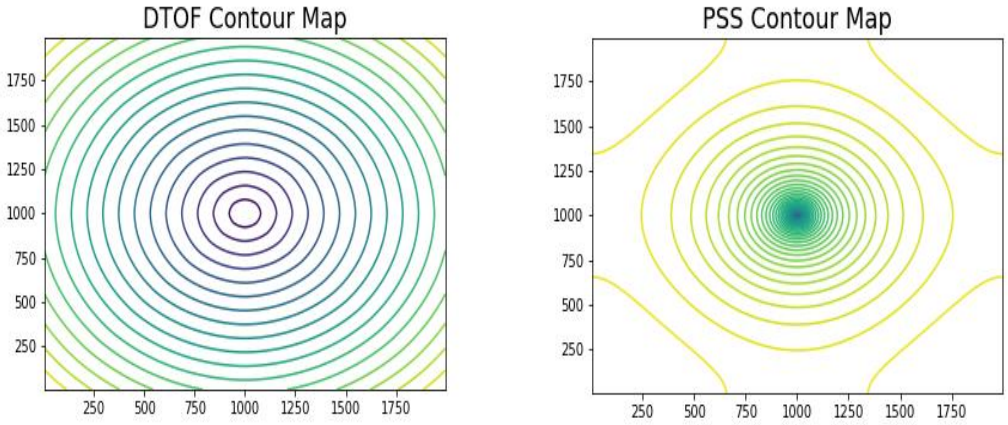

Figure 38 Contour Maps with V_{DP} = 0: DTOF τ (left) and PSS θ (right)

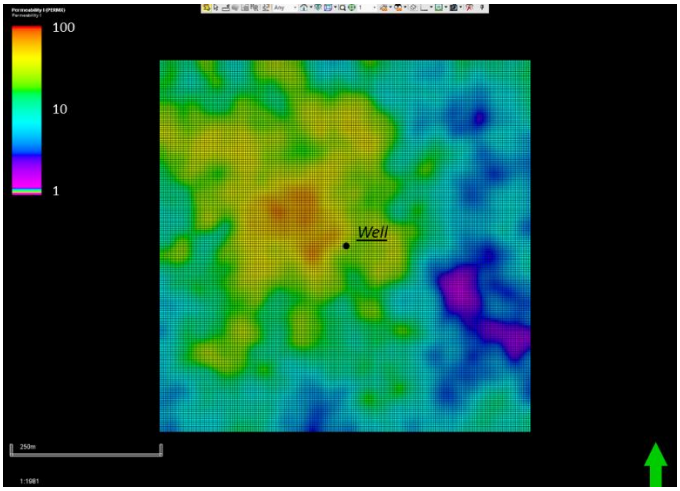

Figure 39 Permeability Map for V_{DP} = 0.6

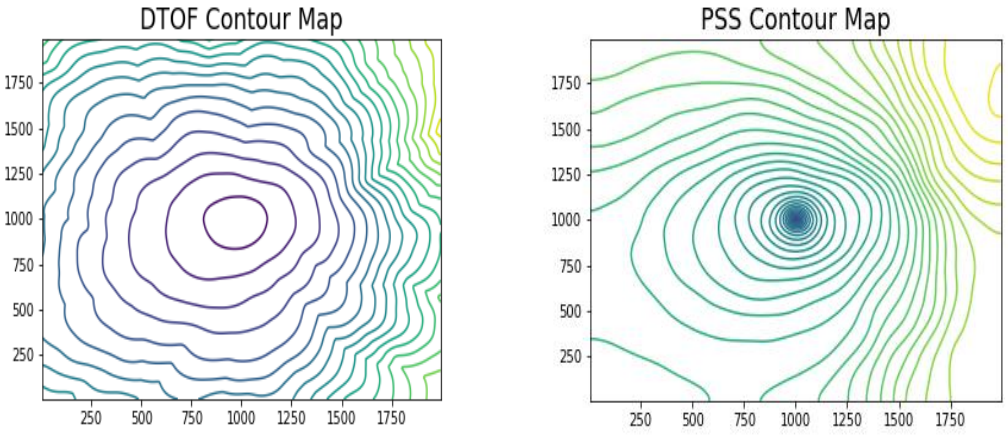

Figure 40 Contour Maps with V_{DP} = 0.6: DTOF (left) and PSS (right)

In comparison of these two coordinates, we can see that the DTOF and PSS coordinates are aligned near well but diverge where boundary effects start to appear. Since it is a solution to the Eikonal equation, the DTOF is a good coordinate for early time and away from strong heterogeneities, including no flow boundaries. In contrast, near the boundary, the DTOF coordinate is not well-aligned with the pressure drop contour. This indicates the underlying assumption of FMM-SIM and FMM-DTOF that pressure drop is aligned with DTOF and that the

pressure variation along each τ contour surface can be ignored, does not hold for late time and boundary dominated flow. The comparison of Figure 38 and Figure 40 indicates that the location at which the boundary effect appears depends upon the reservoir heterogeneity.

Furthermore, the shape of the pressure drop contour is also affected by the inner boundaries. (Lee et al., 2003) in their book described the flow geometry in the case of a vertical infinite conductivity fracture as shown in the LHS of Figure 41. At PSS, the pressure contour around the vertical fracture has an ellipsoidal shape due to the superposition of the drawdown from multiple locations on the fracture (Kucuk & Brigham, 1979). On the other hand, the DTOF contour calculated from the Eikonal equation is shown in the RHS of Figure 41. This coordinate describes the shape of the limit of detectability around the fracture and does not take into consideration the superposition due to the inner boundary. Similar effects will be also true for multiple perforation wells (Malone et al., 2019). Consequently, there may be a discrepancy between the 1D DTOF coordinate and the actual pressure contour, even if the well is located far from the external reservoir boundary.

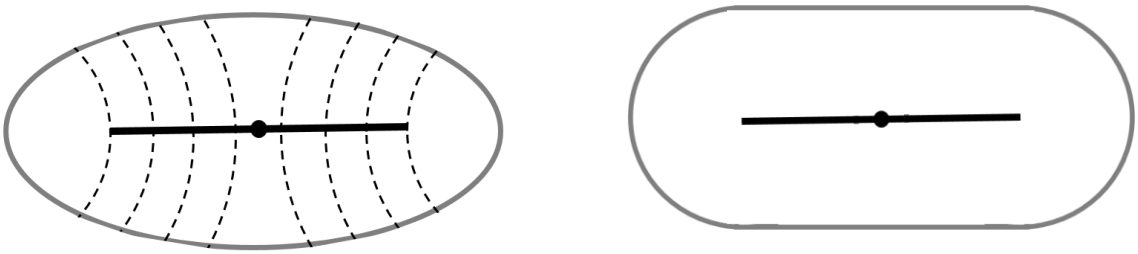

Figure 41 Flow Geometry around a Vertical Fracture

In the next chapter, we analyze the 1D coordinates (PSS and DTOF) against the reservoir pressure drop.

3.5. PSS vs DTOF Correlations

In order to double-check the validity of the DTOF coordinate, we make quantitative comparisons of the pressure drop at each time step with respect to θ and τ. Figure 42 shows the pressure profiles of a heterogeneous model ($V_{DP} = 0.6$) at a low production rate (10 STB/D), so the well does not reach the BHP constraint (1500 psia) by the end of the simulation (400 days). The PSS coordinate is calculated through the process in Section 3.3. The mean variance shown at the top right of each figure is calculated based on a variance of 400 bins with the same number of data points in each bin. In the following two figures, the first, second and third rows correspond to 1, 10 and 100 day pressure profiles, respectively.

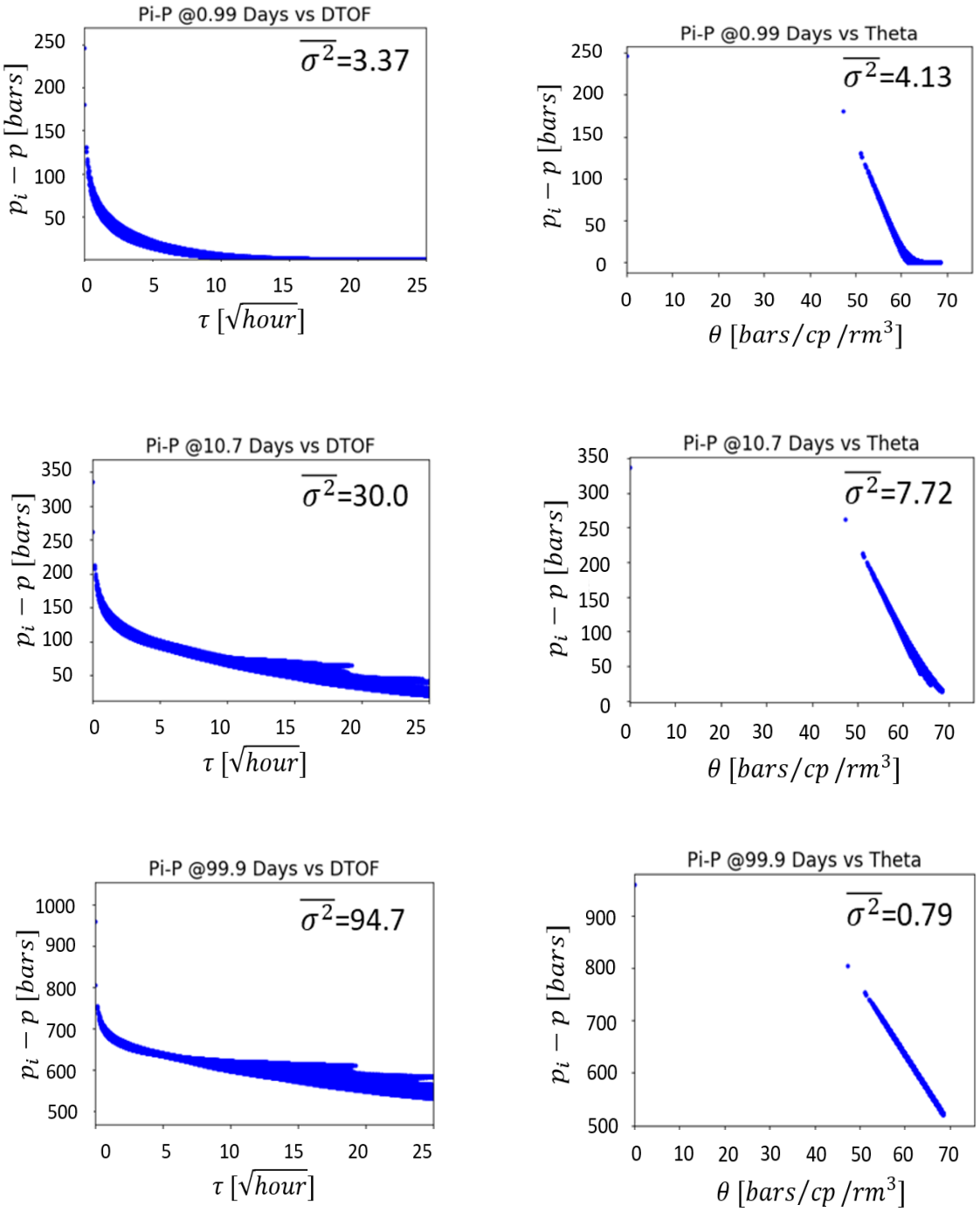

Figure 42 Pressure Profiles with Low Production Rate (PSS Flow)

From Figure 42, we can see the trend that the distribution of pressure drop along DTOF is scattered compared to PSS coordinate shown in the second column, which implies the pressure

drop is not always aligned with DTOF. In more detail, at early time, the mean variance based on either is very small, which indicates that both are good coordinates for transient analysis at early time. However, as the production time goes on, the mean variance based on the DTOF coordinate keeps increasing, while this is not the case for the PSS coordinate. This result implies that the DTOF coordinate is no longer a good coordinate for mid/late time pressure transient flow.

Next, Figure 43 shows the pressure profiles of the model with a high production rate (100 STB/D). As a larger volume of fluid is produced compared to the previous calculation, the well control shifts from a fixed rate drawdown to fixed BHP control (1500 psia), here after 12.3 days.

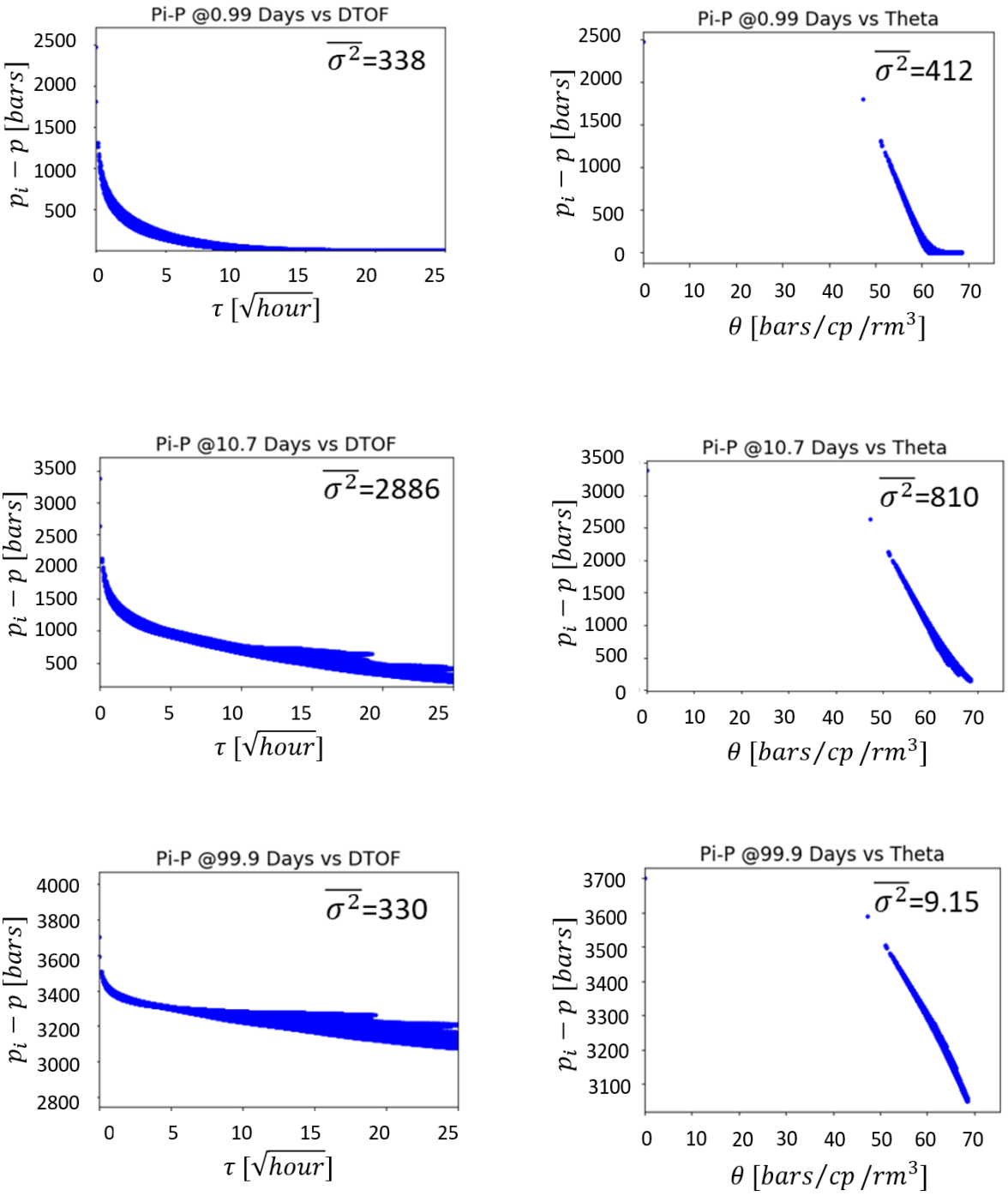

Figure 43 Pressure Profiles with High Production Rate (BDF Flow)

For the DTOF coordinate, generally the same trend can be observed as in the previous calculation. However, it is noteworthy that the mean variance of the PSS coordinate is still very

small at the late time even when PSS flow is not reached. From this comparison, it suggests that θ can be as good or a better 1D coordinate than DTOF for transient analysis at all flow regimes.

3.6. PSS Discretization

In this section, we develop the computational grid for the PSS-based simulation. The discretization is constructed using dilation/erosion operations on the three dimensional finite difference grid, following the PSS coordinate. Pore volume and transport properties (intercell transmissibility and the well index) are obtained by a suitable local upscaling calculation. We also show how to increase the early time resolution with a novel LGR construction in the equivalent well cell. The calculations are tested (with and without LGR) for the 2D synthetic homogeneous model. The reservoir, fluid and well properties used in the study is shown in Table 15, Table 16 and Table 17.

Table 15 Reservoir Properties (2D Homogeneous, 2)

Grid	[41, 41, 1]	[-]
ΔX	600	[ft]
ΔY	600	[ft]
ΔZ	150	[ft]
ϕ	0.01	[-]
k	1	[mD]
c_f	1.0e-6	[1/psi]
p_{init}	5200	[psia]
$S_{w,init}$	0	[-]

Table 16 Fluid Properties 3

Fluid Type	Dead Oil	[-]
B_o	0.99	[bbl/STB]
μ	1.0	[cp]
c_o	1.925e-7	[1/psi]

Table 17 Well Properties for PSS-SIM (2D Homogeneous, 2)

Well Type	Vertical	[-]
Location	[21, 21, 1]	[-]
Target Rate	300	[STB/D]
BHP Constraint	700	[psia]

The corresponding pressure transient profile is shown in Figure 44.

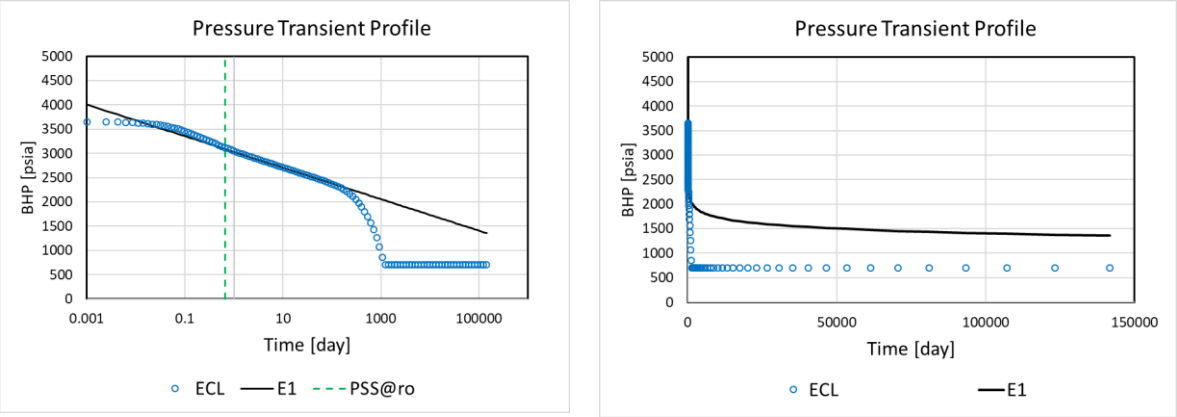

Figure 44 Pressure Transient Profile of a 2D Homogeneous Model for PSS-SIM based on Commercial Software and E1 Analytical Solution

The black line and blue circles represent the E1 analytical solution and the numerical solution based on ECL, respectively. The green dash vertical line denotes the beginning of PSS at the Peaceman radius.

3.6.1. PSS Grid Design

3.6.1.1. Discretization Methodology

In the process of discretization, we use dilation and erosion, which is a method commonly used in the field of image processing (Dougherty & Lotufo, 2003). The discretization will be first performed as a coarsening of the 3D finite difference grid. The first interval will consist of all the perforated well cells. We will also examine local grid refinement (LGR) to improve resolution beyond the Eclipse solution at early time. The discretization process is as follows:

1. First, we label well blocks as “accepted”.
2. Second, we take a number of steps for the dilation process among the neighbors of the accepted cells. The figure below describes the accepted cell (red) and its neighbors included in the dilation region (green) with a step size of 4.

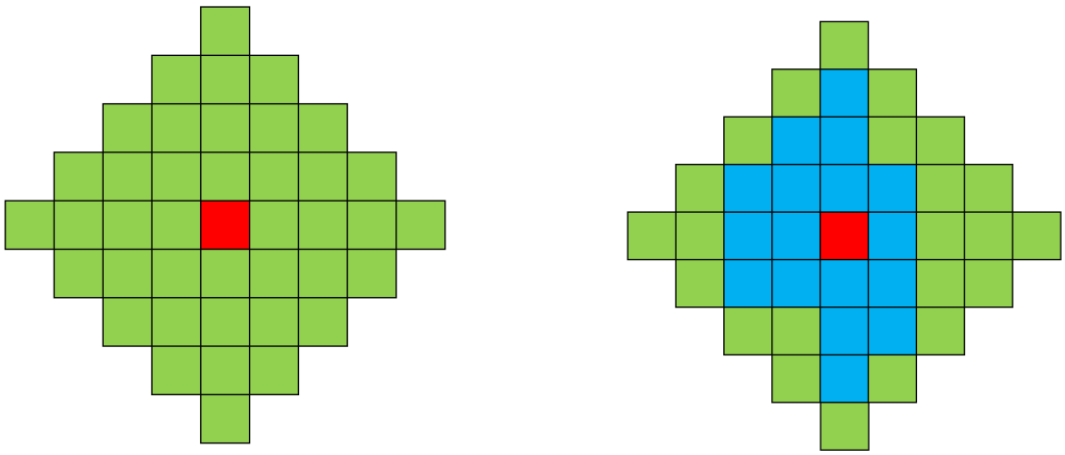

Figure 45 Dilation (left) / Erosion (right) of Cells with Step = 4

3. Among the dilated region (green), we take the pore volume weighted average of θ, to obtain the threshold for the erosion step.

4. We perform erosion based on the threshold value of θ and label these cells as “accepted”. This procedure gives a smoothly designed grid by discarding the periphery cells which have a larger value of θ than the threshold value.
5. Repeat the process 2 through 4 until all cells are accepted.

Process 1-5 gives the design of the PSS grid based upon the θ values.

In the discretization process, it is important to make sure a certain level of connectivity especially near a well, since the well performance is sensitive to the near well reservoir characteristics. In this research, we use step = 4 as a default size for this reason. The following figures describe what may happen with the small step size: the undesirable intervals (Figure 46) and ideal intervals (Figure 47).

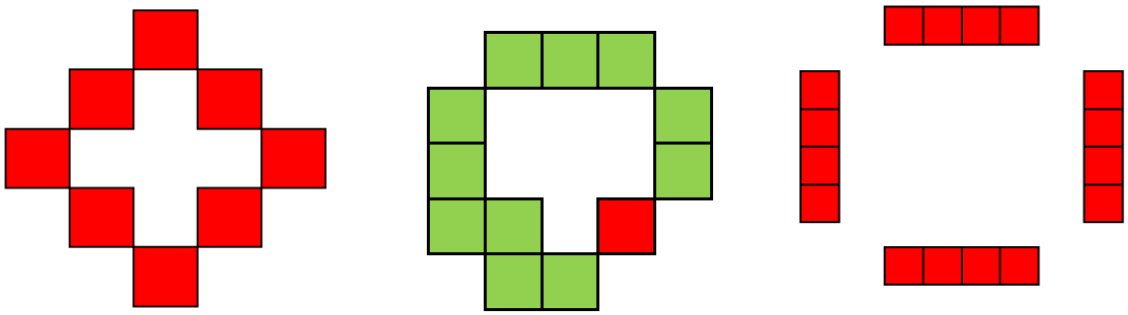

Figure 46 Undesirable Cases for PSS Gridding

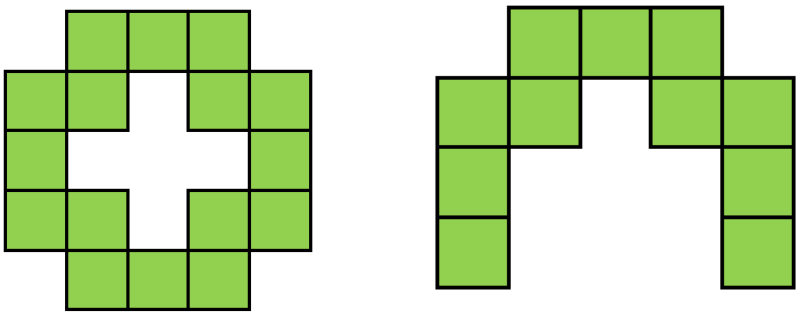

Figure 47 Ideal Cases for PSS Gridding

Here, we take an example of the synthetic study used in 5.1 (V_{DP}=0.68) and examine the impact of the interval continuity for the BHP calculation using PSS-SIM. The reservoir and well properties are shown in Table 18 and Table 19, respectively. The same fluid properties are used in the case study as for FMM-DTOF and PSS-DTOF in (Table 3). To change the level of continuity, we can test the pressure transient profile with different step size in the process of dilation and erosion (see Section 3.6.1.1). Figure 48 represents the discretized intervals with step size of 1 (left) and 4 (right), respectively. While the right figure has sufficiently smooth continuity for each upscaling interval near the well, the left figure has a poor degree of continuity for each interval.

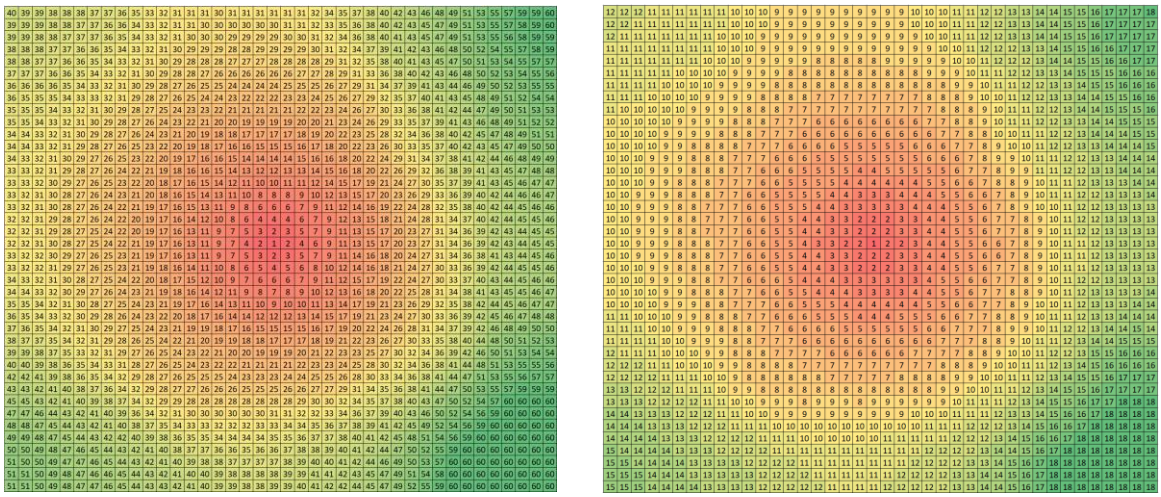

Figure 48 Upscaling Intervals: Step Size = 1 (left) and 4 (right)

Using these two different intervals, we examine the impact on the pressure transient response. (The transmissibility and well index needed for these calculations will be described next, but here we wish to focus on the impact of the grid design.) Figure 49 represents the pressure transient profile with two different step sizes: step = 1 and 4. The blue dots and cross points show ECL numerical simulation results, and the red solid and dash lines denote the results based on PSS-SIM with step size = 4 and 1, respectively. It can be observed that the poor level of interval continuity provides a less accurate pressure transient solution, although the equation systems to be solved are the same.

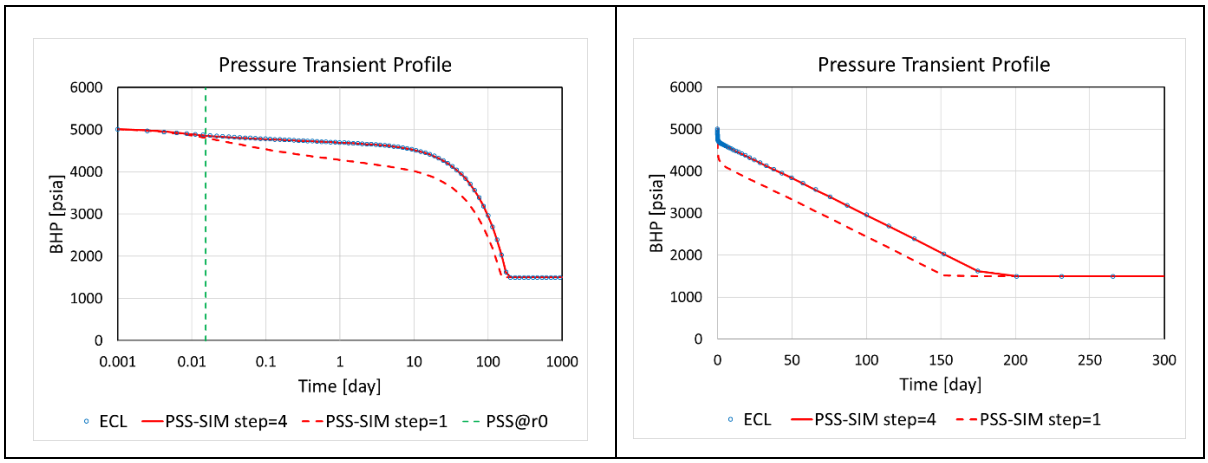

Figure 49 Pressure Transient Profiles with Different Step Size (V_{DP}=0.68)

This case study indicates that the importance of a sufficient level of interval continuity in the process of grid design.

3.6.1.2. Transmissibility Calculation

In this section, we formulate and obtain local PSS pressure solutions to derive the half cell transmissibility for grid interval i $(i=1,...,N)$, following the procedures proposed by (Nunna & King, 2020; Nunna et al., 2018). Since transmissibility is an intrinsic property, we consider a single phase with uniform viscosity and PSS flow to derive the half cell transmissibility.

Figure 50 describes the concept of flow based upscaling for each half cell transmissibility. In this example, θ_m represents the volume of the grid interval and $\partial\theta_m^{\pm}$ denotes the boundary at each side.

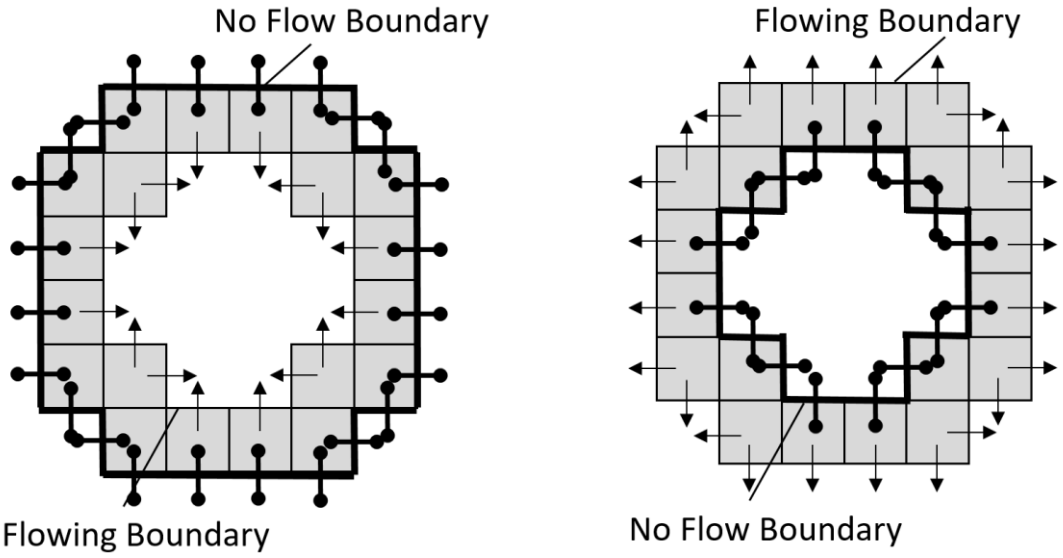

Figure 50 Transmissibility Upscaling Boundary Conditions for T_m^- (left) and T_m^+ (right)

Under the PSS, every fine cell plays a role as a source term which is proportional to its pore volume. In the process of upscaling, we set a flowing face boundary on one side and a non-flowing boundary on the other side. In the left hand side of Figure 50, we calculate the half cell transmissibility of minus direction, by setting up the flowing boundary on that side and no-flowing boundary on the other side. Flipping these boundary condition gives the solution for the half cell transmissibility of plus direction. In each case, we have an isobar where the pressure is set to zero on the flowing face, and the pressure on the other side is the average pressure of the pressures on the black face of each fine cell, which is a solution of finite difference simulation. Based on the pressure difference of these two sides, Δp^{PSS}, we calculate the half cell transmissibility for each direction.

The face flux q_f can be expressed in terms of transmissibility and pressure drop as Eq. (3.15).

$$q_f = \frac{T}{\mu}\Delta p^{PSS} \tag{3.15}$$

Within each PSS coordinate interval, the diffusivity equation Eq. (3.5) can be written as Eq. (3.16).

$$\nabla \bullet \left(-\frac{1}{\mu}\vec{\vec{k}}\left(\vec{x}\right) \bullet \nabla p\left(\vec{x}\right) \right) = \phi\left(\vec{x}\right) \tag{3.16}$$

Taking the integral of Eq. (3.16) gives us the normalized flux in each face.

$$q_f = \int_{\theta_m} \nabla \bullet \left(-\frac{1}{\mu}\vec{\vec{k}}\left(\vec{x}\right) \bullet \nabla p\left(\vec{x}\right) \right) d^3x = \int_{\theta_m} \phi\left(\vec{x}\right) d^3x \tag{3.17}$$

Here, the normalization of the pressure is arbitrary, because only the normalized pressure drop is needed for the transmissibility calculation. Since this is a 2nd order PDE we need two boundary conditions to solve the system.

$$p = 0 \quad @\, FlowingFace \tag{3.18}$$

$$\vec{n} \bullet \vec{\vec{k}} \bullet \nabla p = 0 \quad @\, NonFlowingFace \tag{3.19}$$

First, we consider transmissibility at face $\partial\theta_m^-$, described in the left hand side of Figure 50. Due to the boundary condition expressed as Eq. (3.18), pressure at the downstream faces become zero. Next, flux vanishes at the non-flowing face, which is described as black bars.

The upscaling calculation utilizes connection pressures as the isobar pressures on the flowing boundary, and an average pressure on the non-flowing boundary. Both quantities can be obtained from the derivation shown in the next two equations based on the conservation of the total flux, q_f, given as a sum of fluxes between cells "n" and cells "m".

$$q_f = \sum_{n,m} q_{nm} = \frac{1}{\mu}\sum_{n,m} T_{nm} \cdot \left(p_n - p_m \right) = \frac{2}{\mu}\sum_{n,m} T_{nm} \cdot \left(p_n - \bar{p} \right) = \frac{2}{\mu}\sum_{n,m} T_{nm} \cdot \left(\bar{p} - p_m \right) \tag{3.20}$$

$$\bar{p} \cdot \sum_{n,m} T_{nm} = \frac{1}{2}\sum_{n,m} T_{nm} \cdot \left(p_n + p_m \right) = -\frac{1}{2}\mu q_f + \sum_{n,m} T_{nm} \cdot p_n = \frac{1}{2}\mu q_f + \sum_{n,m} T_{nm} \cdot p_m \tag{3.21}$$

The derivation shows that the pressure of each connection is a simple average, $(p_n + p_m)/2$ and that the average pressure over all of the "nm" connections is transmissibility weighted. These averages are uniquely specified by flux conservation.

Here, Eq. (3.20) represents Darcy's equation on the flowing boundary. q_f is the total flux on the flowing face. p_n denotes the pressure of the fine cell facing to the flowing boundary in the interval, and p_m denotes the pressure of neighbor of the fine cell *n*, which is outside the interval across the flowing boundary. $\bar{p}$ is the average pressure on the flowing face, which is set to zero as a boundary condition (3.18). On the other hand, Eq. (3.21) represents Darcy's equation on the no-flowing boundary. q_f is the total flux on the flowing face, which is set to zero as a boundary condition (3.19). p_n denotes the pressure of the fine cell facing to the no-flowing boundary in the interval, and p_m denotes the pressure of neighbor of the fine cell *n*, which is outside the interval across the no-flowing boundary. $\bar{p}$ is the average pressure on the no-flowing face.

In the same manner as Section 3.3, the discrete form of the diffusivity equation can be expressed as Eq. (3.22).

$$\left\{ \frac{2}{\mu} \sum_{m(n)}^{\text{external flowing}} T_{nm} + \frac{1}{\mu} \sum_{m(n)}^{\text{internal}} T_{nm} \right\} \cdot p_n - \frac{1}{\mu} \sum_{m(n)}^{\text{internal}} T_{nm} \cdot p_m = V_{p,n} \tag{3.22}$$

Here, the coefficient, 2, is coming from $\frac{2}{\mu} \sum_{n,m} T_{nm} \cdot (p_n - \bar{p})$, where $\bar{p} = 0$ in Eq. (3.20). The solution of this equation gives the local pressure at each fine cell. Also, the face flux in Eq. (3.15) can be expressed in terms of intercell transmissibility and local pressure in fine cells as Eq. (3.23).

$$q_f = \sum_n \sum_{m(n)}^{\text{external flowing}} q_{nm} = \frac{2}{\mu} \sum_n \sum_{m(n)}^{\text{external flowing}} T_{nm} \cdot p_n = \sum_n V_{p,n} \tag{3.23}$$

This is simply a discrete form of Eq. (3.17). Next, we calculate the average pressure on the non-flowing face. With the expression of intercell transmissibility T_i ,we can obtain the equation about the average pressure.

$$\Delta p^{PSS} = \sum_n \sum_{m(n)}^{\text{external NoFlow}} T_{nm} \cdot p_n \Bigg/ \sum_n \sum_{m(n)}^{\text{external NoFlow}} T_{nm} \tag{3.24}$$

This equation means the average pressure on non-flowing face of $\partial\theta_m^+$ can be obtained by using the intercell transmissibility as a weight factor. Finally, substituting Δp^{PSS} and q_f to Eq. (3.15) gives the transmissibility at face $\partial\theta_m^-$.

Equally, we can obtain the transmissibility at face $\partial\theta_m^+$. In this case, the boundary condition of the flowing faces and no-flowing face flip as described in the right hand side of Figure 50. The calculation procedure is the same as half cell minus transmissibility at face $\partial\theta_m^-$. First, solving the matrix system shown as Eq. (3.22) gives you a local pressure at each fine cell. Next, the average pressure on no-flowing faces can be calculated by Eq. (3.24). Then, plugging Δp^{PSS} and q_f to Eq. (3.15) gives the transmissibility at face $\partial\theta_m^+$.

As a special case, the first interval consists solely of the perforated well blocks. The upscaled WI is calculated setting a summation of sink/source terms as a flowing face and non-flowing face on the other side. The equation to be solved is shown in Eq. (3.25).

$$\left\{ \frac{1}{\mu} \sum_n^{\#\text{Perforation}} WI_n + \frac{1}{\mu} \sum_{m(n)}^{\text{internal}} T_{nm} \right\} \cdot p_n - \frac{1}{\mu} \sum_{m(n)}^{\text{internal}} T_{nm} \cdot p_m = V_{p,n} \tag{3.25}$$

Equally, flipping these boundary conditions gives the half cell transmissibility on plus direction. The equation to be solved is expressed in the same form as Eq. (3.22). In this way, the corresponding WI and half cell transmissibility at face $\partial\theta_0^+$ should be equivalent to those of the 3D reservoir model.

3.6.1.3. Pressure Comparison

In this section, we provide a comparison of the solutions of the upscaled equations for the PSS and steady state pressure profiles against the analytical solutions. This serves as a test of the accuracy of the calculation of the transmissibility. The analytical solutions for each flowing state are shown below (Dake, 1983).

- PSS Equation (radial flow for a homogeneous bounded reservoir)

$$p^{PSS}\left(V_p\right) = p_{wf} + \frac{\mu q_t}{4\pi kh}\left\{\frac{V_{p,res}}{V_{p,res} - V_p\left(r_w\right)}\ln\left(\frac{V_p}{V_p\left(r_w\right)}\right) - \frac{V_p - V_p\left(r_w\right)}{V_{p,res} - V_p\left(r_w\right)}\right\} \tag{3.26}$$

- Steady State Equation (infinite radial flow for a homogeneous reservoir system)

$$p^{SS}\left(V_p\right) = p_{wf} + \frac{\mu q_t}{4\pi kh}\ln\left(\frac{V_p}{V_p\left(r_w\right)}\right) \tag{3.27}$$

Here, we express the pressure equations in terms of cumulative pore volume, instead of radius, because we are working on a system constructed under the 1D PSS coordinate, not under a radial coordinate.

Figure 51 is the comparison of the numerical pressure drop at each state. The LHS of the figure shows the cross plot of PSS pressure drop up to the point where the finite volume effect starts to appear (where we call the end of infinite radial flow). As for the numerical pressure drop at PSS, we can obtain the values at each grid interval by using cumulative pore volume in Eq. (3.26). In terms of the analytical pressure drop at PSS, we can derive the values by using the

radial pore volume shown in Figure 37 in Eq. (3.26). From this result, we can validate the transmissibility construction using the SS and PSS solutions. Next, the RHS of the figure shows the cross plot of steady state pressure drop. The numerical solution at steady state can be calculated as a cumulative of the inverse of the half cell transmissibilities $\sum_{i=0}^{n}\left(\frac{1}{T_i^-}+\frac{1}{T_i^+}\right)$ at grid intervals. Under PSS, the pressure drop across each interval is based on the dimensionless PSS flux $q_D(\tau)$ obtained from Eq. (1.27), in the long time $(t\to\infty)$ limit as $\sum_{i=0}^{n}\left(\frac{q_D(\tau_{i-1})}{T_i^-}+\frac{q_D(\tau_i)}{T_i^+}\right)$. The analytical pressure drop at steady state flow can be calculated by using the radial pore volume shown in Figure 37 in Eq. (3.27). This cross plot validates the calculated transmissibility is accurate against its analytical solution.

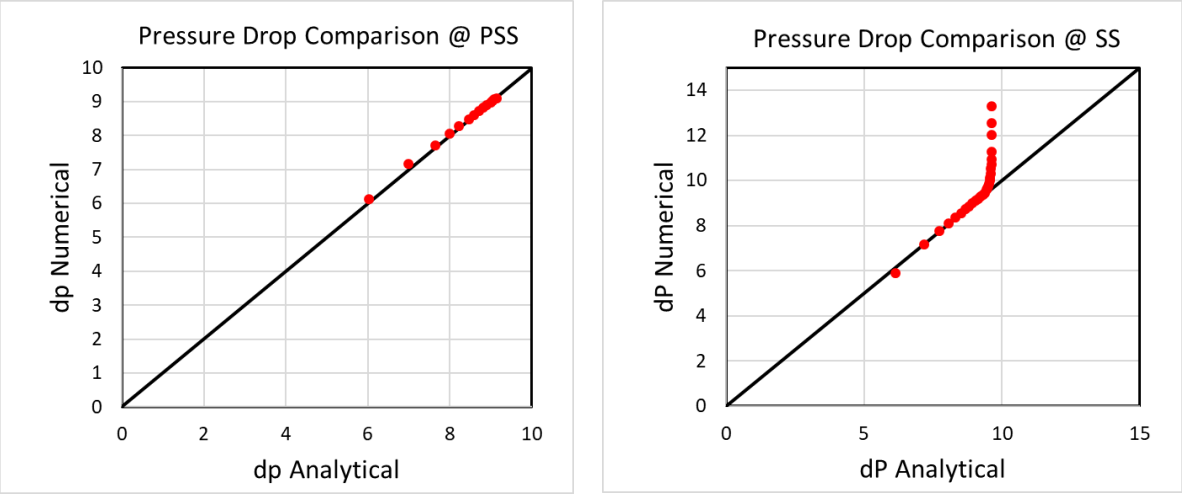

Figure 51 PSS (left) and Steady State Profile (right)

Lastly, we run numerical reservoir simulation based on the calculated transmissibility, ΔV_p and well index. As for the well index (which is also the well half cell transmissibility), the Peaceman Well Index is used in this section. Figure 52 is the comparison of BHP between PSS-SIM and ECL. The green vertical dash line represents the beginning of PSS at Peaceman radius.

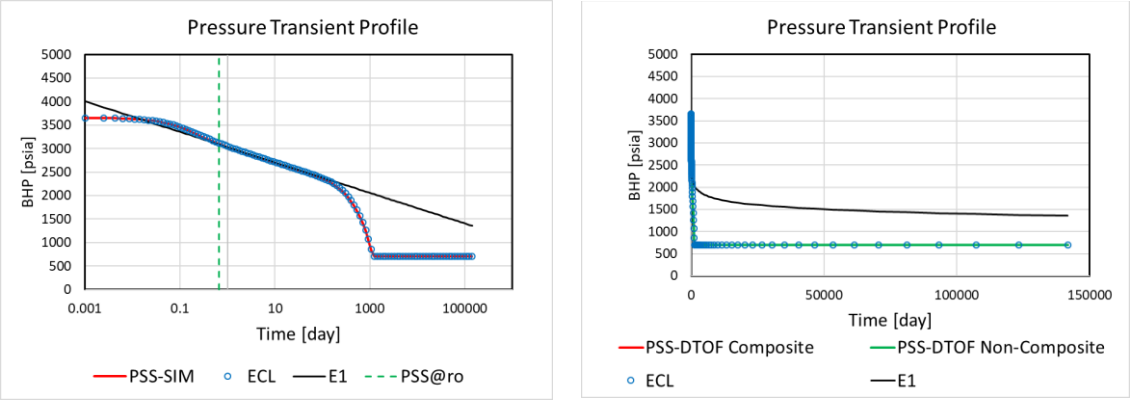

Figure 52 BHP: PSS-SIM based on the Upscaled PSS Coordinate Intervals

From the figure, you can see that both PSS-SIM match ECL well. The key point is that PSS-SIM is able to reproduce the 3D numerical finite difference simulation result with only 14 PSS intervals, although the original 3D reservoir model has 1681 cells. For increased accuracy at the very early time, we introduce LGR in the next section.

3.6.2. PSS Well Cell Local Grid Refinement

In this section, we develop a novel LGR treatment for the well cells in the 1D PSS-SIM model, in order to achieve improved accuracy for early time transients. This LGR construction will also improve the calculation of the DTOF based on the PSS coordinate in the next Chapter (Section 4.2.2).In a previous study, (Pedrosa & Aziz, 1986) developed an LGR for a well block through the use of a “hybrid” cell on the outer boundary of the LGR, which had characteristics of both radial flow and linear flow geometry. Here, we propose a different approach for LGR based upon a well-defined geometry and Darcy flux throughout the entire well cell, without the need for a hybrid boundary cell. Since Peaceman WI and transmissibility represents the radial flow and linear flow, respectively within each regime, we apply radial geometry within the Peaceman radius and linear geometry beyond that radius as described in Figure 53. In this way, the flow

geometry is consistent with WI and transmissibility, and thus the local grid construction is free from the geometry.

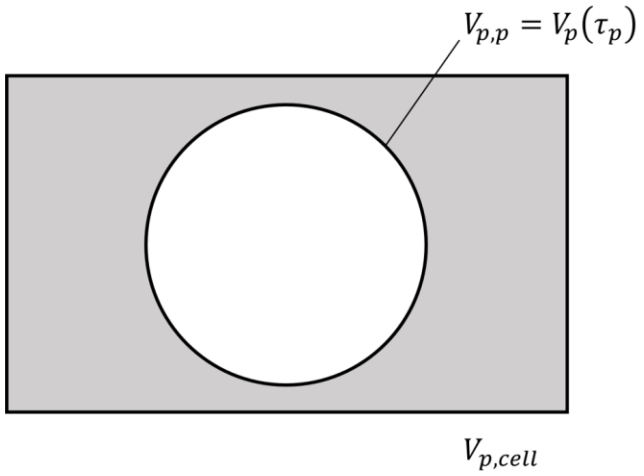

Figure 53 Local Composite Grid Geometry

In the case of FMM/SIM/DTOF, we also utilized a composite cell geometry, in that case up to τ_0, Figure 4. Here the composite flow geometry is designed to allow us to represent the well index and intercell transmissibility: radial flow up to the Peaceman radius and linear flow beyond that radius.

For the radial portion of the flow geometry, we can express Darcy's law as Eq. (3.28).

$$q = \frac{2\pi kh}{\mu} r \frac{\partial p}{\partial r} = \frac{4\pi kh}{\mu} V_p \frac{\partial p}{\partial V_p}, \quad 0 \le V_p \le V_{p,p} \tag{3.28}$$

In the case of multiple perforation wells, kh is a summation of the product of permeability and length of each cell along the well direction, consistent with the Well Index. $V_{p,p}$ is the pore volume out to the Peaceman radius. Similarly, for the linear portion of the flow, we can express

the pore volume as a rim element of the well block: $\Delta V_p = V_{p,cell} - V_{p,p}$. In terms of cumulative pore volume for a piecewise linear element, Darcy's law is expressed as Eq. (3.29).

$$q = \frac{T_{cell}^{+} \Delta V_p}{\mu} \frac{\partial p}{\partial V_p}, \quad V_{p,p} < V_p \le V_{p,cell} \tag{3.29}$$

Here, T_{cell}^{+} denotes twice the intercell transmissibility from the well cell to the next interval. We can verify Eq. (3.28) and Eq. (3.29) recovers the equivalent WI and the half cell transmissibility from the steady state pressure drops Δp_{SS}. By taking the integrals of these equation, we obtain Eq. (3.30) and Eq. (3.31).

$$\frac{1}{\mu q} \Delta p_{SS} = \frac{1}{4\pi kh} \int_{Wellbore}^{Peaceman} \frac{dV_p}{V_p} = \frac{1}{4\pi kh} \ln\left(\frac{V_{p,p}}{V_{p,w}}\right) = \frac{1}{WI} \tag{3.30}$$

$$\frac{1}{\mu q} \Delta p_{SS} = \frac{1}{T_{cell}^{+} \Delta V_p} \int_{Peaceman}^{Cell} dV_p = \frac{1}{T_{cell}^{+}} \tag{3.31}$$

Combine these expressions for Darcy's law into a function $\kappa\left(V_p\right)$, we can express Eq. (3.28) and (3.29) into Eq. (3.32).

$$q = \frac{1}{\mu} \kappa\left(V_p\right) \frac{\partial p}{\partial V_p}, \quad 0 \le V_p \le V_{p,cell} \tag{3.32}$$

$$\kappa\left(V_p\right) = \begin{cases} 4\pi kh V_p & 0 \le V_p \le V_{p,p} \\ T_{cell}^{+} \Delta V_p & V_{p,p} < V_p \le V_{p,cell} \end{cases} \tag{3.33}$$

We can then evaluate the PSS pressure drops for an arbitrary interval from $V_{p,a}$ to $V_{p,b}$, where $0 < V_{p,a} < V_{p,b} \le V_{p,cell}$. This gives us expressions for the directional half cell transmissibilities. By the definition of transmissibility, the transmissibility can be expressed in terms of face flux q_f and pressure drop Δp^{PSS} as shown in Eq. (3.15). When considering T_{ab}^{-}, the flux q at any location in the interval under PSS is expressed as Eq. (3.34).

$$q^{PSS} = q_f \left(\frac{V_{p,b} - V_p}{V_{p,b} - V_{p,a}} \right) \tag{3.34}$$

Equally, the flux q at any location in the interval is expressed as Eq. (3.35), in the case of T_{ab}^{+}.

$$q^{PSS} = q_f \left(\frac{V_p - V_{p,a}}{V_{p,b} - V_{p,a}} \right) \tag{3.35}$$

Substituting Eq. (3.34) or (3.35) to Eq. (3.32) gives us Eq. (3.36) and (3.37).

$$\frac{1}{T_{ab}^{-}} = \int_{V_{p,a}}^{V_p^c} \frac{dV_p}{\kappa\left(V_p\right)} = \left(V_{p,b} - V_{p,a}\right)^{-1} \int_{V_{p,a}}^{V_{p,b}} \frac{V_{p,b} - V_p}{\kappa\left(V_p\right)} dV_p \tag{3.36}$$

$$\frac{1}{T_{ab}^{+}} = \int_{V_p^c}^{V_{p,b}} \frac{dV_p}{\kappa\left(V_p\right)} = \left(V_{p,b} - V_{p,a}\right)^{-1} \int_{V_{p,a}}^{V_{p,b}} \frac{V_p - V_{p,a}}{\kappa\left(V_p\right)} dV_p \tag{3.37}$$

These two expressions are consistent since the SS solution can be obtained from the sum of the two PSS solutions.

This is a generalization of the LGR by (Pedrosa & Aziz, 1986) in that:

- the flow regime for the inner and outer faces of the hybrid interval are replaced with a more rigorous construction based upon the cell volumes
- it is consistent with the Cartesian transmissibility for the well cell and includes the effects of reservoir heterogeneity in adjacent cells
- the transmissibility is not limited by the spacing of the LGR grid intervals

In the case of simplest example with $NL = 1$:

$$\begin{aligned} \frac{V_{p,cell} - V_{p,w}}{T^{-}} &= \int_{Wellbore}^{Peaceman} \frac{\left(V_{p,cell} - V_p\right)}{4\pi khV_p} dV_p + \int_{Peaceman}^{Cell} \frac{\left(V_{p,cell} - V_p\right)}{T_{cell}^{+} \Delta V_p} dV_p \\ &= \frac{1}{4\pi kh} \left\{ V_{p,cell} \cdot \ln\left(\frac{V_{p,p}}{V_{p,w}} \right) - \left(V_{p,p} - V_{p,w}\right) \right\} + \frac{\left(V_{p,cell} - V_{p,p}\right)}{2T_{cell}^{+}} \end{aligned} \tag{3.38}$$

$$\begin{aligned} \frac{V_{p,cell} - V_{p,w}}{T^{+}} &= \int_{Wellbore}^{Peaceman} \frac{\left(V_p - V_{p,w}\right)}{4\pi khV_p} dV_p + \int_{Peaceman}^{Cell} \frac{\left(V_p - V_{p,w}\right)}{T_{cell}^{+} \Delta V_p} dV_p \\ &= \frac{1}{4\pi kh} \left\{ \left(V_{p,p} - V_{p,w}\right) - V_{p,w} \cdot \ln\left(\frac{V_{p,p}}{V_{p,w}} \right) \right\} + \frac{V_{p,cell} + V_{p,p} - 2V_{p,w}}{2T_{cell}^{+}} \end{aligned} \tag{3.39}$$

In the line source limit, $1/T^{-} \to 1/WI \to \infty$, as expected, while $1/T^{+}$ remains finite. In the following case studies, we discretize the radial section into 10 elements logarithmically and compare the well performance against the non-LGR case.

Next, we make an analysis of steady state pressure drop against analytical solutions. The analytical solutions used for the validation process can be calculated using Eq. (3.27), in the same manner as we did in Section 3.6.1.3. The numerical solution for the PSS pressure drop at linear sections (outside of the root cells) are the same as Figure 51. Figure 54 is the comparison of the numerical pressure drop, which is the summation of inverse transmissibility, with the analytical pressure drop calculated using Eq. (3.27). The cross plot matches the analytical solution until the end of the infinite radial flow. This can be a validation of transmissibility calculation.

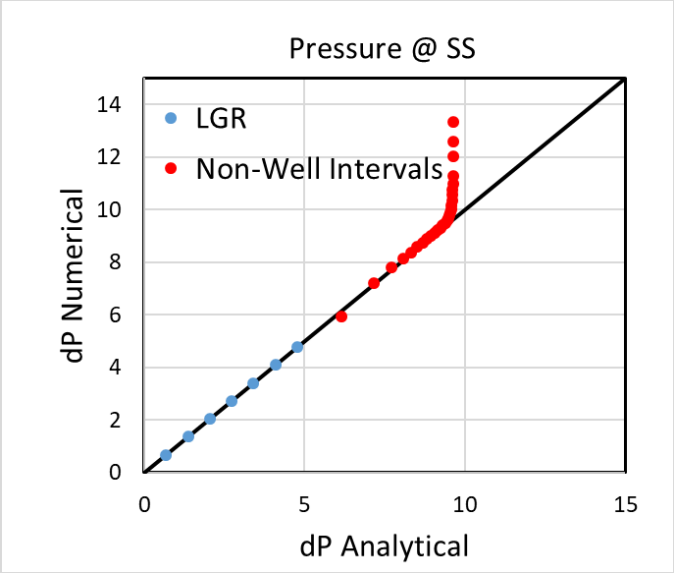

Figure 54 Steady State Pressure Drop Profile with LGR

Lastly, we run ECL simulation based on the calculated transmissibility, ΔV_p and well index. As for the well index, the numerically calculated half-cell transmissibility is used. Figure

55 is the comparison of BHP between PSS-SIM and ECL. The green vertical dash line represents the beginning of PSS at Peaceman radius.

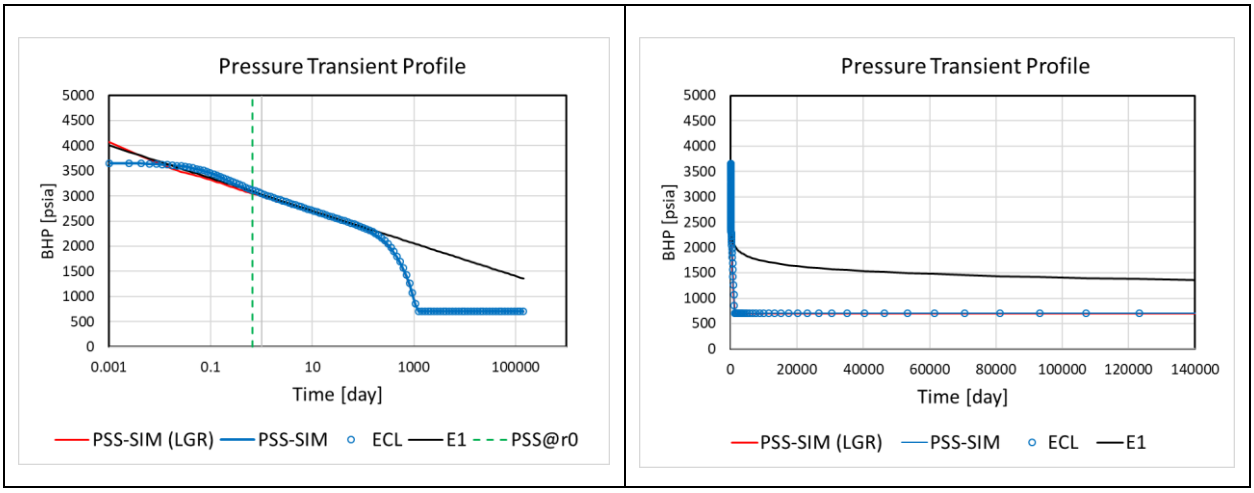

Figure 55 Pressure Transient Profile with LGR

This pressure profile demonstrates the capability of PSS-SIM to improve the accuracy at the early time transient by performing LGR for the root cell. The major benefit over the LGR for FMM-SIM/DTOF is that we have well-defined flow geometry and that WI and half cell transmissibility are consistent with the geometry. Hence, the corresponding WI and transmissibilities are free from the LGR grid intervals. The same concept is applied to PSS-DTOF in Chapter 4 again.

3.7. Case Studies

3.7.1. 2D Heterogeneous Model

- Input

The model is tested against the 2D heterogeneous reservoir, which was used for the FMM-DTOF case study. The reservoir and fluid properties are the summarized in Table 5 and Table 13, respectively. The reservoir case used in the test is moderately heterogeneous (V_{DP} =

0.64) and its permeability field is the same as Section 1.7.2, described in Figure 11. The production constraint and rate are also the same as Table 6. In this study, we applied PSS-SIM without LGR in order to show the ability to match the well performance against ECL. Through the process of the coordinate transformation, 1,681 Cartesian cells in the 2D reservoir model were transformed to only 13 intervals under the 1D PSS coordinate.

- Result

The pressure transient profile is shown in Figure 10. Here, we used PSS-SIM without LGR, since our purpose of this section is to match against ECL. The red and blue lines represent the PSS-SIM and FMM-SIM based production forecast, respectively. The blue dots denotes ECL result The left figure is along logarithmic time scale, and the right is along linear scale.

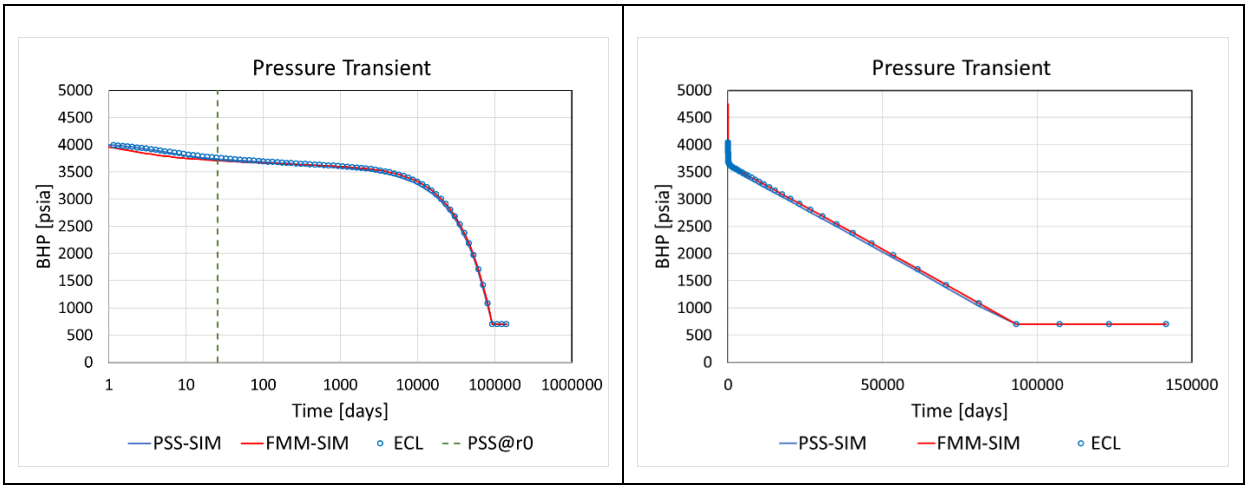

Figure 56 Pressure Transient for Fixed Rate Drawdown of a Heterogeneous Single Well Reservoir

The case study validates the accuracy of the developed model against the heterogeneity. Since this reservoir model is 2D (no inner boundary superposition effect) and the level of

heterogeneity $\left(V_{DP}=0.64\right)$ is not as high as the field model used in Section 2.5, both FMM-SIM and PSS-SIM can reproduce the 3D finite difference simulation result.

3.7.2. Single Well Field Case

- Input

As the last step of the case study using PSS-SIM, we go back to the original problem we could not solve with FMM-DTOF. The field model for the test is the same one used in Section 2.5 (The model description is made in this section). Since PSS-SIM, as well as FMM-SIM, cannot perform superposition to handle multiple wells at the same time, we set up only one production well B2. The well produces oil at target rate at first, and shift to BHP constraint later in the same manner as Section 2.5.

- Result

The figure below (Figure 57) shows the pressure and rate transient profile based on PSS-SIM in comparison with FMM-SIM and ECL. The two blue and red lines denote PSS-SIM and FMM-SIM based results, respectively. Two dots represent ECL based forecasts. The grey vertical dash line denotes the time when Peaceman radius reaches the PSS.

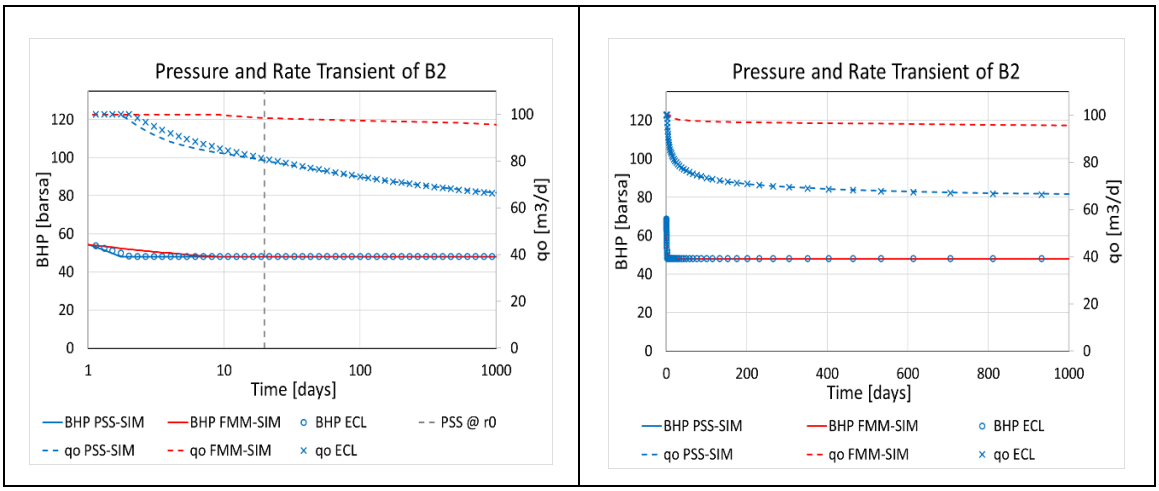

Figure 57 Pressure and Rate Transient Profile with the Field Model using PSS-SIM

In the previous study in Section 3.1, we could not match BHP or rate using FMM-SIM because the 1D DTOF coordinate is not well-aligned with actual pressure drop in the reservoir. This is contradictory to its underlying assumption that we can ignore the pressure drop along each τ contour and have only to consider the pressure drop across contours. Here, however, both BHP and rate match the ECL FD-SIM using PSS-SIM. This result supports the analysis made in Section 3.5 that the normalized pressure drop at PSS itself is a better coordinate for 1D numerical reservoir simulation rather than the DTOF coordinate.

3.7.3. Single Well Field Case with Low Production Rate

To emphasize the study conducted in the previous section (Section 3.7.2), we perform the comparison using a low production rate $\left(q_o = 50 sm^3 / day\right)$ so that the well does not hit the BHP constraint. Figure 58 represents the corresponding pressure/rate transient profiles. The two blue and red lines denote PSS-SIM and FMM-SIM based results, respectively. The dots represent ECL based forecasts. The grey vertical dash line denotes the time when the Peaceman radius reaches PSS.

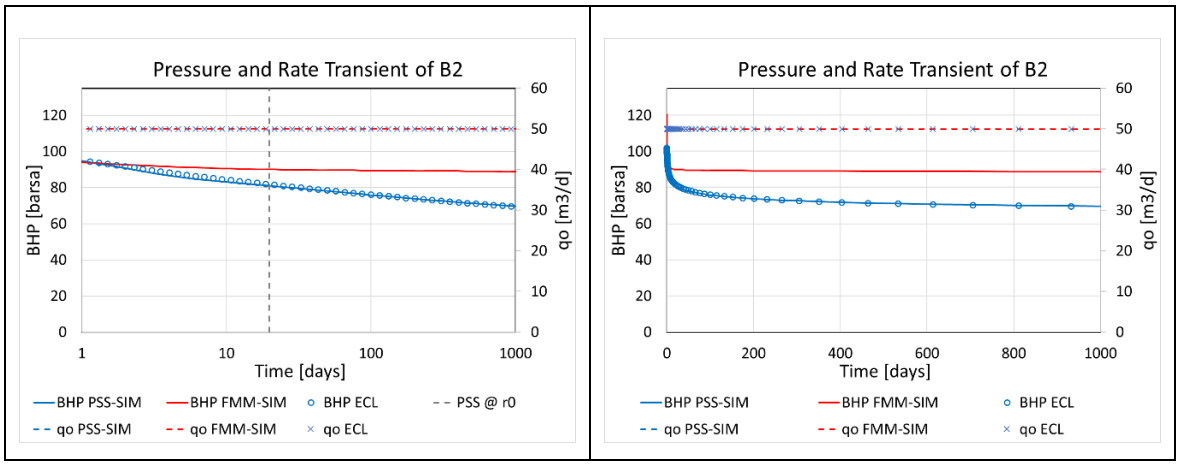

Figure 58 Pressure and Rate Transient Profile with the Field Model using Low Rate

From this figure, we can confirm that although there is no discrepancy in pressure at the very early time (1 day) regardless of methods, FMM-SIM starts to go off in the mid-late time in comparison of ECL. On the other hand, PSS-SIM excellently follows the pressure transient trend of ECL. This result, together with Section 3.7.2, indicates the importance of having a well-aligned 1D coordinate with reservoir pressure drop. Here this example shows the impact of near well superposition effects, which are not captured by the DTOF coordinate.

3.8. Discussion

In the previous chapter, we learned that the use of the DTOF as a 1D spatial coordinate has some limitations for general field applications, while it works well with reservoir models which are moderately heterogeneous and where the well is placed far away from the reservoir boundary. In this chapter, we clarified that the mismatch we have seen in Section 2.5 is because the 1D DTOF coordinate may not be a good representation of actual pressure drop contours in the reservoir. Although the strength of transformed 1D reservoir simulation is in its speed-up due to the coordinate reduction from 3D to 1D, it cannot capture the pressure drop which is generated in other dimensions except for the transformed 1D coordinate. Thus, it is quite important to make

sure that the transformed 1D coordinate best describes the pressure drop of the entire reservoir. As a solution for the issue, we proposed using PSS pressure drop itself as a spatial coordinate for fast numerical simulation and derived transmissibility and corresponding drainage volume within each interval for numerical simulation. Throughout the study, we learned:

- The DTOF coordinate may not be a good representation for mid/late time pressure drop under high heterogeneity or strong boundary effects. The flow regime can be affected not only by the external reservoir boundary, but also by the inner boundary, such as a fracture or other part of perforations
- The PSS coordinate is a better representation of the reservoir pressure drop even after the flow geometry changes into boundary dominated flow
- By taking the first interval of PSS-SIM solely consisting of well blocks, we can generate the same trend of ECL based well performance
- LGR can be applied for the further accuracy at the very early time by taking the radial flow geometry up to Peaceman radius and linear flow geometry beyond that

In the next chapter, in order to apply this method for multiple well reservoir development, we are going to derive and solve a 1D discrete form of the Eikonal equation for the DTOF from the PSS coordinate, which is expected to be better-aligned with the reservoir pressure drop than obtained from the FMM solution. Then, we develop the semi-analytic simulation based on the 1D PSS coordinate and show how to apply it for multiple well models.

4. ASYMPTOTIC PRESSURE SOLUTION BASED ON PSS COORDINATE (PSS-DTOF) AND ITS APPLICATION FOR MULTIPLE WELL RESERVOIR DEVELOPMENT

4.1. Objective of Chapter

In the previous chapter, we showed the application of PSS pressure drop as a spatial coordinate for numerical reservoir simulation. In this chapter, we will show how to obtain the DTOF coordinate directly from the 1D form of the Eikonal equation and the PSS intervals, without the need for the FMM solution. Although the numerical simulation will be more accurate than the asymptotic pressure approximation, the asymptotic approach has its strength in fast computational speed, since it does not require solving numerical finite difference problems for pressure. Besides, it can be easily extended to multiple well reservoir development by means of superposition of pressure drops attributed from each well in the same manner as Chapter 2. In the case of FMM-DTOF developed in Chapter 2, the pressure/rate transient had a discrepancy against 3D numerical finite difference simulation in the case of highly heterogeneous models. PSS-DTOF will overcome this shortcoming because of the advantage of better alignment with the pressure solution than FMM-DTOF.

In this section, we first show how to solve a 1D discrete form of the Eikonal equation to calculate the DTOF from the PSS interval obtained from Chapter 3. Next, we solve asymptotic pressure problem in the 1D coordinate, which is followed by some case studies. Lastly, we extend the system for a single well model to multiple well reservoir development and perform a field application to see how much better PSS-DTOF performs in comparison with FMM-DTOF we derived in Chapter 2.

4.2. Derivation of the Asymptotic Pressure Solution

4.2.1. 1D Eikonal Equation based on the PSS Intervals

In order to develop PSS-DTOF, we need to obtain DTOF, τ . In this section, we consider deriving the discrete form of the Eikonal equation from the PSS intervals, which is necessary for the asymptotic pressure approximation. First, as we derived in Section 1.2, the Eikonal equation in a 3D reservoir model is written as Eq. (1.5) with the boundary condition of $\tau = 0$ at $r = 0$ for each perforation. In the case of a 1D reservoir model, the derivative of τ is simply a gradient along the x coordinate. Thus, Eq. (1.5) can simply be converted to Eq.(4.1).

$$\sqrt{\frac{c_t \phi}{\lambda_{rt} k}} = \left(\frac{d\tau}{dx} \right) \qquad (4.1)$$

$$\tau = 0 \quad at \quad x = 0$$

Using this relation, we can express $\Delta\tau$ with respect to the 1D distance Δx as shown in Eq. (4.3).

$$\Delta\tau = \Delta x \sqrt{\frac{c_t \phi}{\lambda_{rt} k}} \qquad (4.3)$$

We express Eq. (4.3) in terms of incremental pore volume and interval transmissibility in the discrete form.

$$\Delta\tau = \Delta x \sqrt{\frac{c_t \phi}{\lambda_{rt} k}} = \sqrt{\frac{c_t \left(\phi A \Delta x \right)}{\lambda_{rt} \left(kA/\Delta x \right)}} = \sqrt{\frac{c_t \Delta V_p}{\lambda_{rt} T}} \qquad (4.4)$$

$$\tau_n = \tau_{n-1} + \sqrt{\left(\frac{c_t \Delta V_p}{\lambda_{rt} T} \right)_n}, \quad n = 1, \ldots, N \qquad (4.5)$$

$$\tau_0 = \sqrt{\left(\frac{c_t \Delta V_p}{\lambda_{rt} T^+} \right)_0} \qquad (4.6)$$

In Eq. (4.5), T is the transmissibility across an interval, not the intercell transmissibility.

$$1/T_n = 1/T_n^- + 1/T_n^+ \qquad (4.7)$$

Here, λ_{rt} is a function of the initial saturation averaged in the PSS interval, and c_t is evaluated similarly. In Chapter 3, we already developed the incremental pore volume and the corresponding transmissibility in the 1D transformed PSS grid (from Eq. (3.15), (3.23) and (3.24)), so we can obtain τ using Eq. (4.5).

There are two ways to calculate the first τ interval. The simplest way is to apply the linear flow geometry to the first interval, as shown in Eq. (4.6). We will show that a more accurate calculation will apply a composite cell geometry for the first interval, considering the two different flow geometries in the cell: radial and linear (as we did in Section 3.6.1). As for the radial flow geometry, we have the corresponding WI and half cell transmissibility for plus direction obtained from Eq. (3.25) and (3.22), respectively. The radial flow regime ranges from $\tau = 0$ up to τ_p. Next, as for the linear flow geometry $\left(\tau_p \le \tau \le \tau_0\right)$, we can obtain τ using Eq. (4.8).

$$\tau_0 = \tau_p + \sqrt{\frac{\mu c_t \left(V_{p,cell} - V_{p,well}\right)}{T^+_{cell}}}, \quad @Composite \tag{4.8}$$

The linear grid intervals $\left(n = 1,...,N\right)$ can be obtained by Eq. (4.5). Then, in the same manner as FMM-DTOF, we can derive the relationship between local pressure and τ using Eq. (2.1).

Based on the constructed system, we conduct the validation to see if the asymptotic model can reproduce the same trend as ECL finite difference simulation. For the purpose of comparison, we examine PSS-DTOF using a composite cell geometry (radial and linear flow) for the first interval against PSS-DTOF without a composite cell treatment (only linear flow) in a well interval. Here, we take the same 2D homogeneous reservoir model used for PSS-SIM in Section 3.6. The reservoir, fluid and well properties are summarized in Table 15, Table 16 and

Table 17, respectively. The well placed at the center of the 2D reservoir model produces oil with a specified rate first and switches to BHP control. Figure 59 shows the pressure transient profile based on PSS-DTOF. The pressure transient profile of PSS-DTOF with the composite cell treatment is shown as a red line, and PSS-DTOF without a composite cell treatment is described as a green solid line. The black line represents the E1 analytical solution (Lee, 1982; Lee et al., 2003), and the blue dots correspond to ECL results. In this figure, the green vertical dash line denotes the time for PSS at the Peaceman radius. You can see that the forecasted BHP based on PSS-DTOF with the composite cell is exactly the same as the ECL finite difference result treatment at the very early time step. This is because WI is calculated based on the same flow geometrical assumption as ECL. On the other hand, PSS-DTOF without the composite cell treatment has a discrepancy at the early time against ECL. This comparison demonstrates the impact of the composite cell treatment for the well interval. For the mid time, both PSS-DTOF follow the E1 analytical solution until the end of infinite radial flow. Once the pressure front hits the external reservoir boundary, it starts to follow ECL due to the finite volume effect of the reservoir.

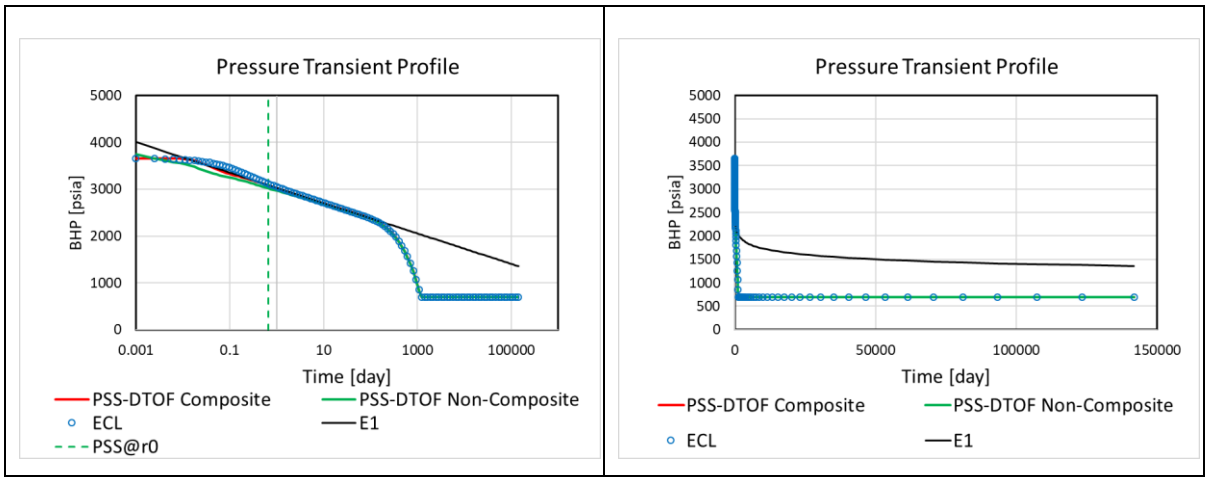

Figure 59 Pressure Transient Profile using PSS-DTOF

This case study shows the ability for PSS-DTOF to reproduce the ECL finite difference simulation result without solving numerical finite difference problem for pressure, and importance to apply well cell composite geometry..

4.2.2. LGR for the Well Cell

In this section, we consider applying LGR for the first interval. Since we have already obtained τ_p and τ_0 at the composite cell, we simply have to apply the same resolution as we did for FMM-DTOF in Section 1.6. Here, we perform LGR for the root cells into NL sub-elements. The elements from 1 through NL-1 correspond to the radial flow section and NL denotes the linear flow section up to the end of the root cells. In the radial section, the local cell interval is taken logarithmically to match the gridding system consistent with ECL (Schlumberger, 2019a).

Figure 60 represents the pressure transient profile using PSS-DTOF with LGR for the root cells. Likewise to Figure 59, the black line represents the E1 analytical solution, and the blue dots correspond to ECL. The red and blue lines are PSS-DTOF results with and without LGR, respectively. The green vertical dash line denotes the time for PSS at the Peaceman radius.

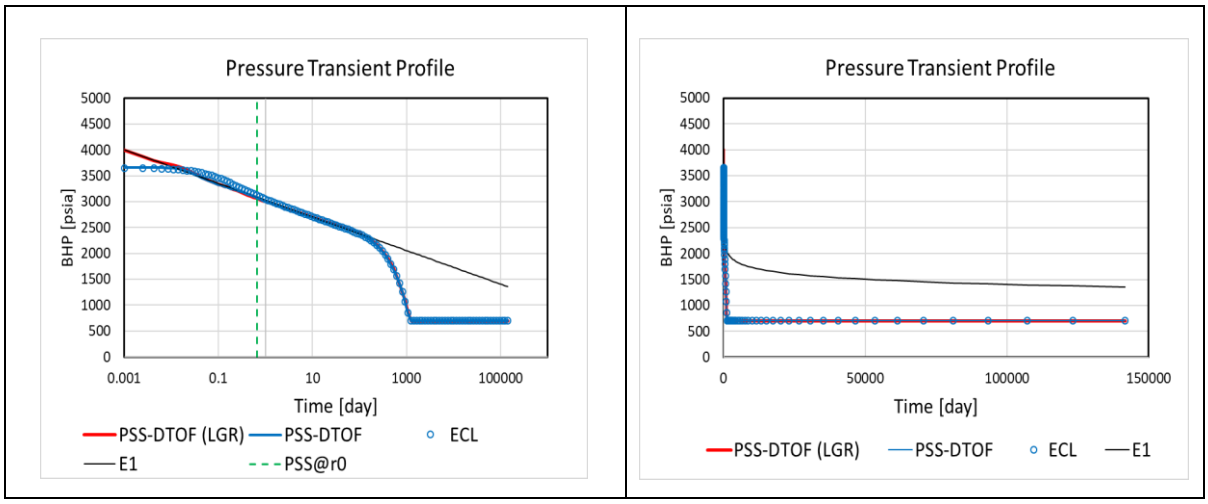

Figure 60 Pressure Transient Profile using PSS-DTOF with LGR

You can see that the forecasted BHP based on PSS-DTOF at the very early time step is now following the E1 analytical solution, instead of ECL, and starts to follow ECL due to the finite volume effect of the reservoir. This example shows the possibility for PSS-DTOF to improve the very early time accuracy by performing LGR.

4.3. Case Studies

4.3.1. 2D Heterogeneous Model

First, we conduct a case study with the same 2D synthetic heterogeneous model used for FMM-DTOF in Section 1.7.2. Since the objective of this section is to show the capability for PSS-DTOF to reproduce the trend of ECL result without the need of running the finite difference simulation under the PSS coordinate, we apply a composite well geometry for the first interval (without LGR). The reservoir, fluid and well properties are summarized in Table 5, Table 13 and Table 6, respectively. The permeability field is described in Figure 11. Figure 61 shows the pressure transient profile using PSS-DTOF in comparison with PSS-SIM and ECL finite

difference simulation. The blue dots and the red line correspond to ECL and PSS-DTOF results, respectively. The green vertical dash line denotes the time for PSS at Peaceman radius.

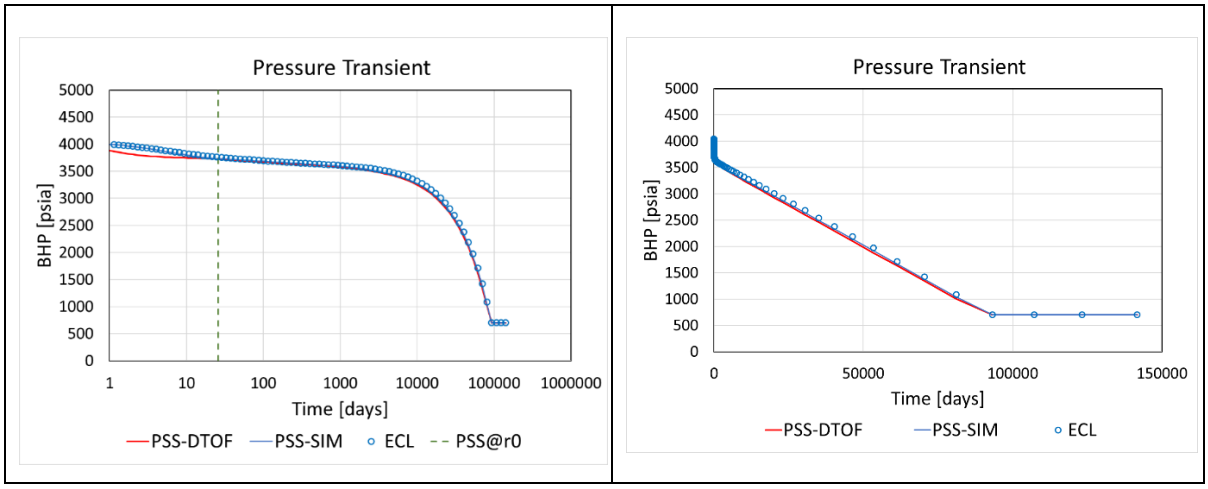

Figure 61 Pressure Transient Profile with 2D Heterogeneous Model using PSS-DTOF

From the figure, it can be observed that although there is small mismatch at the early time between PSS-DTOF and PSS-SIM, the pressure transient profile of PSS-DTOF follows the trend of ECL and PSS-SIM. This case study result can be a validation that PSS-DTOF is applicable even for heterogeneous media. Throughout the study, we have seen four different pressure solutions: FMM-SIM, FMM-DTOF, PSS-SIM and PSS-DTOF. In Chapter 5, all the four methods will be compared against each other with various level of heterogeneity.

4.3.2. 3D Field Model

Next, we perform a case study with the 3D field model which we could not get a good match with FMM-DTOF / FMM-SIM. Because of the same reason in Section 4.3.1, we use PSS-DTOF with a composite cell geometry for the first interval. The reservoir, fluid and well properties are summarized in Table 12, Table 13 and Table 14, respectively. The permeability field is described in Figure 31. Figure 62 shows the pressure transient profile using PSS-DTOF in comparison with PSS-SIM and ECL finite difference simulation. The blue dots and cross

correspond to BHP and rate based on ECL finite difference simulation. The grey vertical dash line denotes the time when the Peaceman radius becomes PSS. The red solid and dash line represent the BHP and rate based on PSS-DTOF. The blue solid and dash line represent the BHP and rate result based on PSS-SIM derived in Section 3.7.2.

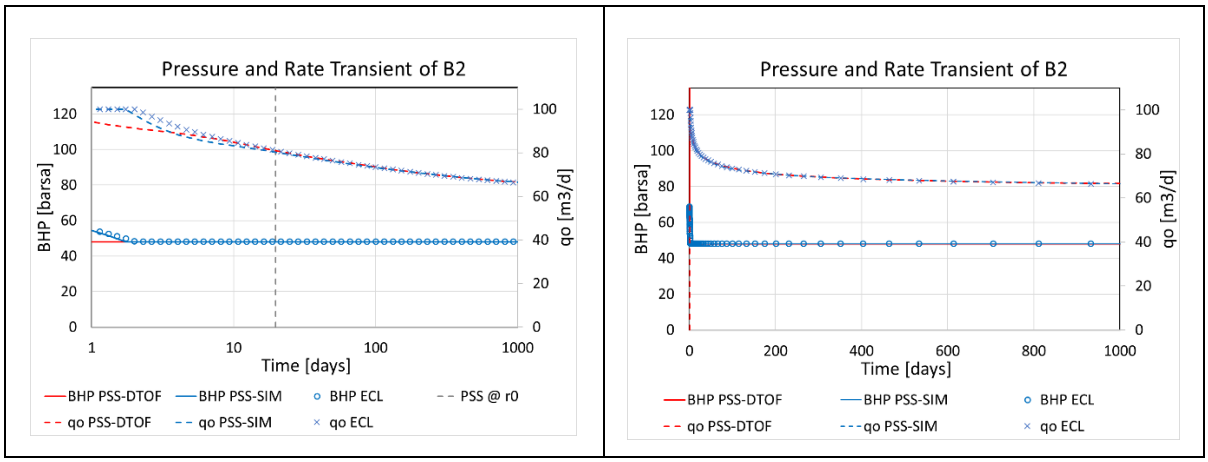

Figure 62 Pressure and Rate Transient Profile with the Field Model Using PSS-DTOF

From the figure, we can see that both BHP and rate follow the trend of ECL results, although there is small mismatch at the very early time. This result is consistent with that of Section 4.3.1. This case study, in comparison with the results based on FMM-DTOF/SIM, implies the importance of pressure difference alignment along with the constructed 1D coordinate.

4.4. Extension of PSS-DTOF to Multiple Well Reservoir Development

In the previous section, we have developed PSS-DTOF for a single well reservoir model. In this section, we extend the model to multiple well reservoir development. Since we have τ under each coordinate originated from each well, we can simply follow the same procedure as FMM-DTOF. We first need to calculate the pressure drop from the initial pressure at any location τ in each coordinate originated from each well, and then interpolate τ of a well

location under each spatial coordinate to get each pressure drop δp_j. Superposition of δp_j in each 1D coordinate gives us the total pressure drop at the well location.

Using the constructed system, we perform the field application. The field model used for this study is the same one as the model for FMM-DTOF (described in Section 2.4) to see how much improvement PSS-DTOF can make. The permeability field is described in Figure 26. V_{DP} in the model is 0.65, so the level of heterogeneity is "very heterogeneous" according to its definition (Dykstra & Parsons, 1950). The reservoir has five vertical production wells: one at the middle of the reservoir and four around it. The well produces oil at target rate at first, and shift to BHP constraint later. The reservoir and well properties are shown in the tables below (Table 10 and Table 11, respectively). The fluid properties are the same as Table 3. The permeability and porosity distribution are described in Figure 27 and Figure 28.

Figure 63 shows the production forecast based on PSS-DTOF against FMM-DTOF and ECL for each well. The blue dots and cross correspond to BHP and rate based on ECL finite difference simulation. The green and red line denote BHP and rate based on PSS-DTOF, respectively.

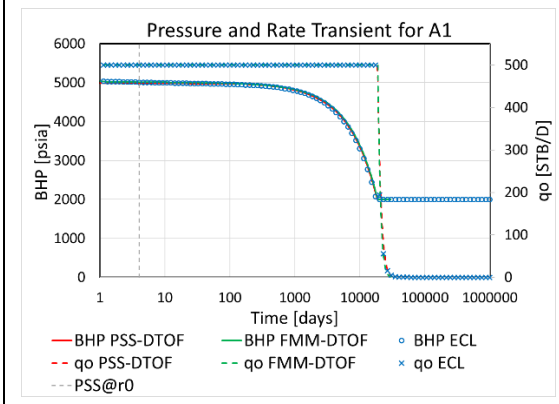
Pressure and Rate Transient for A1
BHP [psia]
qo [STB/D]
Time [days]
BHP PSS-DTOF
BHP FMM-DTOF
BHP ECL
qo PSS-DTOF
qo FMM-DTOF
qo ECL
PSS@r0

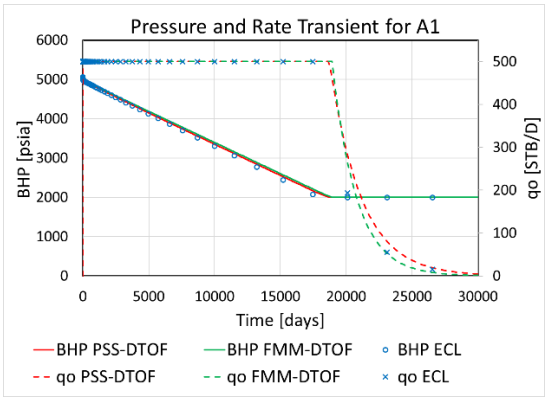
Pressure and Rate Transient for A1
BHP [psia]
qo [STB/D]
Time [days]
BHP PSS-DTOF
BHP FMM-DTOF
BHP ECL
qo PSS-DTOF
qo FMM-DTOF
qo ECL

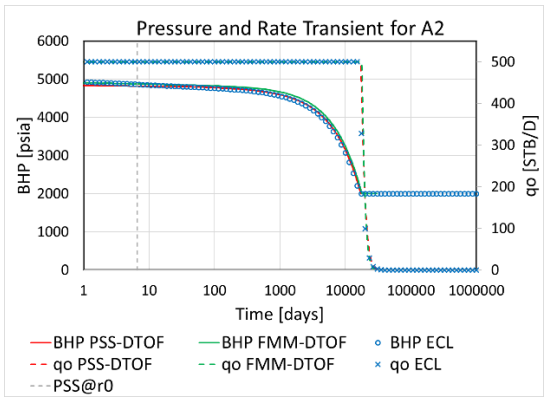
Pressure and Rate Transient for A2
BHP [psia]
qo [STB/D]
Time [days]
BHP PSS-DTOF
BHP FMM-DTOF
BHP ECL
qo PSS-DTOF
qo FMM-DTOF
qo ECL
PSS@r0

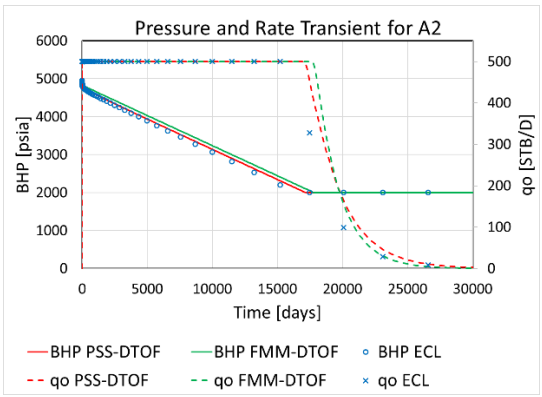
Pressure and Rate Transient for A2
BHP [psia]
qo [STB/D]
Time [days]
BHP PSS-DTOF
BHP FMM-DTOF
BHP ECL
qo PSS-DTOF
qo FMM-DTOF
qo ECL

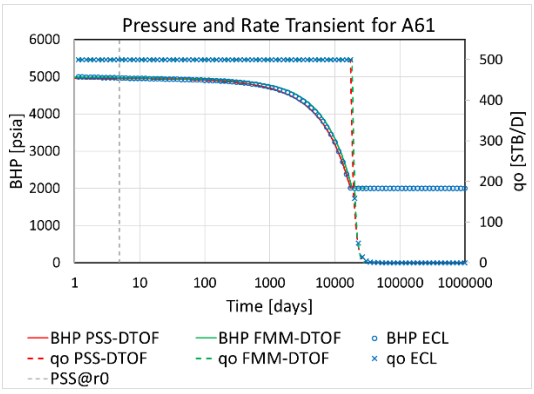
Pressure and Rate Transient for A61
BHP [psia]
qo [STB/D]
Time [days]
BHP PSS-DTOF
BHP FMM-DTOF
BHP ECL
qo PSS-DTOF
qo FMM-DTOF
qo ECL
PSS@r0

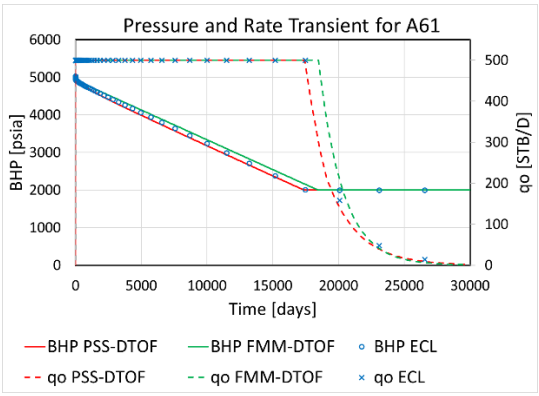
Pressure and Rate Transient for A61
BHP [psia]
qo [STB/D]
Time [days]
BHP PSS-DTOF
BHP FMM-DTOF
BHP ECL
qo PSS-DTOF
qo FMM-DTOF
qo ECL

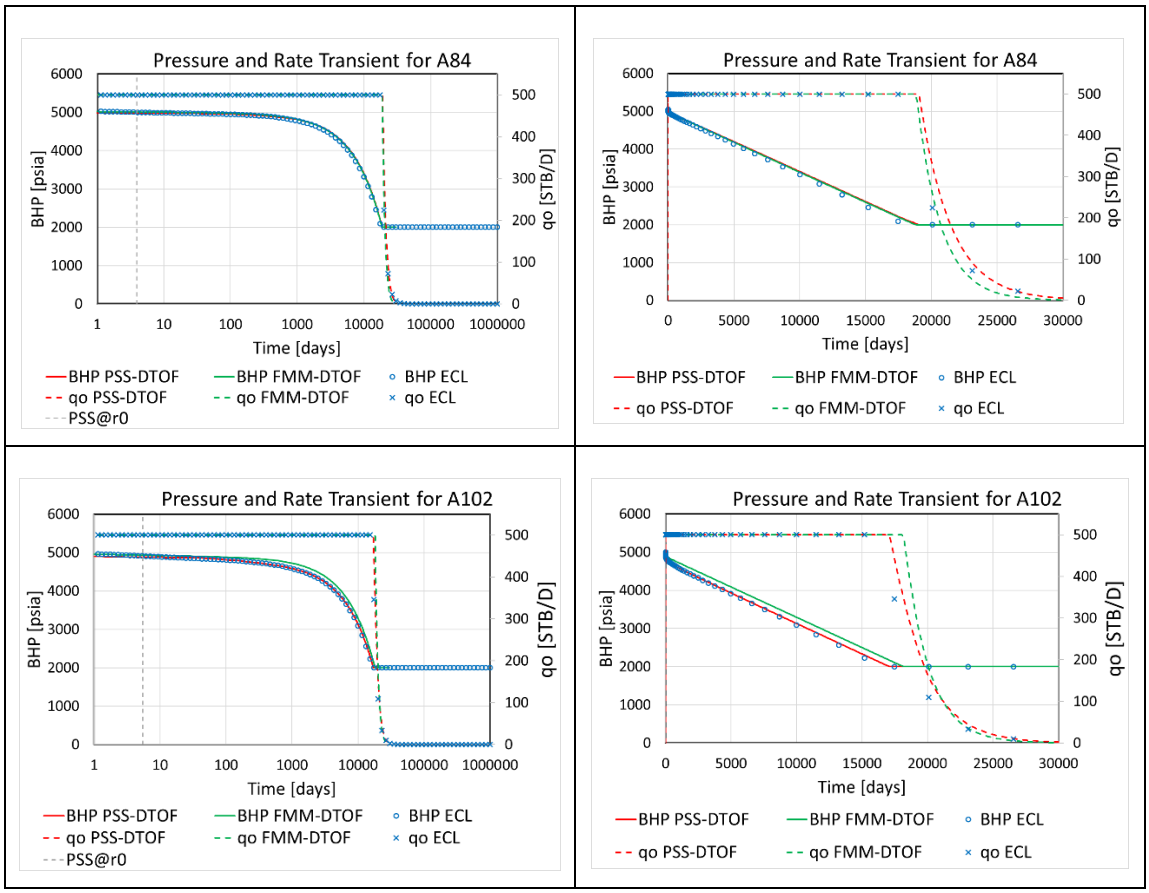

Figure 63 Pressure and Rate Transient for a Multiple Well Field Model Using PSS-DTOF and PSS-SIM

The rate transient profile is quite sensitive to the exact time when the well control switches to BHP constraint from the specified target rate, but both BHP and rate, by and large, match ECL results. In more details, FMM-DTOF had a mismatch in pressure transient profile if a well is positioned near the reservoir boundary (A2 and A102), it is noteworthy that those wells have a better match with ECL using FMM-DTOF regardless of their locations, as seen in A102. This case study can be a good validation that PSS-DTOF can handle multiple well reservoir development by means of superposition, and it also proves the superiority in the coordinate transformation in that the constructed coordinate has no limitation about well positioning.

4.5. Discussion

In the previous chapter, we derived a novel coordinate transformation approach and performed a numerical simulation to show the benefit to use the PSS pressure itself as a spatial coordinate. In this chapter, we developed an asymptotic pressure approximation approach to estimate pressure under the constructed 1D PSS coordinate without the need to solve a numerical finite difference equation for all the pressures within the reservoir. Since this is an asymptotic approximation, it is computationally lighter than the numerical reservoir simulation. Besides, we can easily extend the asymptotic approach to multiple well reservoir development by means of superposition of pressure drop attributed to each well. Throughout the study, we learned:

- Asymptotic pressure solution (PSS-DTOF) can reproduce the same pressure profile as the numerical simulation result (PSS-SIM)
- The constructed PSS coordinate is not sensitive to the well positioning, unlike FMM-DTOF / FMM-SIM as seen in Section 2.4
- Pressure drop at any location can be easily obtained by means of superposition of the pressure drop attributed to each well
- PSS-DTOF can reduce the size of the numerical problem. In the case of the filed model in Section 4.4, PSS-DTOF reproduced the 3D numerical finite difference simulation result only by solving for 11 unknows, although the 3D finite difference simulator needed to solve for 30,400 unknowns

In this research study, we introduced four different approaches to estimate reservoir pressure: FMM-SIM, FMM-DTOF, PSS-SIM and PSS-DTOF. In the final chapter, we conclude the research by making comparisons among all of these approaches with respect to various level of the reservoir heterogeneity.

5. ANALYSIS AND COMPARISON OF THE FOUR PRESSURE SOLUTIONS

This research started by the literature review about the asymptotic pressure approximation (FMM-DTOF) for a single well reservoir model (Chapter 1). We extended the system to be able to apply for multiple well reservoir development by means of superposition to see the limitation of FMM-DTOF (Chapter 2). In Chapter 3, we analyzed the cause of the mismatch between FMM-DTOF/SIM and ECL finite difference simulation, and proposed a fast numerical reservoir simulation based on the PSS as a spatial coordinate. In Chapter 4, we developed the asymptotic pressure approach based on the newly proposed PSS coordinate to apply for multiple well reservoir simulation. As a concluding chapter of the study, we make comparisons of these four pressure solutions.

5.1. Heterogeneity Effect

In Section 3.4, we observed that near a boundary, that the DTOF coordinate is not well-aligned with the pressure drop contour at the mid-late time and BDF (Figure 42 and Figure 43). Besides, we showed that it depends up on the reservoir heterogeneity and well location when the actual pressure drop starts to be off-aligned from the DTOF coordinate. In this section, we test the impact of the reservoir heterogeneity to the pressure and rate transient profile with various level of heterogeneity to see the applicability of the DTOF/PSS coordinates. Here, we prepared the three synthetic 3D reservoir models with increasing levels of heterogeneity: the standard deviation of reservoir permeability in a logarithmic scale is 0 (homogeneous), 0.2 and 0.5, which correspond to V_{DP} = 0, 0.36 and 0.68, respectively. The reservoir and well property are shown in Table 18 and Table 19, respectively. The same fluid properties are used in the case study as for FMM-DTOF and PSS-DTOF in (Table 3). The production well is located at the center of the

reservoir and is fully completed. The well produces oil at specified target rate until it reaches the BHP constraint (1500 psia). Figure 64 and Figure 65 represent the 3D permeability maps (left) and the permeability histogram (right) for each model: V_{DP} = 0.36 and 0.68. Here, the values of the permeability are created using a geostatistical simulator SGeMS, and then these values are normalized to have the assigned mean value (1 mD) and each specified standard deviation (0, 0.2 and 0.5). Thus, the permeability distribution patterns are all the same, while only the level of heterogeneity is different.

Table 18 Reservoir Properties (3D Heterogeneous)

Grid	[40, 40, 10]	[-]
ΔX	10.05	[ft]
ΔY	10.05	[ft]
ΔZ	2.0	[ft]
ϕ	0.10	[-]
V_{DP}	0, 0.36, 0.68	[-]
c_f	1.0e-6	[1/psi]
p_{init}	5200	[psia]
$S_{w,init}$	0	[-]

Table 19 Well Properties (3D Heterogeneous)

Well Type	Vertical	[-]
Location	[20, 20, 1-10]	[-]
Target Rate	10	[STB/D]
BHP Constraint	1500	[psia]

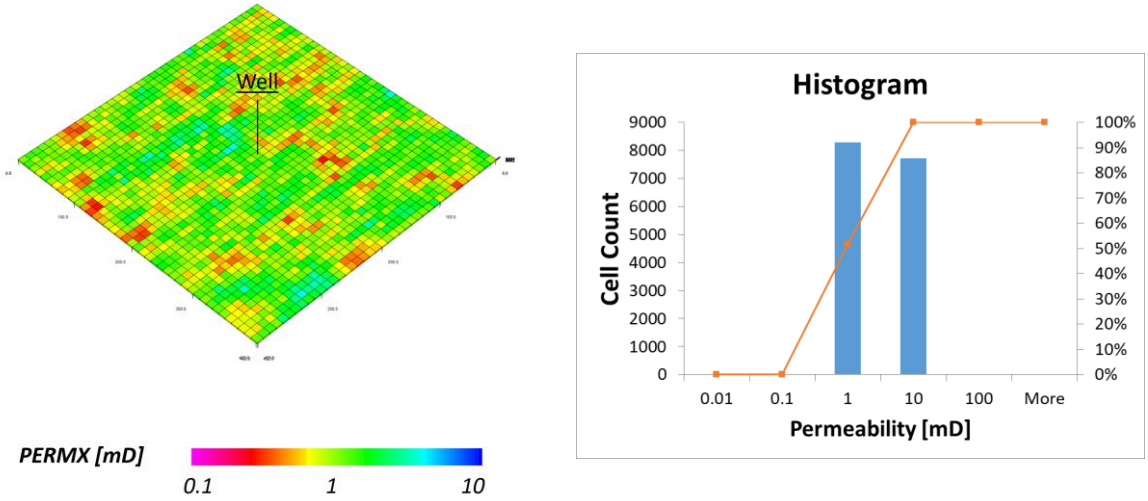

Figure 64 3D Reservoir Heterogeneity Map (left) and Pressure Transient Profile (right): V_{DP} = 0.36

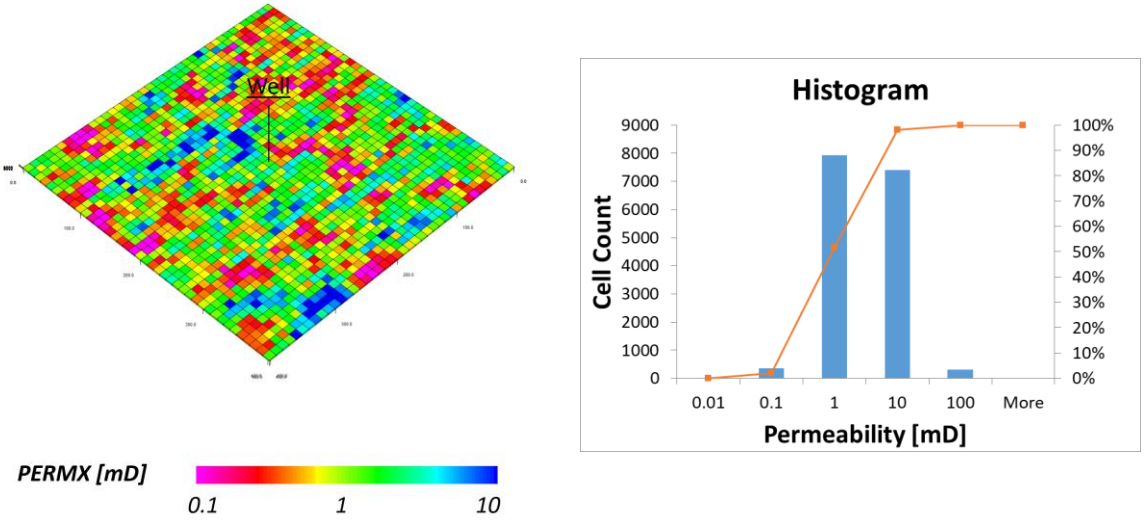

Figure 65 3D Reservoir Heterogeneity Map (left) and Pressure Transient Profile (right): V_{DP} = 0.68

Using these models, we first compare the early-mid time well performance based on FMM and PSS with low production rate. Figure 66, Figure 67 and Figure 68 represent the pressure transient profile with each V_{DP}. The blue dots denote ECL finite difference simulation,

and the red and green lines represent PSS and FMM based result, respectively. The solid and dash line correspond to SIM and DTOF in each figure.

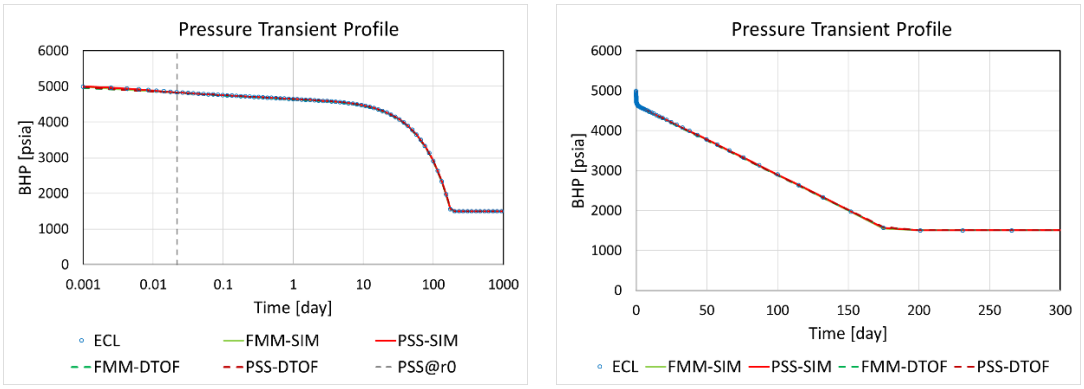

Figure 66 Pressure Transient Profile Comparison (Homogeneous)

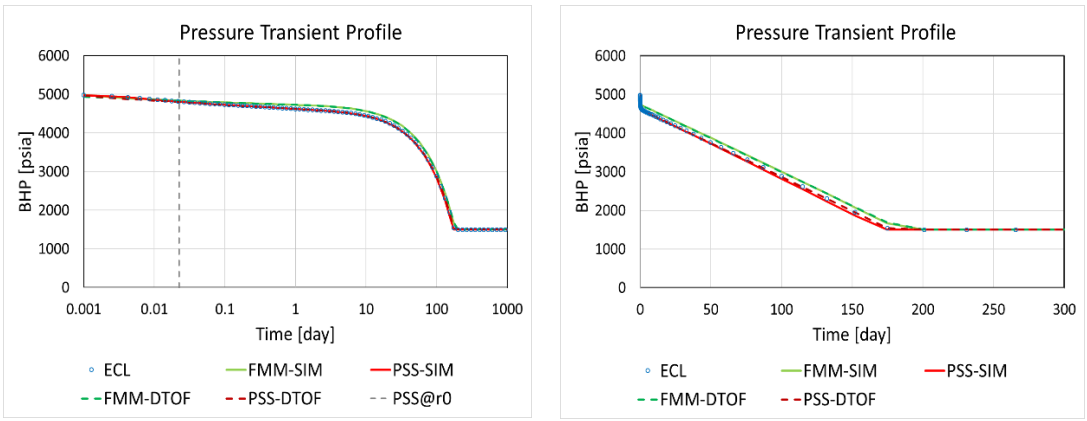

Figure 67 Pressure Transient Profile Comparison (V_{DP} = 0.36)

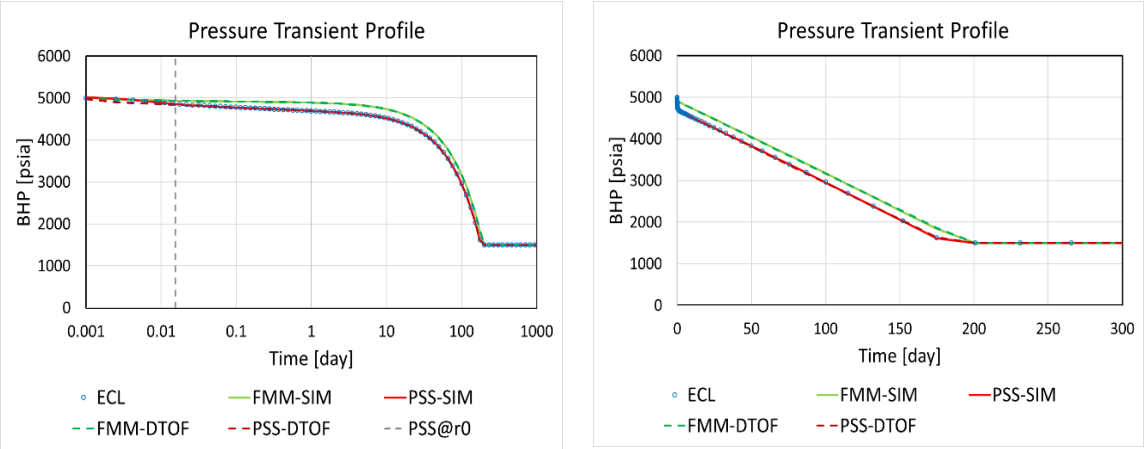

Figure 68 Pressure Transient Profile Comparison (V_{DP} = 0.68)

From these figures, first it can be observed that a pair of FMM-SIM and FMM-DTOF and a pair of PSS-SIM and PSS-DTOF generate almost the same result for both FMM and PSS. This means that the derived pressure transient solution should be almost the same regardless of numerical simulation or asymptotic approximation, because the corresponding pore volume and transmissibility are the same, as long as it is under the same coordinate. Secondly, although there is no discrepancy in pressure transient regardless of pressure solutions for the homogeneous case, the data mismatch, especially for the mid-late time, increases as the reservoir becomes more heterogeneous. Meanwhile, the pressure transient results based on PSS-SIM and PSS-DTOF are accurate against ECL simulation throughout the production history. This indicates that the PSS coordinate better represents the entire reservoir pressure drop rather than the DTOF coordinate, and that the DTOF coordinate is no longer along the actual pressure drop for mid-late time in highly heterogeneous media. It also depends up on the level of heterogeneity how far the underlying assumption of FMM holds.

In the next case study, we analyze the rate transient profile. The purpose of this study is to test the robustness of the PSS coordinate under BDF. Here, we use the same reservoir models

described in Figure 64 - Figure 65, and increase the production rate so that the reservoir switches to BDF. The well properties used for this study is shown in Table 20.

Table 20 Well Properties (Heterogeneity Effect Analysis)

Well Type	Vertical	[-]
Location	[20, 20, 1-10]	[-]
Target Rate	100	[STB/D]
BHP Constraint	700	[psia]

Figure 69, Figure 70 and Figure 71 represent the pressure transient profile with each heterogeneity. The blue dots denote ECL finite difference simulation, and the red and green lines represent PSS and FMM based result, respectively. The solid and dash line correspond to SIM and DTOF in each figure.

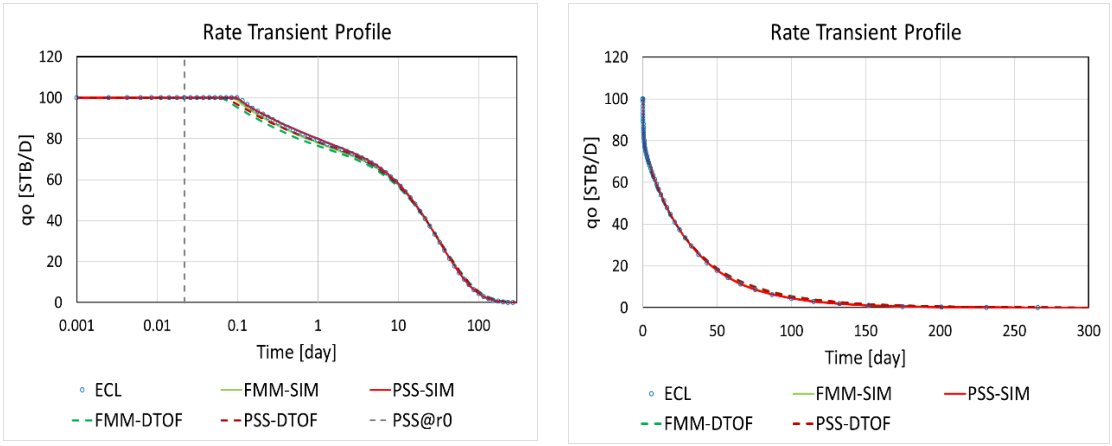

Figure 69 Rate Transient Profile Comparison (Homogeneous)

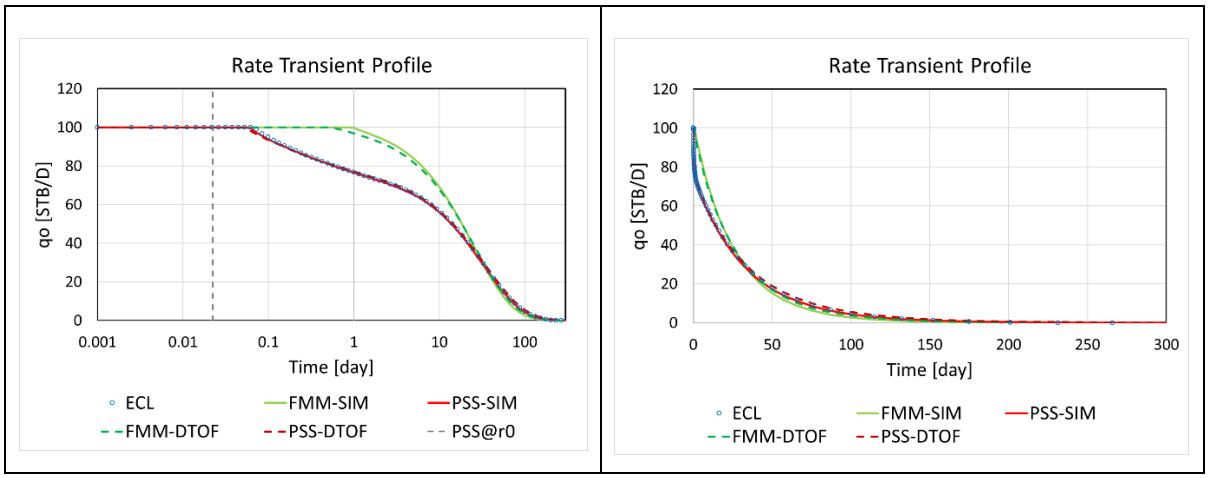

Figure 70 Rate Transient Profile Comparison (V_{DP} = 0.36)

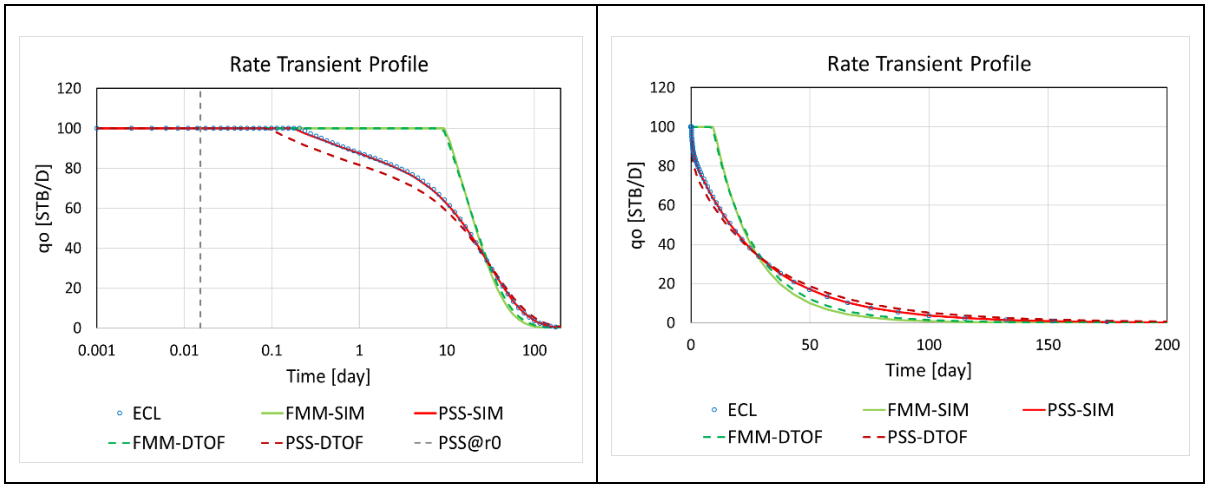

Figure 71 Rate Transient Profile Comparison (V_{DP} = 0.68)

Similarly to the pressure transient case studies, it can be observed that FMM-SIM/DTOF can output the production rate with high accuracy for the homogeneous case even under BDF, but the level of accuracy drops as the model becomes more heterogeneous (V_{DP} = 0.36 and 0.68). Meanwhile, the oil production rate based on PSS-SIM is always accurate against ECL numerical simulation, which indicates the importance of the pressure drop alignment with the constructed 1D coordinate. Lastly, as for the comparison between PSS-SIM and PSS-DTOF, PSS-DTOF can generally calculate the production rate with the same level of accuracy as PSS-SIM, but it can be

seen that there are small mismatch between these two in the case of V_{DP} = 0.68. This implies that the asymptotic relation between pressure and rate may not be as accurate a representation under BDF depending upon the degree of reservoir heterogeneity.

Lastly, we come back to the field model demonstrated in Section 3.7.3. Figure 72 shows the pressure and rate transient profile of PSS-DTOF, PSS-SIM, FMM-DTOF, FMM-SIM and ECL. The reservoir model is described in Section 2.5. V_{DP} in the model is 0.765, so it is even more heterogeneous than any of the 3D heterogeneous models shown in this section. The well placed at the center of the reservoir produces oil with a fixed rate and it does not hit the BHP constraint throughout the production history.

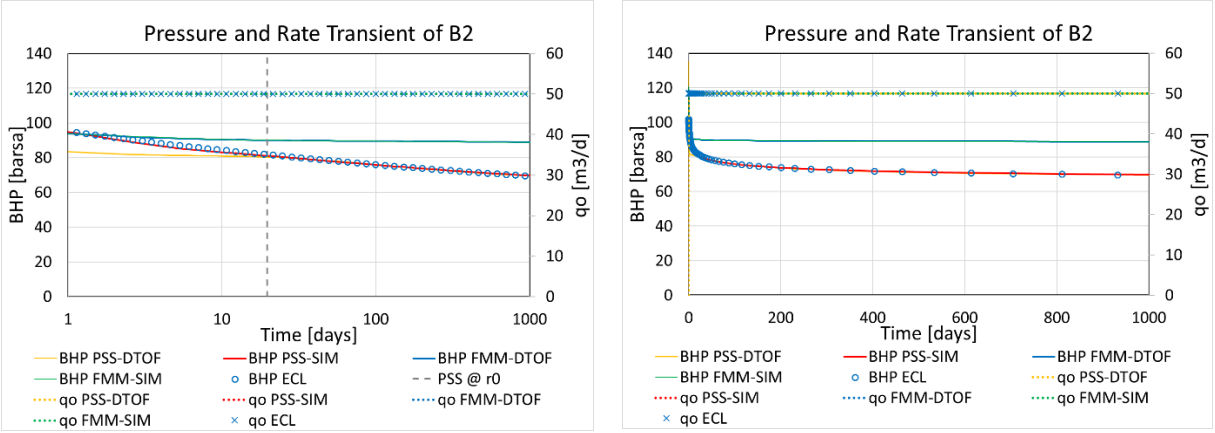

Figure 72 Pressure/Rate Transient Profiles using the Single Well Field Model

From the figure, we can confirm that both PSS-DTOF and PSS-SIM match the Eclipse finite difference simulation result after the PSS at Peaceman radius, while FMM-DTOF and FMM-SIM cannot follow its trend. Taking into consideration what we learned from this case study with various level of heterogeneity, we can conclude that this discrepancy is as a result of the difference in the constructed 1D coordinate under high heterogeneity. These entire case

studies indicate that it is important to have a well-aligned 1D coordinate along with the reservoir pressure drop.

5.2. Boundary Effect

In addition to the heterogeneity effect, the quality of the DTOF coordinate is also sensitive to the well positioning. In this section, we take a look at the field case study performed in Section 2.4 and 4.4 to make an analysis of the reservoir boundary effect. First, to double check the level of heterogeneity, we take an example of the single well (A1), which is located far away from the reservoir as described in Figure 73. The well produces oil at target rate at first, and shift to BHP constraint later. The reservoir and well properties are shown in Table 10 and Table 21, respectively, and the fluid properties are the same as Table 3. The permeability and porosity distribution are described in Figure 27 and Figure 28, respectively.

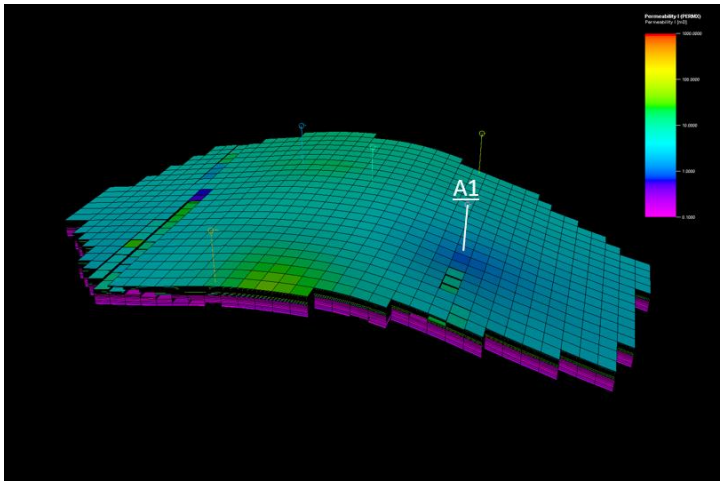

Figure 73 Single Well Field Model with A1

Table 21 Well Properties (Boundary Effect Analysis)

Well Type	Vertical, Fully Completed	[-]
Target Rate	500	[STB/D]
BHP Constraint	700	[psia]

Figure 74 shows the pressure and rate transient response of FMM-SIM and PSS-SIM in comparison with ECL. The comparison between FMM-SIM and PSS-SIM shows that the pressure and rate transient profiles are close to each other, which implies that the constructed 1D coordinate is both a good representation of the pressure drop in the 3D reservoir model, and they are almost the same. This result indicates the reservoir model used for the study has sufficiently smooth heterogeneity distribution in its model, which is necessary for the underlying assumption of FMM to hold.

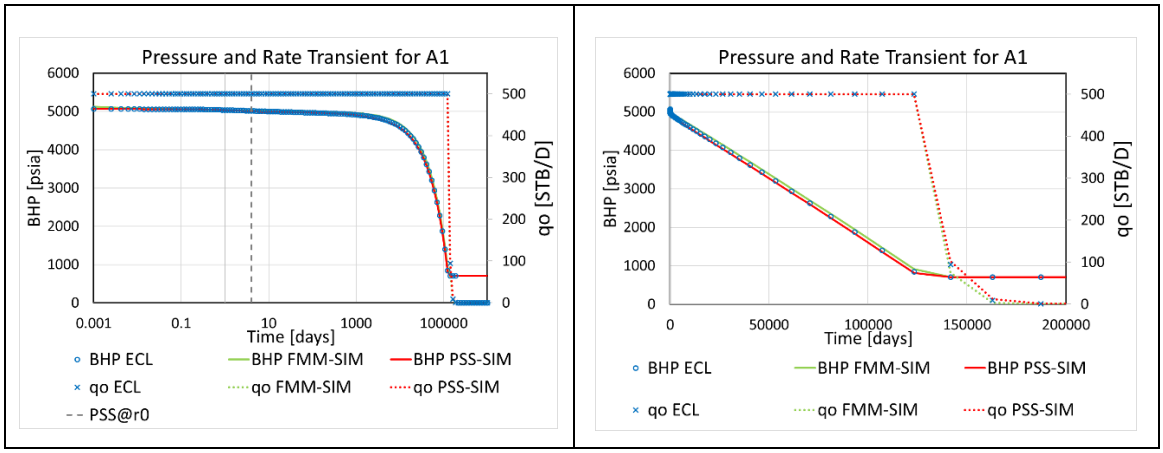

Figure 74 Pressure Transient Profiles with A1

Next, for the purpose of the boundary effect analysis, we pick only a single well which is located right near the reservoir boundary as described in Figure 75. The well produces oil at target rate at first, and shift to BHP constraint later. The reservoir and well properties are shown in the 2.4 (Table 10 and Table 21, respectively), and the fluid properties are the same as Table 3.

The permeability and porosity distribution are described in Figure 27 and Figure 28, respectively.

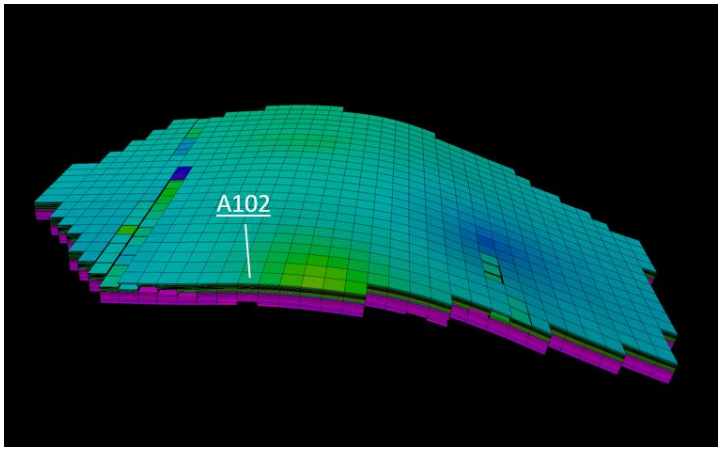

Figure 75 Single Well Field Model with A102

Figure 76 shows the pressure transient profiles based on FMM-SIM/DTOF, PSS-DTOF/SIM and ECL all together. The solid and dash line correspond to the BHP of SIM and DTOF. The round-dot lines are oil production rates.

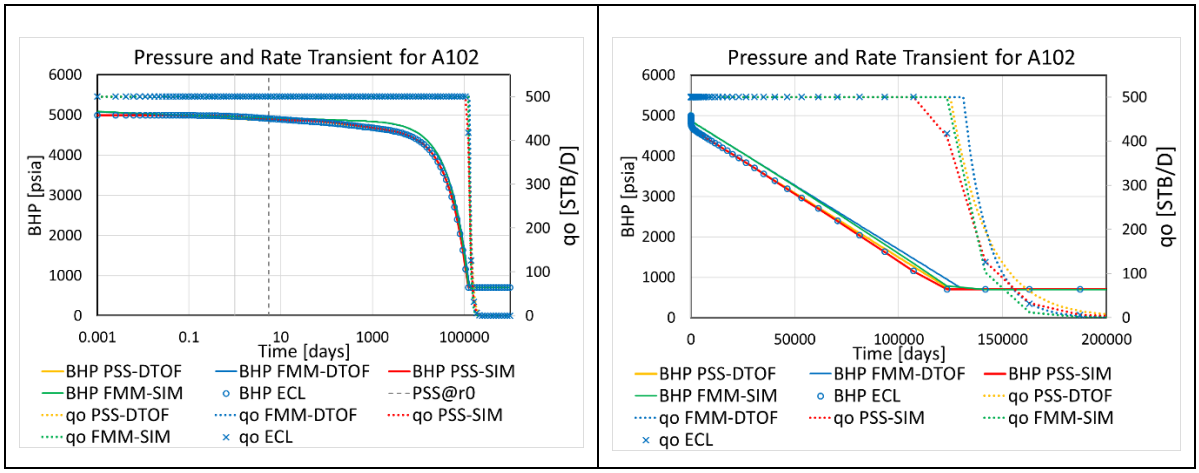

Figure 76 Pressure Transient Profiles with A102

For the purpose of the analysis, we take a look at the pressure and rate transient profiles one by one in the following sections.

- FMM-SIM vs PSS-SIM

The comparison between FMM-SIM and PSS-SIM gives us information about which is a better representation of the entire reservoir pressure profile. Figure 77 shows the pressure and rate transient based on FMM-SIM and PSS-SIM. The red and green lines represent PSS-SIM and FMM-SIM, respectively. The solid and round dot lines are BHP and rate for each type. The blue dot and cross points denote ECL finite difference simulation.

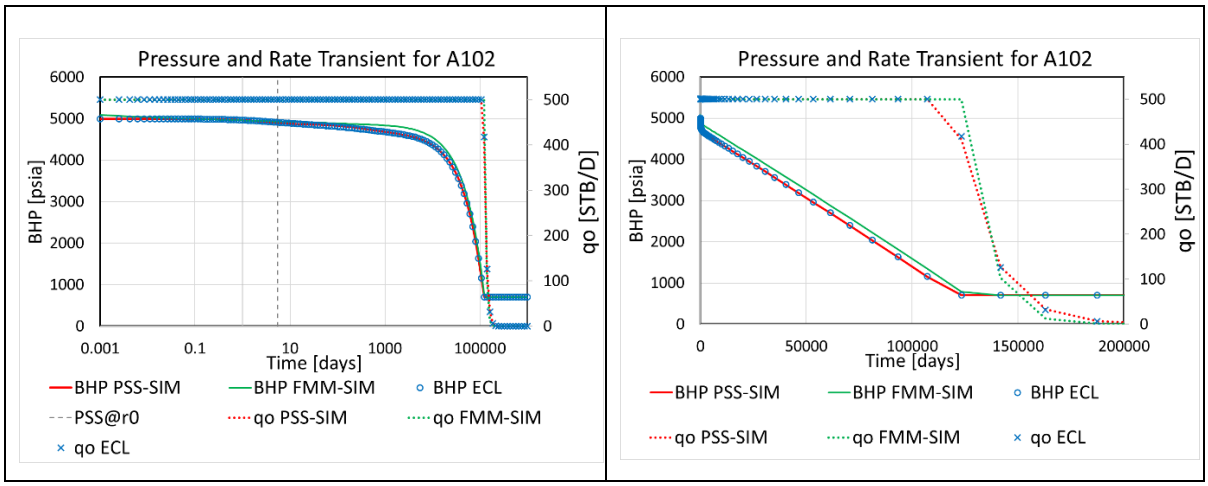

Figure 77 Pressure Transient Profiles with A102: FMM-SIM vs PSS-SIM

The comparison of the pressure transient profiles shows that FMM-SIM has a mismatch against ECL finite difference simulation. This is because the DTOF coordinate is a simply based on the Diffusive Time of Flight (travel time) to the well, so it cannot reflect the reflection of the pressure propagation at the reservoir boundary, which is located very close to the well in this case, into the actual pressure drop. On the other hand, the pressure transient profile based on PSS-SIM has a perfect match with the ECL simulation result. More importantly, the rate transient response based on PSS-SIM completely matches that of ECL simulation. This indicates that the PSS coordinate, which is constructed based on the PSS pressure drop of the reservoir, is still a good 1D representation of the pressure drop in the 3D reservoir model even for BDF.

- PSS-SIM vs PSS-DTOF

In the previous comparison, we are positive that the PSS coordinate is a good 1D representation of the pressure drop in the 3D reservoir model. Next, under the constructed PSS coordinate, we compare PSS-SIM with PSS-DTOF to see how far the asymptotic pressure approximation is valid. Figure 78 shows the pressure and rate transient based on PSS-SIM and PSS-DTOF. The red-solid and orange-solid lines represent the BHP based on PSS-SIM and PSS-DTOF, respectively. The red-dot and orange-dot lines are oil production rate for PSS-SIM and PSS-DTOF. The blue dot and cross points denote ECL finite difference simulation.

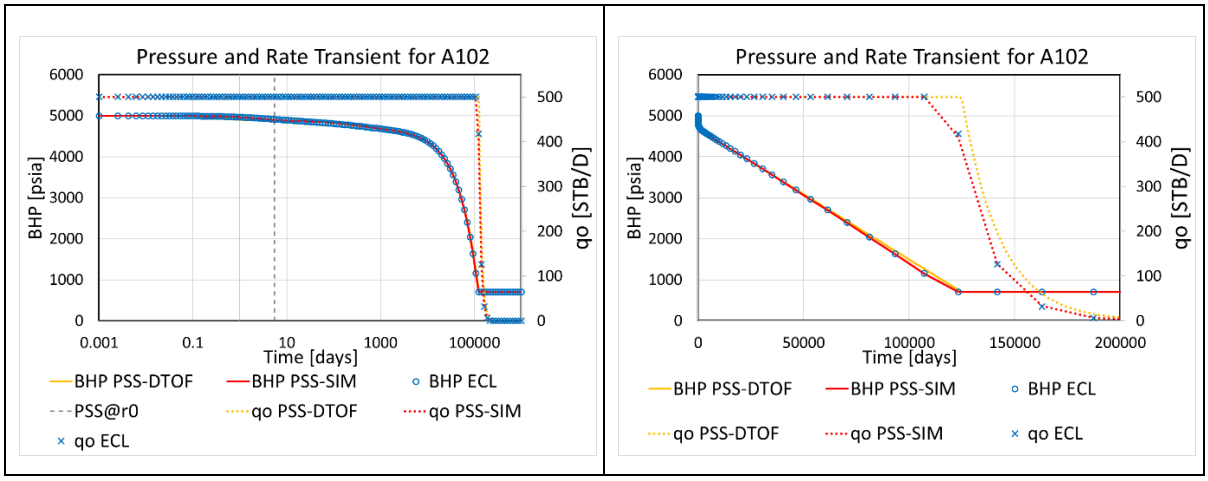

Figure 78 Pressure Transient Profiles with A102: PSS-SIM vs PSS-DTOF

The comparison of the pressure transient profiles shows that PSS-DTOF has a complete match against ECL finite difference simulation. This indicates that the asymptotic pressure approximation is accurate for the early-mid time. However, the comparison of the rate transient profiles shows that PSS-DTOF has a mismatch against ECL finite difference simulation once the well hits the assigned BHP constraint. This indicates that the asymptotic relation between pressure and flux may not provide a good approximation under the BDF.

5.3. Computation Time

Lastly, we make a comparison with respect to computation time for each pressure solution. In this section, we use the single well field model described in Figure 73 for computation time analysis. Figure 79 shows the comparison of these four approaches against Eclipse numerical simulation.

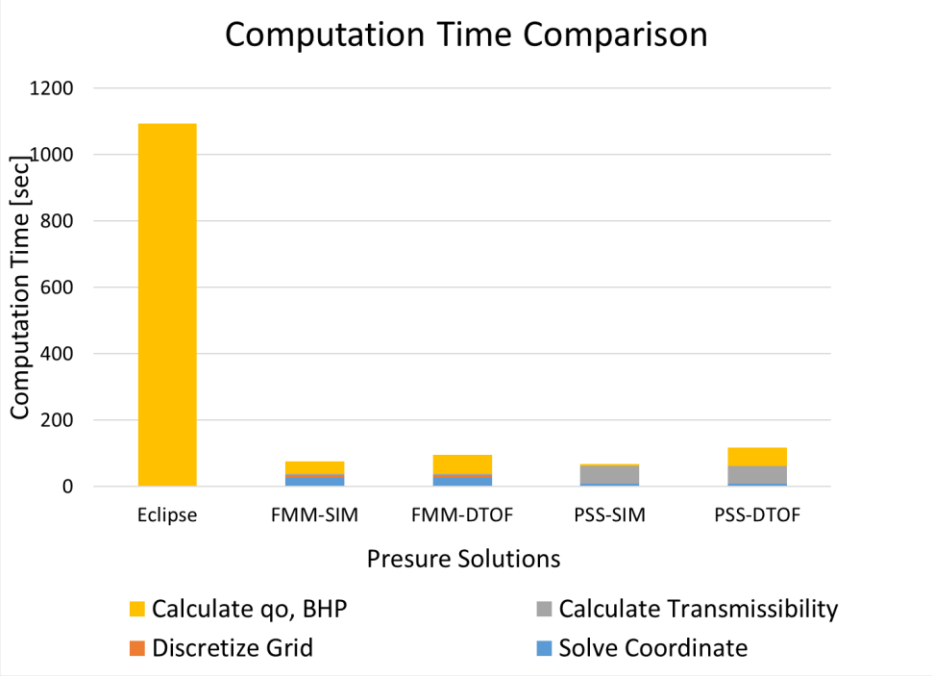

Figure 79 Computation Time Comparison

First of all, the whole computation time for Eclipse numerical simulation, FMM-SIM, FMM-DTOF, PSS-SIM and PSS-DTOF are 1094.4, 75.8, 95.2, 66.5, and 116.5 sec, respectively. This indicates that these four approaches gained 10-15 times computation speed up. In the whole calculation process, the numerical simulation (SIM) and the asymptotic pressure approximation (DTOF) have three processes in common (Solving the coordinate, discretizing the grid and calculating transmissibility), and have difference only in the pressure and rate calculation. From the comparison, it is observed that PSS-DTOF and FMM-DTOF take more time in solving the

whole system than PSS-SIM and FMM-SIM. However, this is simply due to the difference in construction of the code and matrix solver. In the study, we used Eclipse numerical simulator for the pressure/rate calculation in PSS-SIM and FMM-DTOF, while we used an iteration loop with respect to time step and Python library for solving the pressure matrix in PSS-DTOF and FMM-DTOF. Next, we can also see that PSS-SIM has slightly smaller computation time than FMM-SIM. In fact, PSS-SIM overcomes FMM-SIM in calculation speed for coordinate, discretization and pressure/rate, but SPP-SIM/DTOF has an overhead in calculating the 1D transmissibility (which corresponds to Section 3.6.1.2). This can be one of future works to be improved.

Throughout the case study in this section we figured out the following points:

- Even if the reservoir heterogeneity is sufficiently smooth, the DTOF coordinate is not well aligned with the actual pressure drop of the entire reservoir, when the well is located near the reservoir boundary
- This is because the DTOF coordinate is constructed simply based on the Diffusive Time of Flight (travel time) and it cannot take into consideration the pressure drop reflection at the reservoir boundary
- PSS-SIM has a perfect match in pressure and rate transient response with ECL finite difference simulation, which indicates that the PSS coordinate is a perfect 1D representation of the entire reservoir pressure drop both for early-mid (transient-PSS) and late time (BDF)
- Both SIM and DTOF have a perfect match in pressure transient. This indicates that the asymptotic relation between pressure and rate is accurate for the early-mid time (transient-PSS)
- DTOF has mismatch in rate at the late time, which implies that the asymptotic pressure approximation does not hold well under BDF
- PSS-SIM and PSS-DTOF have an overhead in calculating transmissibility, which is one of future works

6. CONCLUSION AND FUTURE WORK

This research study started by clarifying the cause of the mismatch in pressure and rate transient profile based on FMM-SIM/DTOF against ECL numerical solution. FMM-SIM/DTOF not only requires sufficiently smooth heterogeneity for its underlying assumption to hold, but also is sensitive to the boundary effect. In addition to the external reservoir boundary, the inner boundary also affect the pressure gradient of the reservoir. This effect may become not negligible under multiple perforation or hydraulic fractured wells. As a solution, we proposed the use of the PSS as a spatial coordinate for the fast 1D reservoir simulation. This approach has a few limitations for its application. First, it requires the sufficiently smooth connectivity for its interval due to the block centered discretization. Secondly, this approach cannot take into consideration the gravity effect for the coordinate construction, since the coordinate is simply dependent on PSS pressure drop. Hence, a reservoir model where a pressure vector is not associated with a gravity vector may not be a good target of this approach, such as a heavy oil reservoir. Third, a reservoir with strong phase discrepancy is not a good target such as water/gas injection models, since we cannot observe sweep effects within the transformed 1D interval. Regardless of these limitations, however, this approach has its own strength which benefits reservoir simulation analysis. The correlation analysis of the constructed 1D coordinate and pressure drop indicates that the PSS coordinate is a better representation of the pressure drop of the entire reservoir rather than the DTOF coordinate. Meanwhile, the pressure drop is well-aligned with the DTOF coordinate only for the early time. This analysis supports the argument that FMM-SIM/DTOF is a good application for unconventional reservoirs where the transient regime lasts for a long time due to their ultra-low permeability, but this is not always a good application for conventional reservoirs. Besides, although the PSS coordinate is constructed

based on the pressure drop under PSS, this is still a good representation under the BDF. Further, the PSS coordinate has one more benefit that it does not requires a complicated treatment for faulted reservoir models unlike FMM. Consequently, the use of PSS pressure drop as a spatial coordinate has a potential to take over the DTOF coordinate. Thus, both PSS-SIM and PSS-DTOF are beneficial for reservoir characterization history matching to find the well-matched realization models by ranking them based on data mismatch of production forecast against observed well performance. As an example of applications outside of oil and gas industry, these approaches might be also useful in tracking contamination in the underground water system to determine which part of the water can be drinking water for humans, since both of these approaches are based on transmissibility upscaling of fluid flow. Next, the comparison of PSS-SIM and PSS-DTOF tells us that PSS-DTOF can provide the pressure transient response with the same level of accuracy for the early-mid time, while the rate transient response has small mismatch at the late time. This is because the asymptotic relation between pressure and rate does not perfectly hold well for BDF. However, PSS-DTOF has its benefit that it can dramatically reduce the number of unknowns compared to the numerical finite difference simulation. Considering this characteristics, PSS-DTOF is well suited for the use of the early-mid time reservoir development, such as well spacing optimization problems due to the computational speed up. Consequently, the application of PSS-DTOF for the well spacing optimization for multiple well reservoir development can be one of good future work.

REFERENCES

Chen, H., Onishi, T., Park, J., & Datta-Gupta, A. (2020). *Computing Pressure Front Propagation Using the Diffusive Time of Flight in Structured and Unstructured Grid Systems Via the Fast Marching Method*. Paper presented at the SPE Annual Technical Conference and Exhibition. https://doi.org/10.2118/201771-MS

Dake, L. P. (1983). *Fundamentals of Reservoir Engineering* (Vol. 8). Amsterdam, Netherlands: Elsevier Science.

Datta-Gupta, A., Xie, J., Gupta, N., King, M. J., & Lee, W. J. (2011). Radius of Investigation and its Generalization to Unconventional Reservoirs. *Journal of Petroleum Technology*, *63*(07), 52-55. doi:10.2118/0711-0052-JPT

Dougherty, E. R., & Lotufo, R. A. (2003). *Hands-on Morphological Image Processing* (Vol. TT59). Bellingham, WA: SPIE Press.

Dykstra, H., & Parsons, R. L. (1950). The Prediction of Oil Recovery by Water Flooding. In *Secondary Recovery of Oil in the United States* (2nd ed., pp. 160–174). Washington, DC: American Petroleum Institute.

Fujita, Y., Datta-Gupta, A., & King, M. J. (2015). *A Comprehensive Reservoir Simulator for Unconventional Reservoirs Based on the Fast Marching Method and Diffusive Time of Flight*. Paper presented at the SPE Reservoir Simulation Symposium, Houston, Texas, USA. https://doi.org/10.2118/173269-MS

Fujita, Y., Datta-Gupta, A., & King, M. J. (2016). A Comprehensive Reservoir Simulator for Unconventional Reservoirs That Is Based on the Fast Marching Method and Diffusive Time of Flight. *SPE Journal*, *21*(06), 2276-2288. doi:10.2118/173269-PA

Gunasekera, D., Cox, J., & Lindsey, P. (1997). *The Generation and Application of K-Orthogonal Grid Systems*. Paper presented at the SPE Reservoir Simulation Symposium, Dallas, Texas. https://doi.org/10.2118/37998-MS

Horne, N. R. (1995). *Modern Well Testing Analysis: A Computer-Aided Approach*. Palo Alto, CA: Petroway, Inc.

Iino, A., & Datta-Gupta, A. (2018). *Optimizing CO2 and Field Gas Injection EOR in Unconventional Reservoirs Using the Fast Marching Method*. Paper presented at the SPE Improved Oil Recovery Conference. https://doi.org/10.2118/190304-MS

Iino, A., Jung, H. Y., Onishi, T., & Datta-Gupta, A. (2020). *Rapid Simulation Accounting For Well Interference in Unconventional Reservoirs Using Fast Marching Method*. Paper presented at the SPE/AAPG/SEG Unconventional Resources Technology Conference. https://doi.org/10.15530/urtec-2020-2468

Iino, A., Onishi, T., & Datta-Gupta, A. (2020). Optimizing CO2- and Field-Gas-Injection EOR in Unconventional Reservoirs Using the Fast-Marching Method. *SPE Reservoir Evaluation & Engineering, 23*(01), 261-281. doi:10.2118/190304-pa

Iino, A., Vyas, A., Huang, J., Datta-Gupta, A., Fujita, Y., & Sankaran, S. (2017). *Rapid Compositional Simulation and History Matching of Shale Oil Reservoirs Using the Fast Marching Method*. Paper presented at the SPE/AAPG/SEG Unconventional Resources Technology Conference. https://doi.org/10.15530/URTEC-2017-2693139

King, M. J., Wang, Z., & Datta-Gupta, A. (2016). *Asymptotic Solutions of the Diffusivity Equation and Their Applications*. Paper presented at the SPE Europec featured at 78th EAGE Conference and Exhibition, Vienna, Austria. https://doi.org/10.2118/180149-MS

Kucuk, F., & Brigham, W. E. (1979). Transient Flow in Elliptical Systems. *SPE Journal, 19*(06), 401-410. doi:10.2118/7488-PA

Lee, W. J. (1982). *Well Testing*. Richardson, TX: Society of Petroleum Engineers.

Lee, W. J., Rollins, B. J., & Spivey, P. J. (2003). *Pressure Transient Testing*. Richardson, TX: Society of Petroleum Engineers.

Li, C., & King, M. J. (2020). Integration of Pressure Transient Data into Reservoir Models Using the Fast Marching Method. *SPE Journal, 25*(04), 1557-1577. doi:10.2118/180148-PA

Li, C., Wang, Z., & King, M. J. (2021). *Transient Drainage Volume Characterization and Flow Simulation in Reservoir Models Using the Fast Marching Method*. To appear, Computational Geosciences.

Malone, A., King, M. J., & Wang, Z. (2019). *Characterization of Multiple Transverse Fracture Wells Using the Asymptotic Approximation of the Diffusivity Equation*. Paper presented at the SPE Europec featured at 81st EAGE Conference and Exhibition, London, England, UK. https://doi.org/10.2118/195505-MS

Nunna, K., & King, M. J. (2020). Dynamic Diffuse-Source Upscaling in High-Contrast Systems. *SPE Journal, 25*(01), 347-368. doi:10.2118/182689-PA

Nunna, K., Liu, C.-H., & King, M. (2018). *Application Of Diffuse Source Basis Functions To Multiscale Simulation*. Paper presented at the ECMOR XVI - 16th European Conference on the Mathematics of Oil Recovery, Barcelona, Spain. https://doi.org/10.3997/2214-4609.201802250

Park, J., Iino, A., Datta-Gupta, A., Bi, J., & Sankaran, S. (2019). *Rapid Modeling of Injection and Production Phases of Hydraulically Fractured Shale Wells Using the Fast Marching Method*. Paper presented at the SPE/AAPG/SEG Unconventional Resources Technology Conference. https://doi.org/10.15530/urtec-2019-339

Peaceman, D. W. (1978). Interpretation of Well-Block Pressures in Numerical Reservoir Simulation (includes associated paper 6988). *SPE Journal, 18*(03), 183-194. doi:10.2118/6893-PA

Peaceman, D. W. (1983). Interpretation of Well-Block Pressures in Numerical Reservoir Simulation With Nonsquare Grid Blocks and Anisotropic Permeability. *SPE Journal, 23*(3), 531-543. doi:10.2118/10528-PA

Pedrosa, O. A., Jr., & Aziz, K. (1986). Use of a Hybrid Grid in Reservoir Simulation. *SPE Reservoir Engineering, 1*(06), 611-621. doi:10.2118/13507-PA

Ponting, D. K. (1989). *Corner Point Geometry in Reservoir Simulation*. Paper presented at the 1st European Conference on the Mathematics of Oil Recovery, Cambridge, UK.

Schlumberger. (2019a). *Eclipse Technical Description 2019.1*. Abingdon, UK: Schlumberger.

Schlumberger. (2019b). *Eclipse Version 2019.1 Reference Manual*. Abingdon, UK: Schlumberger.

Sethian, J. (1999). Fast Marching Methods. *SIAM Review, 41*(2), 199-235. doi:10.1137/S0036144598347059

Thambynayagam, M. (2011). *The Diffusion Handbook: Applied Solutions for Engineers*. New York, NY: McGraw-Hill.

Virtanen, P., Gommers, R., Oliphant, T. E., Haberland, M., Reddy, T., Cournapeau, D., . . . SciPy Contributors. (2020). SciPy 1.0: Fundamental Algorithms for Scientific Computing in Python. *Nature Method, 17*(3), 261-272. doi:10.1038/s41592-019-0686-2

Wang, Z., Li, C., & King, M. (2017). *Validation and Extension of Asymptotic Solutions of Diffusivity Equation and Their Applications to Synthetic Cases*. Paper presented at the SPE Reservoir Simulation Conference, Montgomery, Texas, USA. https://doi.org/10.2118/182716-MS

Wang, Z., Malone, A., & King, M. (2019). Quantitative Production Analysis and EUR Prediction from Unconventional Reservoirs Using a Data-Driven Drainage Volume Formulation. *Computational Geosciences*. doi:10.1007/s10596-019-09833-8

Winestock, A. G., & Colpitts, G. P. (1965). Advances in Estimating Gas Well Deliverability. *Journal of Canadian Petroleum Technology, 4*(3), 111-119. doi:10.2118/65-03-01

Yang, C., Xue, X., King, M. J., & Datta-Gupta, A. (2017). *Flow Simulation of Complex Fracture Systems With Unstructured Grids Using the Fast Marching Method*. Paper presented at the SPE/AAPG/SEG Unconventional Resources Technology Conference. https://doi.org/10.15530/URTEC-2017-2691393

Zhang, Y., Bansal, N., Fujita, Y., Datta-Gupta, A., King, M. J., & Sankaran, S. (2014). *From Streamlines to Fast Marching: Rapid Simulation and Performance Assessment of Shale Gas Reservoirs Using Diffusive Time of Flight as a Spatial Coordinate*. Paper presented at the SPE Unconventional Resources Conference, The Woodlands, Texas, USA. https://doi.org/10.2118/168997-MS

Zhang, Y., Bansal, N., Fujita, Y., Datta-Gupta, A., King, M. J., & Sankaran, S. (2016). From Streamlines to Fast Marching: Rapid Simulation and Performance Assessment of Shale-Gas Reservoirs by Use of Diffusive Time of Flight as a Spatial Coordinate. *SPE Journal, 21*(05), 1883-1898. doi:10.2118/168997-PA

Zhang, Y., Yang, C., King, M. J., & Datta-Gupta, A. (2013). *Fast-Marching Methods for Complex Grids and Anisotropic Permeabilities: Application to Unconventional Reservoirs*. Paper presented at the SPE Reservoir Simulation Symposium, The Woodlands, Texas, USA. https://doi.org/10.2118/163637-MS